



---

## CHAPTER ONE

# Cyclostratigraphy and Astrochronology in 2018

Linda A. Hinnov

Department of Atmospheric, Oceanic, and Earth Sciences, George Mason University, Fairfax, VA, United States

E-mail: [lhinnov@gmu.edu](mailto:lhinnov@gmu.edu)

## Contents

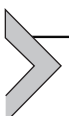
|   |    |
|---|----|
| 1. Introduction   | 4  |
| 1.1 Astrodynamics — Orbital Eccentricity and Inclination    | 5  |
| 1.1.1 <i>Orbital Eccentricity and Inclination Variables</i> | 5  |
| 1.1.2 <i>Astronomical Solutions</i>                         | 8  |
| 1.1.3 <i>Paleo-Astrodynamics</i>                            | 8  |
| 1.2 Geodynamics —Precession and Obliquity                   | 11 |
| 1.2.1 <i>Luni-Solar Precession</i>                          | 11 |
| 1.2.2 <i>Precession and Obliquity Equations</i>             | 13 |
| 1.2.3 <i>Tidal Dissipation and Dynamical Ellipticity</i>    | 13 |
| 1.2.4 <i>Paleo-Geodynamics</i>                              | 15 |
| 1.3 Milankovitch Cycles and Paleoclimate Responses          | 17 |
| 1.3.1 <i>The Insolation Equation</i>                        | 18 |
| 1.3.2 <i>Paleoclimate Responses</i>                         | 19 |
| 1.4 Stratigraphic Record of Milankovitch Cycles             | 24 |
| 1.4.1 <i>Rectification Effects</i>                          | 25 |
| 1.4.2 <i>Variable Accumulation Rates</i>                    | 25 |
| 2. Cyclostratigraphy  | 28 |
| 2.1 Cenozoic  | 28 |
| 2.2 Mesozoic  | 31 |
| 2.2.1 <i>Cretaceous</i>                                     | 31 |
| 2.2.2 <i>Jurassic</i>                                       | 33 |
| 2.2.3 <i>Triassic</i>                                       | 33 |
| 2.3 Paleozoic   | 34 |
| 2.3.1 <i>Permian</i>  | 35 |
| 2.3.2 <i>Carboniferous</i>                                  | 35 |
| 2.3.3 <i>Devonian</i>                                       | 36 |
| 2.3.4 <i>Silurian</i>                                       | 37 |
| 2.3.5 <i>Ordovician</i>                                     | 37 |
| 2.3.6 <i>Cambrian</i>                                       | 38 |

|   |   |    |
|---|---|----|
| <b>2.4</b>  | Precambrian   | 39 |
| 2.4.1   | <i>Neoproterozoic</i>   | 39 |
| 2.4.2   | <i>Mesoproterozoic</i>  | 40 |
| 2.4.3   | <i>Paleoproterozoic</i>   | 40 |
| 2.4.4   | <i>Archean</i>  | 41 |
| <b>3.</b>   | Astrochronology   | 41 |
| <b>3.1</b>  | Astronomical Targets  | 42 |
| 3.1.1   | <i>Time Domain</i>  | 42 |
| 3.1.2   | <i>Frequency Domain</i>   | 43 |
| <b>3.2</b>  | Astronomical Metronomes   | 44 |
| 3.2.1   | <i>Venus and Jupiter Longitude of Perihelia and Earth's Orbital Eccentricity <math>g_2-g_5</math></i> | 44 |
| 3.2.2   | <i>Earth and Saturn Precession of Nodes and Earth's Orbital Inclination <math>s_3-s_6</math></i>      | 45 |
| <b>3.3</b>  | Classical Tuning  | 46 |
| 3.3.1   | <i>Visual Tuning</i>  | 46 |
| 3.3.2   | <i>Minimal Tuning</i>   | 47 |
| 3.3.3   | <i>Tune and Release</i>   | 47 |
| <b>3.4</b>  | Sedimentological Tuning   | 48 |
| 3.4.1   | <i>Aluminum Tuning</i>  | 48 |
| 3.4.2   | <i>Carbonate Tuning</i>   | 48 |
| 3.4.3   | <i>Depth-Derived Time Scales</i>  | 48 |
| 3.4.4   | <i>Turbidite, Conglomerate Removal</i>  | 49 |
| <b>3.5</b>  | Statistical Tuning  | 49 |
| 3.5.1   | <i>Average Spectral Misfit (ASM)</i>  | 49 |
| 3.5.2   | <i>Bayesian Tuning</i>  | 50 |
| 3.5.3   | <i>TimeOpt and TimeOptMCMC</i>  | 51 |
| 3.5.4   | <i>Correlation Coefficient (COCO)</i>   | 51 |
| 3.5.5   | <i>Other Assorted Techniques</i>  | 52 |
| <b>3.6</b>  | Astronomical Time Scale   | 52 |
| <b>4.</b>   | Conclusions   | 53 |
| Appendix A — Calculation of Earth's Orbital Eccentricity and Inclination    |   | 54 |
| A.1   | La2010 Solution Files   | 54 |
| A.2   | Orbital Eccentricity  | 55 |
| A.3   | Orbital Inclination   | 55 |
| Appendix B — Astronomical Solutions Transformative to Cyclostratigraphy     |   | 55 |
| B.1   | Analytical Solutions  | 55 |
| B.2   | Numerical Integrations  | 56 |
| Appendix C — Variables of Earth's Precession                                |   | 56 |
| C.1   | — Luni-Solar Precession   | 56 |
| C.2   | — Orbital Contributions to Precession and Obliquity   | 57 |
| C.3   | — Variable Definitions  | 58 |
| Appendix D — Lunar Recession and Earth Deceleration                         |   | 58 |
| Appendix E — Earth-Moon Roche Limit   |   | 59 |
| Appendix F — Calculating the $g_2-g_5$ and $s_3-s_6$ Metronomes With La2004 |   | 59 |

|   |    |
|---|----|
| Appendix G – Major Sequences of $g_2$ – $g_5$ Cycles in the Geologic Record | 60 |
| Cenozoic  | 60 |
| <i>Neogene</i>  | 60 |
| <i>Paleogene</i>  | 60 |
| Mesozoic  | 61 |
| <i>Cretaceous</i>   | 61 |
| <i>Jurassic</i>   | 61 |
| <i>Triassic</i>   | 62 |
| Paleozoic   | 62 |
| <i>Permian</i>  | 62 |
| <i>Carboniferous</i>  | 62 |
| <i>Devonian</i>   | 62 |
| <i>Silurian</i>   | 63 |
| <i>Ordovician</i>   | 63 |
| Acknowledgments   | 63 |
| References  | 64 |

## Abstract

After more than a century of doubt and equivocation, cyclostratigraphy — the stratigraphic record of astronomically forced paleoclimatic change — has come to be widely accepted in the geosciences. Cyclostratigraphy depicts a paleoclimate system that is intimately connected with and pervasively tuned to the variations of co-occurring astronomical and geophysical parameters that have affected the Earth through geologic time. Cyclostratigraphy provides a proprietary record of planetary orbital motions, and is the sole repository of evidence for interplanetary orbital resonance and chaotic interaction throughout Solar System history. Cyclostratigraphy has also recorded the evolution of Earth's rotation rate and mass distribution, and by consequence, the orbital dynamics of the Moon. For the most recent ten million years, cyclostratigraphy has been precisely correlated to quantitative astronomical models, and for hundreds of millions of years prior to that, has been matched to models with a progressively decreasing but still significant measure of confidence. This has led to the rise of astrochronology, which assigns cyclostratigraphy to a specific time scale based on its correlation to astronomical solutions. Modern astronomical solutions are highly consistent, indicating that the theory of Solar System dynamics has been described as completely as possible for 0 to at least 50 million years ago (Ma). This indicates that cyclostratigraphy can be correlated to the full Earth orbital eccentricity and/or inclination solution over 0–50 Ma, to contribute a high-precision astrochronology for the geologic time scale. For times prior to 50 Ma, astronomical models deviate substantially from one another as predicted by the Lyapunov time of the Solar System, and depict chaotic behavior, for example, between Earth and Mars. On the other hand, specific planetary orbits, notably those of Jupiter and Saturn, theoretically remain stable over much longer periods of time; these have led to the recognition of “metronomes” in Earth's orbital motions, specifically,  $g_2$  –  $g_5$  and  $s_3$  –  $s_6$ , which when identified in cyclostratigraphy can provide practical extensions to the Astronomical Time Scale for hundreds of millions of years into the past.



## 1. INTRODUCTION

The Earth's stratigraphic record of astronomically forced climate change originates from variations in the Earth's orientation with respect to the Sun imposed by gravitational attraction from the Moon, Sun and other planets. The motions of the attracting bodies are described by astrodynamical theory, and their interactions with the Earth invoke geodynamical theory. The coupling of these variations with the incoming solar radiation, known as insolation, is embodied in the Milankovitch theory of climate.

Planetary orbital motions are modeled as variations in orbital eccentricity and inclination ([Section 1.1](#)). A prediction of chaotic interactions between Earth and Mars during Cretaceous time has recently been validated by cyclostratigraphy. The Earth also experiences precession and obliquity variations due to its axial tilt and gravitational attraction from the Moon and Sun, and to a minor extent the other planets ([Section 1.2](#)). Tidal dissipation in the Earth–Moon system results in lunar recession, deceleration in Earth's rotation, and decreasing frequencies in the Earth's precession and obliquity. These effects are now being quantified by powerful new analyses of the cyclostratigraphic record. Earth's precession and obliquity variations control the amount of solar energy incident on the Earth, and influence paleoclimate change ([Section 1.3](#)).

Recovery of the cyclostratigraphic record of Earth's astronomical parameters has grown rapidly over the past several decades, first focusing on the Cenozoic Era, but advancing progressively into the Mesozoic Era, and most recently, the Paleozoic Era and the Precambrian ([Section 2](#)). These advances are attended by new problems, including a severe paucity of geochronologic constraints for cyclostratigraphic data series, and lack of knowledge about the deep-time evolution of the planetary orbits or Earth–Moon system evolution. The time calibration of cyclostratigraphy, or astrochronology, thus involves numerous strategies, most recently with the advent of extremely fast computers, brute-force optimization and Bayesian techniques ([Section 3](#)). The goal of astrochronology is to construct an “astronomical time scale” with a resolving power that exceeds and/or maintains the accuracy and precision of geologic time provided by radioisotope geochronology ([Section 4](#)).

## 1.1 Astrodynamics – Orbital Eccentricity and Inclination

The evolution of planetary orbits has been an active line of inquiry in astronomy for centuries, with Laplace and Lagrange describing in the late 18th century the equations of motion that are used for solutions to this day (historical perspective in [Laskar, 2013](#)). The original goal for accurate reconstruction of planetary motion has broadened to consider the more general problem of Solar System stability, which, due to the long timescales involved, requires observational data from the cyclostratigraphic record ([Laskar et al., 2011a, 2011b](#)). The basic solution variables are described ([1.1.1](#)), followed by a summary of legacy and current astronomical solutions and their limitations ([Section 1.1.2](#)), and ending with examples of cyclostratigraphic observations that have been used to validate one astronomical solution in particular ([Section 1.1.3](#)).

### 1.1.1 Orbital Eccentricity and Inclination Variables

Classical secular perturbation theory of the Solar System for  $n = 1, 2, 3, \dots, N = 9$  planets (including Pluto) in order of distance from the Sun involves the solution of orbital eccentricity and inclination variables (e.g., Eqs. (2) and (5) in [Bretagnon, 1974](#)):

$$\begin{aligned} z_n(t) &= e_n(t) \exp(i\Pi_n t) = h_n(t) + ik_n(t) \approx \sum_{j=1}^N A_{n,j} \exp(ig_j t) \\ \zeta_n(t) &= \sin\left(\frac{I_n(t)}{2}\right) \exp(i\Omega_n t) = p_n(t) + iq_n(t) \approx \sum_{j=1}^N B_{n,j} \exp(is_j t) \end{aligned} \quad (1)$$

The orbital elements  $e$ ,  $\Pi$ ,  $I$  and  $\Omega$  are eccentricity, longitude of perihelion, inclination and longitude of ascending node, respectively, and variables  $h_n(t)$ ,  $k_n(t)$ ,  $p_n(t)$ , and  $q_n(t)$ ;  $A_{n,j}$  and  $B_{n,j}$  are amplitudes, and  $g_j$  and  $s_j$  are the fundamental secular frequencies of the planets (e.g., Table 3 in [Laskar et al., 2004](#)).

Earth's orbital eccentricity is ([Fig. 2A and B; Appendix A](#)):

$$e_3(t) = \sqrt{h_3^2(t) + k_3^2(t)} \quad (2)$$

for which the  $g_j$  are the contributing frequencies of the planetary orbital perihelia. Values for  $h_3(t)$  and  $k_3(t)$  for time  $t$  in 1 kyear (kyr) steps

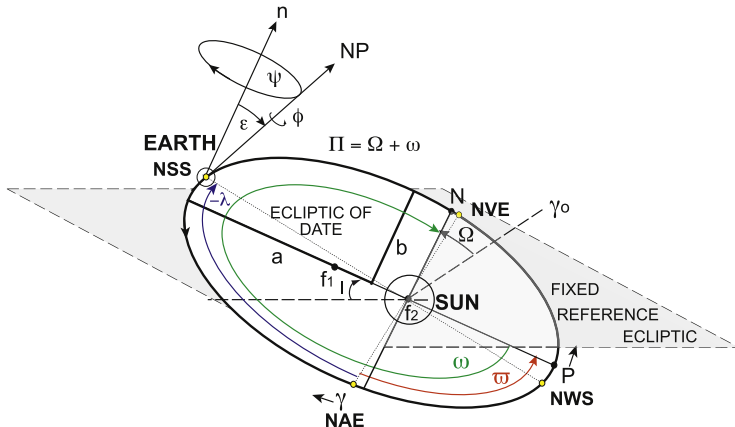


**Figure 1** Earth's astronomical parameters viewed from above the Earth's Northern Hemisphere. Earth is positioned near modern-day northern Summer Solstice. The Earth's orbit is elliptical with major axis  $a$  and minor axis  $b$ , and two foci ( $f_1, f_2$ ). The Sun's position is at  $f_2$ . The orbital elements are eccentricity  $e = \sqrt{(a^2 + b^2)/a}$ , longitude of perihelion ( $\Pi$ ), inclination ( $I$ ) and longitude of the ascending node ( $\Omega$ ). The plane of the Earth's orbit is the "ecliptic of date" and is inclined at an angle  $I$  relative to a "fixed reference ecliptic." The Earth's orbit intersects the reference ecliptic at a longitude  $\Omega$  at point N, the ascending node, relative to a fixed vernal point  $\gamma_0$ . The orbital perihelion point P, measured relative to  $\gamma_0$  as longitude of perihelion  $\Pi = \Omega + \omega$ , moves slowly anticlockwise. The argument of the perihelion  $\omega$  measures the angular distance between P and N. The angle  $\varpi = \Pi + \psi$  tracks the moving vernal point  $\gamma$  relative to P, which moves clockwise along the orbit due to the luni-solar precession  $\psi$ . The true longitude of the Earth  $\lambda$  varies from 0 to 360° throughout the year with respect to  $\gamma$ , in the clockwise direction, i.e., in the direction of the Earth's path; here for clarity it is drawn in the opposite direction. The Earth has an anticlockwise rotation rate  $\phi$  and an obliquity angle  $\varepsilon$  that precesses clockwise at a rate  $\psi$ . NP is the Earth's rotation axis ("North Pole"), and n is the normal to the ecliptic of date. Note: today, perihelion P is  $\omega = 103^\circ$  from  $\gamma$ , i.e., it occurs on calendar day January 3.

(negative  $t$  for time before present) are provided for the 2010 Laskar solutions. Earth's orbital eccentricity is otherwise customarily reported as a frequency decomposition, e.g., Table 6 of Laskar et al. (2004) lists the 20 leading trigonometric terms.

Earth's orbital inclination is (Fig. 2C and D; Appendix A):

$$I_3(t) = 2 \sin^{-1} \left( \sqrt{p_3^2(t) + q_3^2(t)} \right) \quad (3)$$

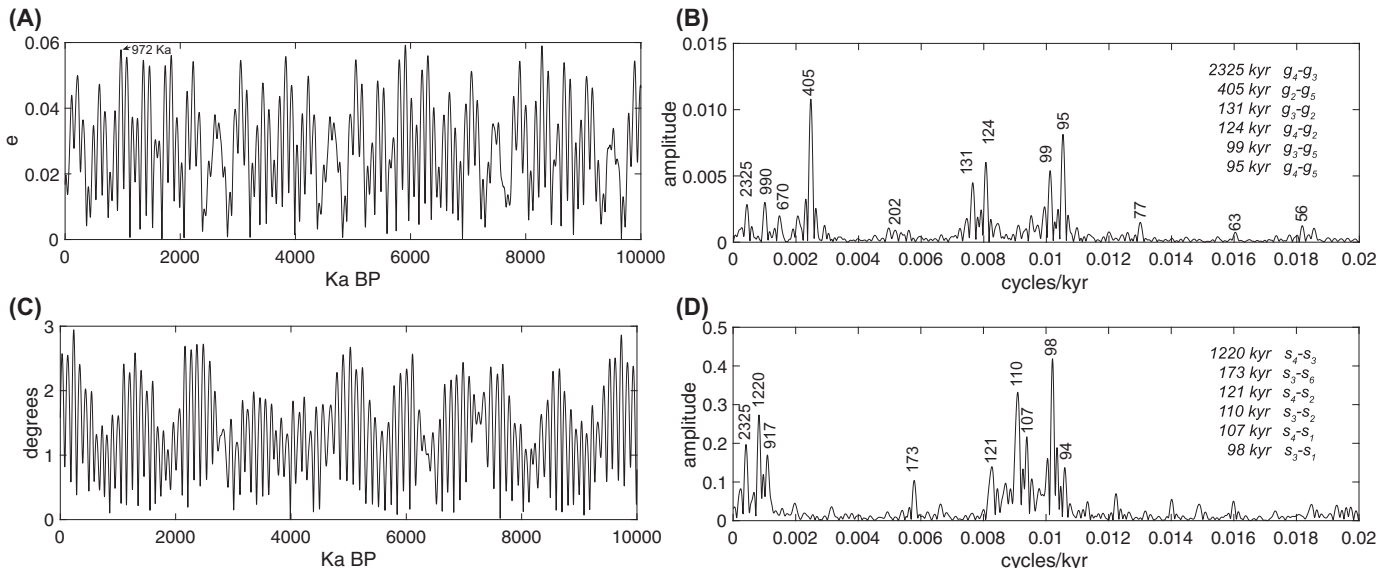


**Figure 2** Earth's orbital parameters from the La2010d astronomical solution (Laskar et al., 2011a). (A) The orbital eccentricity variation, 0–10 Ma. (B) Periodogram of the orbital eccentricity variation shown in (A). (C) The orbital inclination variation relative to the invariable plane, 0–10 Ma (Note: Fig. 6 in Laskar et al. (2004) shows La2004 orbital inclination relative to the *ecliptic* plane). (D) Periodogram of the orbital inclination variation shown in (C). Details for how to calculate A and C are provided in Appendix A.

for which the  $s_j$  are the contributing frequencies of the planetary orbital nodes. Values for  $p_3(t)$  and  $q_3(t)$  are explicitly provided for the La2010 solution (see [Appendix A](#)). For the La2004 solution, the modeled  $(h, k, p, q)$  values must be extracted using *insola,f* (subroutine Telor and its dependencies) (see URL in [Appendix A](#)). Orbital eccentricity has long been a major focus in cyclostratigraphy (e.g., [Section 1.4](#)), orbital inclination far less so until recently (e.g., [Section 3.2.2](#)).

### **1.1.2 Astronomical Solutions**

Originally, astronomical solutions were carried out analytically with trigonometric series approximations (e.g., [Le Verrier, 1855](#); [Stockwell, 1873](#); [Brouwer and van Woerkom, 1950](#); [Sharaf and Budnikova, 1967](#); [Bretagnon, 1974](#)). The advent of computers enabled solutions to be carried out by numerical integration, first for the outer planets (Jupiter to Pluto), which can be integrated over large steps, e.g., 40 days for Jupiter. Later the addition of the inner planets (Mercury to Mars) required integration over much smaller steps, e.g., 0.5 days ([Laskar, 1993](#)), and for a much larger number of combinations ([Ito and Tanikawa, 2007](#)). The first full Solar System solution (8 planets) involving numerical integration used averaged orbits and an integration step-size of 500 years (La1990 of [Laskar, 1990](#)). The La2004 solution was a “direct numerical integration of the gravitational equations” of the entire Solar System (8 planets plus Pluto) using a step-size of 0.005 years (=1.82625 days) ([Laskar et al., 2004](#)). It is valid (provides a unique solution) for 0 to 41 Ma. The La2010 solution ([Laskar et al., 2011a](#)) improved on La2004 by using a new, high-precision planetary ephemeris INPOP (Intégration Numérique Planétaire de l’Observatoire de Paris). It is valid for 0 to 50 Ma. Incorporating the asteroids Ceres, Pallas, Vesta, Iris and Bamberga ([Laskar et al., 2011b](#)) has led to the La2011 solution, also valid from 0 to 50 Ma ([Laskar et al., 2012](#)). New modeling by [Zeebe \(2017\)](#) provides unique solutions for 0 to 54 Ma. The time limitation of  $\sim$ 54 Ma is governed by the Lyapunov time of the Solar System, i.e., the timescale at which uncertainty in the planetary orbits increases by a factor of e, estimated to be approximately 5 Myr ([Laskar, 1989](#)).

### **1.1.3 Paleo-Astro dynamics**

The question of whether the motions of the planets have been stable through time has led to the discovery of chaotic zones ([Laskar, 1990](#)), to which the orbits of the inner planets are particularly susceptible ([Laskar, 2015](#)). One set of motions of quantifiable interest has been the secular

resonance between Earth and Mars, between their rotating orbital perihelia ( $g_4 - g_3$ ) and inclinations ( $s_4 - s_3$ ). Laskar's numerical models predict that for 0 to at least 50 Ma, the solutions for these two motions are in 2:1 resonance, and are manifested in the Earth's orbital eccentricity and obliquity variations as long-period modulations of 2.4 Myr and 1.2 Myr, respectively (Fig. 3A). This means that the Earth-Mars resonance state should be observable in the cyclostratigraphic record. The 1.2 Myr obliquity

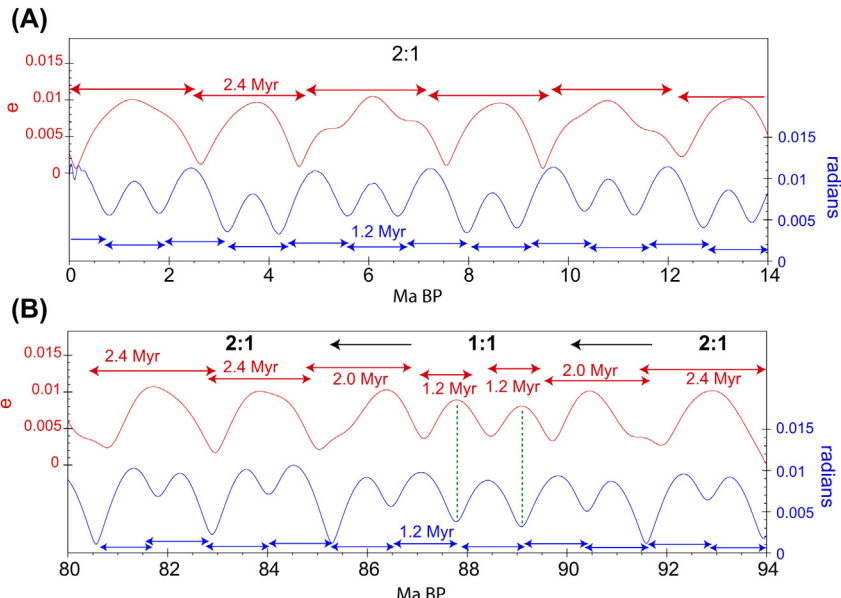


**Figure 3** Excerpts from the 0–250 Ma record of  $g_4 - g_3$  and  $s_4 - s_3$  modulations from the La2004 solution highlighting a chaotic interval between 80 Ma to 94 Ma. The  $g_4 - g_3$  modulations were extracted from the La2004 orbital eccentricity solution (Laskar et al., 2004) by Taner bandpass filtering (Kodama and Hinnov, 2015) with a lower cutoff frequency of 0.095 cycles/kyr, center frequency of 0.01025 cycles/kyr and upper cutoff frequency 0.0110 cycles/kyr; the filtered series was Hilbert-transformed to obtain the amplitude envelope, i.e., the modulations of interest. The  $s_4 - s_3$  modulations were extracted from the La2004 obliquity solution by Taner bandpass filtering with a lower cutoff frequency of 0.023 cycles/kyr, a center frequency of 0.0275 cycles/kyr and upper cutoff frequency of 0.032 cycles/kyr; the filtered series was Hilbert transformed to obtain the modulations. (A) The modulations for 0 to 14 Ma show a stable 2:1 secular resonance between the orbital motions of Earth and Mars, i.e., 2.4 Myr:1.2 Myr. (B) The modulations for 80 to 94 Ma are chaotic:  $g_4 - g_3$  modulations transition from a 2.4 Myr periodicity to a 1.2 Myr periodicity for two cycles, so that Earth-Mars orbital resonance to 1:1, then subsequently transition back to 2.4 Myr periodicity and 2:1 resonance.

modulation was discovered in Cenozoic cyclostratigraphy from ODP Leg 154 for a 10-Myr long interval spanning the Oligocene–Miocene boundary (Shackleton et al., 1999); later, the 2.4 Myr orbital eccentricity modulation was detected in the same data confirming that the Earth and Mars orbits were in the stable 2:1 resonance pattern as predicted by both La1993 and La2004 (Pálike et al., 2004).

The La2004 solution computed back to 250 Ma predicts that the most recent major chaotic transition took place from 83 Ma to 94 Ma. The modulation pattern for this interval (Fig. 3B) indicates that the  $g_4 - g_3$  modulation shortens starting at 92 Ma, first to a single 2 Myr cycle, then to 1.2 Myr cycling for two repetitions before transitioning back first to a single 2.0 Myr cycle and then to 2.4 Myr at 85 Ma. Importantly the  $s_4 - s_3$  modulation maintains a 1.2 Myr periodicity through the entire episode. This chaotic event has recently been detected in cyclostratigraphy of the Niobrara Formation (Western Interior Seaway) (Ma et al., 2017), and in the continental Songliao Basin (Wu et al., 2018a, 2018b), with a near-perfect fit to the characteristics of La2004 solution shown in Fig. 3B (The La2004 solution indicates another similar event between 78 Ma and 80 Ma, but involving only one 1.2 Myr cycle in the  $g_4 - g_3$  modulation.) It should be emphasized that astronomers are unconvinced that any of the astronomical solutions, including La2004, could be accurate much further back in time from 55 Ma, and so the Cretaceous empirical evidence may not constitute a validation of the La2004 model specifically. Nonetheless, the discovery of this ancient chaotic interval in cyclostratigraphy is a significant step forward for paleo-astrodynamics.

One of the lessons of the Cretaceous example is that tracking  $g_4 - g_3$  modulations only in cyclostratigraphy may be sufficient to identify Earth–Mars chaotic episodes. The stratigraphic amplification of the orbital eccentricity frequencies in the Triassic Newark Series and Inuyama Sequence (Section 2.2.3) brings to light very long-period 1.6 Myr to 1.8 Myr cycles ascribed as a direct contribution of  $g_4 - g_3$  to the orbital eccentricity variation (not as modulator of the short orbital eccentricity) (Olsen and Kent, 1999; Ikeda and Tada, 2013). A 1.75 Myr cycle persists throughout the Newark Series, which suggests that the Earth–Mars orbits were in 1:1 resonance for an extended time of at least 22 Myr during the Late Triassic Period (see Fig. 16 in Olsen, 2010).

Other recent attempts to isolate possible  $g_4 - g_3$  and  $s_4 - s_3$  modulations have been made for Paleozoic cyclostratigraphy. The 13 Myr-long Late Permian section from Meishan and Shangsi (South China) do not reveal

clearly recognizable modulations; slowly shifting depositional environments may have interfered with the rock magnetic proxies used in the study (Wu et al., 2013). Early-Middle Permian cyclostratigraphy at Shangsi (China) shows signs of 2:1 resonance, but both interpreted  $g_4 - g_3$  and  $s_4 - s_3$  periodicities are slightly shorter than 2.4 Myr and 1.2 Myr (Fang et al., 2017). In the Chinese Carboniferous, a 2:1 to 1:1 resonance transition from the Serpukovian to Moscovian was detected in joint  $g_4 - g_3$  and  $s_4 - s_3$  modulations from magnetic susceptibility measurements of the Luokun section (South China; Fang et al., 2018). These reports are being made whenever very long cyclostratigraphic sections are at hand, and so are opportunistic in nature. That said, the most critical geologic periods to investigate for Solar System chaos are those closest to the terminus of the astronomical model accuracy, i.e., back in time from 55 Ma, and in light of the Cretaceous evidence above, from 55 Ma to 80 Ma. Finally, the establishment of firm times of resonance transitions from cyclostratigraphy will be the key to identifying the best astronomical solution (Zeebe, 2017).

## 1.2 Geodynamics –Precession and Obliquity

### 1.2.1 Luni-Solar Precession

The Earth's luni-solar precession arises from the angle  $\varepsilon$  of the Earth's rotational axis with respect to the ecliptic plane, its equatorial bulge due to rotational effects on the non-rigid Earth, and by gravitational attraction from the Moon and Sun and the other planets on the equatorial bulge (Fig. 4). Astronomers refer to the Earth's obliquity as “inclination of the ecliptic to the equator”, or “obliquity of the ecliptic”, and the Earth's luni-solar precession as the “luni-solar precession of longitude” or (the major component of) “precession of the equator” (Dehant and Capitaine, 1997). The annually averaged luni-solar precession rate is (see Appendix C for variable definitions):

$$p_{\odot+c} = \frac{3}{2} \left( \frac{G}{\phi} \right) H \left[ \frac{m_{\odot}}{a^3} (1 - e^2)^{-3/2} + \frac{m_c}{a_c^3} (1 - e_c^2)^{-3/2} \left( 1 - \left( \frac{3}{2} \right) \sin^2 I_c \right) \right] \cos \varepsilon \quad (4)$$

The variable  $p_{\odot+c}/\cos \varepsilon$  is designated as the “precession constant”  $\alpha$  in Eq. (8) of Laskar et al. (2004). Other smaller contributions to the total “precession of the equator” are summarized in Fig. 1 of Dehant and Capitaine (1997) and Table 3 of Williams (1994). For the International

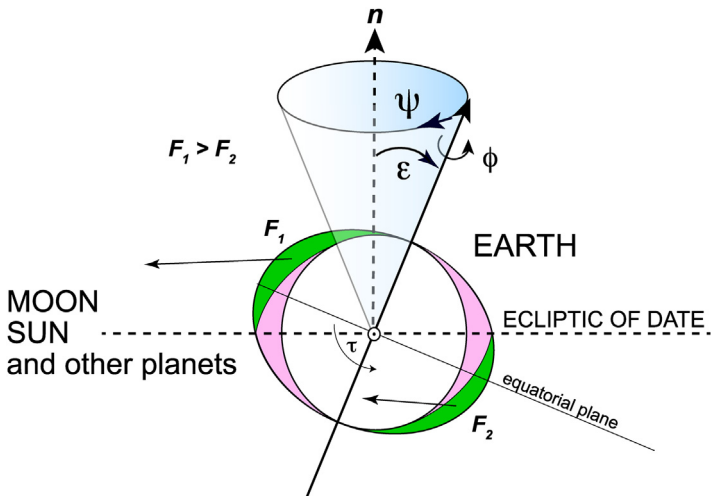


**Figure 4** The Earth's rotational axis is tilted with respect to the ecliptic of date normal  $n$  at an obliquity angle  $\epsilon$ ; Earth's rotation  $\Omega$  is anti-clockwise. The rotation raises a permanent equatorial bulge at right angles to the rotation axis (shown in green and pink). The equatorial bulge experiences gravitational forces  $F_1$  and  $F_2$  from the attracting bodies of the Moon, Sun and (to a much lesser extent) other planets (Note: Moon's orbit is presently inclined by  $I_C = 5.15^\circ$  relative to the ecliptic.). The pink areas line up in the direction of gravitational forcing, experience equal but opposite torques, and cancel out. The green areas, however, are offset from the direction of forcing; the bulge closest to the attracting bodies experiences greater forcing so that  $F_1 > F_2$ . This inequality leads to a net torque  $\tau$  along a line in the equatorial plane that is normal to both the forcing direction and Earth's rotation axis. This torque generates an additional component of angular momentum on the Earth that is parallel to  $\tau$ , changing the direction of the rotation axis. This leads to clockwise precession  $\psi$  of the rotation axis, which varies with the changing positions of the attracting bodies with respect to the equatorial bulge (e.g., at Spring Equinox  $\tau = 0$ ), with an annually averaged value of approximately 50 arcseconds/year (see Appendix C). From Dehant and Mathews (2015) and Lowrie (2007).

Astronomical Union 1976 System of Astronomical Constants (IAU76),  $\epsilon = 84381.448 \text{ arcseconds} = 23.43929^\circ$ , and  $p_{\odot+C} = 50.40736050 \text{ arcseconds/year}$ , or 1 cycle/(25,711 years). Astronomers continue to refine the precession model with improvements to the Solar System ephemerides and geophysical observations (Liu and Capitaine, 2017). The La2004 solution gives 50.475838 arcseconds/year, denoted as “p”, e.g., Eq. (40) in Laskar et al. (2004), corresponding to 1 cycle/(25,676 years). Owing to the continuously revolving positions of the Moon and Earth with respect to the Sun, current instantaneous  $p_{\odot+C}$  ranges from 0 (at the

equinoxes) to as high as 115 arcseconds/year, varying with fortnightly and semi-annual tidal periodicities (Fig. 4 in [Edvardsson et al., 2002](#)).

### 1.2.2 Precession and Obliquity Equations

Planetary perturbations to the ecliptic plane, thus to the Earth's precession  $\psi$  and obliquity  $\epsilon$ , are accounted for by the coupled precession and obliquity equations ([De Surgy and Laskar, 1997](#), Eq. (6) in [Laskar et al., 2004](#)):

$$\begin{aligned} \frac{dX}{dt} &= L \left( 1 - \frac{X^2}{L^2} \right)^{\frac{1}{2}} (\mathcal{B}(t) \sin \psi - \mathcal{A}(t) \cos \psi) \\ \frac{d\psi}{dt} &= \frac{\alpha X}{L} - \frac{X}{L \left( 1 - \frac{X^2}{L^2} \right)^{\frac{1}{2}}} (\mathcal{A}(t) \sin \psi + \mathcal{B}(t) \cos \psi) - 2\mathcal{C}(t) \end{aligned} \quad (5)$$

where  $X = \cos \epsilon$  and  $L = C\phi$ ,  $\alpha = p_{\odot+\subset} / \cos \epsilon$ , and  $\mathcal{A}(t)$ ,  $\mathcal{B}(t)$  and  $\mathcal{C}(t)$  give time-dependent variations to the ecliptic plane caused by planetary perturbations, modeled by the astronomical solution ([Appendix C](#)).

The “solution of order zero” for the Earth's precession due to the Moon and Sun with no planetary disturbances, hence a constant obliquity  $\epsilon$ , is (Eq. 27 in [Laskar et al., 2004](#)):  $\psi = \psi_0 + pt$ , where  $p = p_{\odot+\subset}$ . Higher order solutions to account for the planetary contributions take the form of (Eq. 34 in [Laskar et al., 2004](#)):

$$\psi = \psi_0 + pt + p_1 t^2 + \text{other terms} \quad (6)$$

where  $\psi_0 = 49086 \text{ arcsec}$  and  $p_1 = -13.526564 \text{ arcsec/year}^2$ .

### 1.2.3 Tidal Dissipation and Dynamical Ellipticity

The Earth's rotation rate depends on tidal dissipation and mass redistribution ([Lambeck, 1980](#)). Tidal dissipation arises from anelastic response of the Earth to the tidal forces generated by the Sun and Moon (p. 290, [Lambeck, 1980](#)). The fluid (ocean) and anelastic (solid Earth) tidal responses result in a time delay in the net position of the tidal bulge relative to the Earth-Moon axis, the bulge leads the axis by a small angle  $\delta$  (e.g., Fig. 4 in [Wahr, 1988](#)). A torque in the opposite direction of the Earth's rotation is raised between the Moon and the leading bulge, causing continuous rotational deceleration. Evidence from paleontology and tidalites confirms that the Earth's rotation rate has decreased over the past 2 Ga, and also that the deceleration was variable, apparently even reversing sign over at least one interval ([Fig. 5](#)).

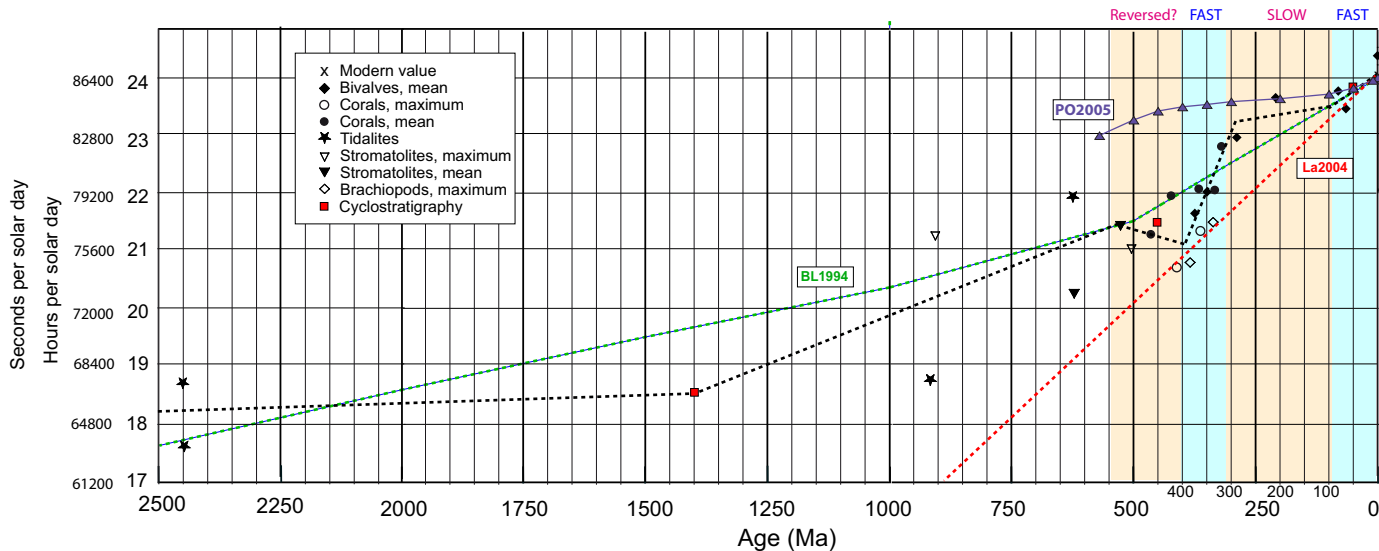


**Figure 5** Evolution of Earth's rotation. Data are redrawn from Williams (2000) who compiled data from Scruton (1978), Berry and Barker (1968), Wells (1970), Mazzullo (1971), Pannella (1972), and Vanyo and Awramik (1985). Data from cyclostratigraphy are from Meyers and Malinverno (2018). Results from the paleo-tidal model of Poliakov (2005) are also shown (purple triangles and line). The red dashed line indicates the Lunar Laser Ranging based empirical model assumed by Laskar et al. (2004) for the La2004 solution, and is extrapolated back in time until the model indicates 17 h LOD; the green dashed line indicates the paleontological model assumed by Berger and Loutre (1994), which averages through the paleontological and tidalite data.

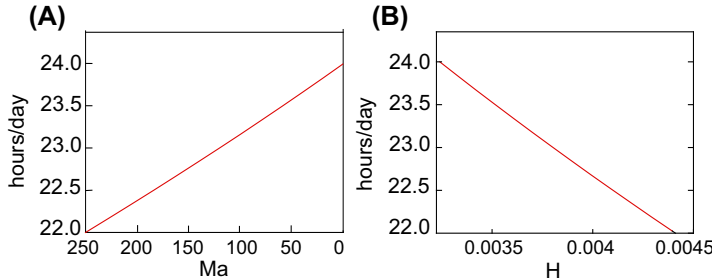


**Figure 6** Dynamical ellipticity and rotation rate. (A) Lunar Laser Ranging measurements of 3.82 cm/year lunar recession ([Dickey et al., 1994](#)), biased slightly to 3.89 cm/year ([Laskar et al., 2004](#)), corresponds to a decrease in length-of-day of 2.68 milliseconds/century extrapolated back in time to 250 Ma. (B) Dynamical ellipticity  $H$  obtained by Eq. (6).

The Earth's shape is ellipsoidal and dynamic, commonly referred to as "dynamical ellipticity" (or "dynamical oblateness"), and depends on the Earth's rotation rate, internal density and the consequent gravitational and centrifugal force balances. It is characterized largely by rotational flattening of the poles, and has been approximated as (Eq. 9 in [Berger and Loutre, 1994](#); related discussion on hydrostatic flattening on p. 28 in [Lambeck, 1980](#)) ([Fig. 6](#)):

$$H = (C - A) / C = 6.094 \times 10^5 \times \phi^2 \quad (7)$$

where  $A$  and  $C$  are Earth's equatorial and polar moments of inertia, and  $\phi$  is Earth's rotation rate (see [Appendix C](#) for values).  $H$  can also be affected by mass redistribution, e.g., ice sheets that can result in "climate friction", which contributes to changes in rotation rate and could potentially even lead to resonance with the orbital parameter related to  $s_6 - g_6 + g_5$  ([Laskar et al., 1993](#)).  $H$  is fast-varying, contributing time-variable changes to  $p$  on the order of 1% per 100,000 years ([Thomson, 1990](#)).  $\phi$  is slow-varying, contributing deep-time, secular changes in  $p$  on the order of 1% per 50 million years ([Denis et al., 2002](#)).

#### 1.2.4 Paleo-Geodynamics

The importance of Earth's rotational dynamics in Milankovitch cycles rose to prominence during early efforts to estimate length-of-day (LOD) and Earth-Moon distance from ancient corals, mollusks and stromatolites, and sedimentary tidalites ([Fig. 5](#)). In a groundbreaking paper, [Walker and Zahmle \(1986\)](#) invoked an astronomical origin, namely the lunar nodal cycle, to

explain the origin of 23:1 iron-silica lamination bundling patterns in the 2.5 Ga Weeli Wollu Formation of Australia (Trendall, 1973), for which each lamination pair was assumed to represent a varve. At 2.5 Ga, the lunar nodal cycle would have been significantly longer than its present-day 18.6-year period due to a shorter 0.86 of present-day Earth-Moon distance. They further proposed that an independent determination of their estimate could be made from coeval Milankovitch cycles, which they predicted would have had periodicities of 17 kyr for obliquity and 13 kyr for precession. 2.5 Ga Milankovitch cycles have not yet been firmly established (although see Section 2.4.3), but a recent study of Proterozoic Milankovitch cycles estimates 0.887 of present-day Earth-Moon distance at 1.4 Ga (Section 2.4.2; Meyers and Malinverno, 2018; see also Fig. 5). The Weeli Wollu Formation was later reassessed by Williams (1989) to have 28–30 laminae per bundle, and indicative of tidalites, but the suggestion by Walker and Zahnle (1986) that Milankovitch cycles could serve as a validation tool has remained intact.

The dependence of the precession and obliquity equations (Eq. 5) on  $p_{\odot+c}$  (Eq. 4), which is defined by Earth's rotation rate and shape, was merged with the paleontological and tidalite evidence for shorter LOD in the geologic past, an Earth flattening model (Eq. 9), and lunar recession to estimate Milankovitch cycle periodicities from 0–500 Ma (Berger et al., 1989; Loutre et al., 1990; Berger et al., 1992) and later to 2.5 Ga (Berger and Loutre, 1994). This was followed by inclusion of adjustable tidal dissipation (TD) and dynamical ellipticity ( $E_D$ ) variables in the La1993 and La2004 astronomical solutions (Laskar et al., 2004), while the La2004 solution adopted values based on present-day Lunar Laser Ranging observations of lunar recession. These variables were exploited in testing the power of Milankovitch cycles to solve these two unknowns for the Cenozoic (Pälike and Shackleton, 2000; Lourens et al., 2001; Zeeden et al., 2014). The results suggested that the La2004 model conforms well with Cenozoic cyclostratigraphy, suggesting that over the past 25 Myr, paleo-geodynamics was operating with present-day magnitudes (La2004 red dashed line in Fig. 5).

More recently an effort was made to estimate uncertainties imposed by paleo-geodynamics on Milankovitch cycles back to 700 Ma (Waltham, 2015); this work was motivated by a much lower tidal dissipation energy than present-day required by conditions surrounding the time of origin of the Moon. This requirement is supported by models of the early Eocene Ocean indicating much lower tidal dissipation compared with present-day

(1.44 TW for early Eocene vs. 2.78 TW for present day) (Green and Huber, 2013), with additional modeling for the Cretaceous (2.1 TW) and Permo-Triassic transition (0.9 TW) (Green et al., 2017), and by Poliakov (2005). Together with the observational evidence (black dashed line in Fig. 6) the modeling indicates a more slowly decreasing LOD from 250–50 Ma.

The Milankovitch record over this time, by contrast, appears to indicate obliquity cycle periodicities, in particular, that conform to the faster La2004 TD-ED model, indicating 35 kyr obliquity at 245 Ma (Anisian; Li et al., 2018a), 32.7–32.9 kyr obliquity at 250–251 Ma (Griesbachian; Li et al., 2016); and a slight lengthening to 34-kyr at 252–260 Ma (Wuchiapingian-Changhsingian; Wu et al., 2013). In a new extraordinary 34 Myr-long section from the Chinese Carboniferous (Shangruya, Huashiban, Dala and Maping formations), there is evidence for an obliquity cycle evolving from a 30.5–30.7 kyr period at the base of the sequence, in the Visean-Bashkirian (333–315 Ma), to a 31.4 kyr period at the top of the sequence, in the Gzhelian (300 Ma) (Wu et al., 2018a, 2018b). A short 2 Myr long section from the late Bashkirian Copacabana Formation (Bolivia) analyzed with ASM (Section 3.5.2) supplemented with an optimization on  $k$ , indicates  $k = 58.7 \text{ arcsec/kyr}$  (Ma et al., 2018). Assuming present-day  $s_4 = -17.755 \text{ arcsec/year}$  and  $s_3 = -18.850 \text{ arcsec/year}$  yields main obliquity periodicities of 31652 years and 32522 years, and a 22 h LOD. These periodicities are slightly longer than those estimated from the Chinese data; application of the same optimization procedure developed by Ma et al. might reconcile the differences. Finally, a more detailed optimization on  $k$  and  $g_i$  (“timeOptMCMC”, Section 3.5.4) for the 1.4 Ga Xiamaling Formation (China) yielded  $k(=p) = 85.790450 \text{ arcsec/year}$ , corresponding to an 18.68-h LOD (Meyers and Malinverno, 2018).

### 1.3 Milankovitch Cycles and Paleoclimate Responses

The promise of cyclostratigraphy to yield information about Solar System dynamics has in recent years, in the rush simply to identify astronomical signals, deemphasized research into the paleoclimatic response to astronomical forcing. Understanding the paleoclimatic response begins with the insolation equation: in particular, the insolation has very weak direct contributions from the Earth’s obliquity and orbital eccentricity variations. There is no precession variation inherent to global insolation; nonlinear and threshold responses of the climate are required to generate precession

index signals in insolation-forced climate change. Additional filtering takes place when climatic change is registered in the stratigraphic record (Sections 1.3.2 and 1.4).

### 1.3.1 The Insolation Equation

The solar irradiance has a major daily cycle due to the Earth's rotation, and a strong annual cycle due to the Earth's revolution around the Sun. The solar irradiance reaching any geographic location on Earth (see Fig. 6 in [Hinnov, 2013](#)) is given by the “insolation equation”:

$$W = (S_0/r^2) \cos z = (S_0/r^2) (\sin\theta \sin\delta + \cos\theta \cos\delta \cos\alpha) \quad (8)$$

Earth-Sun distance  $r$  depends on the orbital eccentricity and time of year, and solar declination angle  $\delta$  depends on the obliquity;  $S_0$  is the solar constant (in  $\text{W}/\text{m}^2$ ),  $z$  is angle of the Sun in the local sky relative to the local zenith point,  $\theta$  is the geographic latitude of the location, and  $\alpha$  is the hour angle of the Sun in the local sky, where  $\alpha = 0$  is at the meridian (local midday).

Eq. (8) was introduced by [Meech \(1856\)](#), who implemented elliptic integrals to accurately position the Earth on its orbit. Meech also considered obliquity and orbital eccentricity effects (based on Le Verrier) on insolation for specific values, concluding that both were insufficient to drive significant climate change. [Pilgrim \(1904\)](#) provided a 1-myrs long calculation of the combined orbital eccentricity, obliquity and precession on insolation, based on the [Stockwell \(1873\)](#) astronomical solution (Appendix B). Finally, a comprehensive theory of astronomically forced insolation was completed, first using Pilgrim's values ([Milankovitch, 1920](#)), and later comparing this with the (Le Verrier-based) astronomical solution of [Miskovitch \(1931\)](#) in ([Milankovitch, 1941](#)) (see reproduction in Fig. 2 of [Loutre, 2003](#)).

FORTRAN codes for computing insolation were introduced by [Berger \(1978\)](#) and [Laskar et al. \(1993\)](#). A myriad of important insolation calculations was discussed in [Berger et al. \(1993\)](#), including instantaneous insolation (irradiance, in  $\text{W}/\text{m}^2$ ), integrated insolation (irradiation, in  $\text{J}/\text{m}^2$ ), and zenith-class distance. The freeware *Analyseries* ([Paillard et al., 1996](#)) calculates insolation with options for three astronomical solutions. [Huybers \(2006\)](#) adapted the [Berger \(1978\)](#) FORTRAN code into the MATLAB script *daily\_insolation.m*. The MATLAB GUI *Earth Orbit v2.1* enables detailed visualization of the astronomical parameters and insolation ([Kostadinov and Gilb, 2014](#)). [Berger et al. \(2010\)](#) compared elliptical integral versus summation methods for accurate integrating insolation over

time intervals along the Earth's orbit, with code recently made available in *palinsol* for R (Crucifix, 2016).

Calculating Eq. (8) with hourly  $dt$  obviously resolves the diurnal cycle; hourly  $dt$  would be needed when evaluating zenith-class insolation (Berger et al., 1993) when a climate response is expected for a limited range of solar angles in the sky, e.g., a west-facing mountain glacier. Monthly  $dt$ , resolving the seasonal cycle of insolation, reveals some surprises (Fig. 7). The seasonal (annual) cycle undergoes small interannual modulations forced by different astronomical parameter contributions throughout the year. At 65° North, winter insolation is modulated by the obliquity, spring (or fall) insolation is modulated by the precession index only, and summer insolation by a combination of obliquity and precession index variations. Moreover, from month to month, the phase of the precession index shifts by 30° increments, the consequence of each month occurring at a different point along the Earth's orbit. Other significant implications of this annually resolved insolation calculation are discussed at length in Section 1.3.2 below.

Inter-annually sampled insolation (for  $dt \gg 1$  year) resolves the astronomical parameters only, notably the latitudinal dependence of obliquity forcing as shown for June 21 at different Northern latitudes (Fig. 8). Obliquity forcing increases poleward, jumping up dramatically from 60° N to 80° N (i.e., across the Arctic Circle at 66° N), although never exceeding the amplitudes of the precession index. Also, the summer insolation increases from an average of 400 W/m<sup>2</sup> at the Equator to 525 W/m<sup>2</sup> at 80° N, due to more daylight hours with increasing latitude (up to 24 h north of the Arctic Circle). Finally, the Earth's orbital eccentricity plays a minuscule role in the direct forcing of insolation (see Section 1.4 for discussion on the dominance of orbital eccentricity signals in cyclostratigraphy).

### 1.3.2 Paleoclimate Responses

The annually resolved insolation calls attention to a long-standing dilemma in Milankovitch theory: the seasonal cycle of insolation (at 65° N) has an amplitude of more than ±200 W/m<sup>2</sup> (Fig. 7C), whereas the Milankovitch cycles have amplitudes of up to ±15 W/m<sup>2</sup> (for the obliquity) and up to 20 W/m<sup>2</sup> for the precession index (Fig. 8B), and occasionally at most, at 80° N, ±75 W/m<sup>2</sup> (peak-to-peak) amplitudes (Fig. 8A). By this measure, the amplitude of the astronomically forced insolation variations are only about a 10th of the amplitude of the seasonal insolation. Thus, the

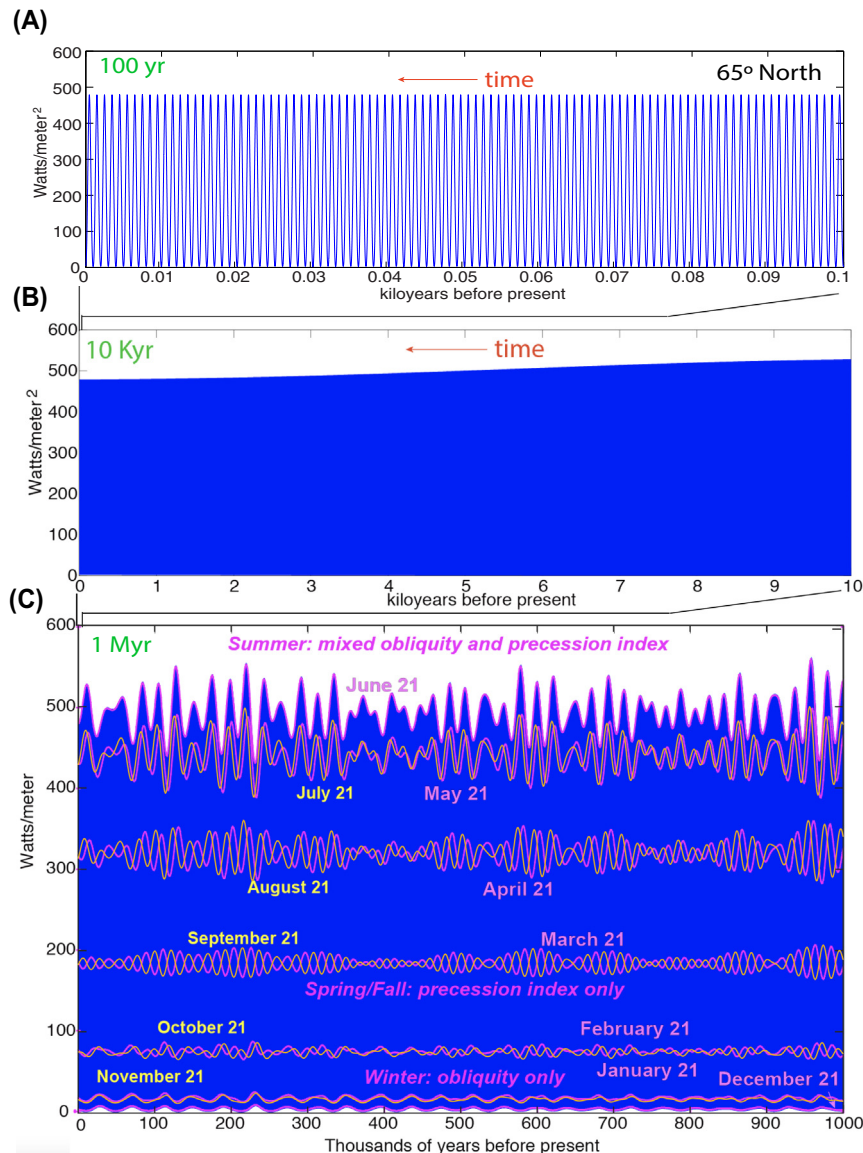


**Figure 7** Daily insolation at 65° North calculated at  $\Delta t = 0.0822$  yr (30 day) time steps using the MATLAB script *daily\_insolation.m* (Huybers, 2006), with modifications (The mean value of  $k$  is maintained throughout the year in this calculation, and not changed as required by the lunar orbit, as mentioned in Section 1.2.1). (A) The most recent 100 years, showing a strong seasonal cycle in insolation. (B) The most recent 10 kyr, revealing a long-term change in the insolation cycle maxima. (C) The most recent 1 Myr, which shows astronomically forced maxima and minima (June 21 and December 21, respectively) in the Northern Hemisphere insolation cycles.

characterization of insolation at the interannual scale only (as in Fig. 8) does not acknowledge that the majority of insolation power is in the seasonal cycle.

Therefore, the modulations of the seasonal cycle of insolation must be the source of astronomically forced climate change. A simple model of how astronomically forced climate variations could come to dominate the paleoclimate record is shown in Figs. 9 and 10:

- (1) The seasonal insolation, taken as the driver of the climate system and shown for the past 5 years (Fig. 9Aa), has an annual-band spectrum (Fig. 9B) with a major peak at 1 cycle/year, and small side-band peaks at  $1 \pm 1/(54 \text{ kyr})$ ,  $1 \pm 1/(41 \text{ kyr})$  and  $1 \pm 1/(29 \text{ kyr})$  from the modulation by the obliquity variation, and a very small side-band peaks at  $1-1/(23\text{kyr})$  and  $1-1/(9\text{kyr})$  from modulations by the precession index, which are one-sided due to the uni-directional counter-clockwise motion of the precession along the annual orbit (Fig. 1). The power spectrum across all frequencies (Fig. 10A) confirms that the annual spectral peak contains the majority of the power; there is a well-defined, but very low-power peak in the obliquity band, approximately 4 orders of magnitude lower than the annual power.
- (2) A “threshold climate” response to the seasonal insolation would involve a ‘threshold’ insolation below which the climate system does not respond (is “insensitive”); above this threshold, the climate responds linearly to the insolation (Fig. 9C). For example, there may be a minimum insolation required to trigger marine productivity or warm the ocean surface layer. This produces a paleoclimate proxy that is a “half-rectified” version of the insolation. The annual-band spectrum shows a slight strengthening of the obliquity- and precession-induced side-bands with respect to the annual peak (Fig. 9D). The power spectrum across all frequencies (Fig. 10B) shows an annual peak that is slightly diminished in power (reflecting the near-halving of the annual cycle amplitude by the threshold), but now in addition to obliquity power there is precession index power at a comparable level,

---

The magenta and light orange curves indicate daily insolation for specific calendar days in the year, revealing the familiar astronomical variations, with a mix of precession index and obliquity variations affecting insolation maxima (June 21), precession index only at spring (or fall) equinox (March 21 or September 21), and obliquity affecting insolation minima (December 21), and a shifting phase of the precession index variations (see text).

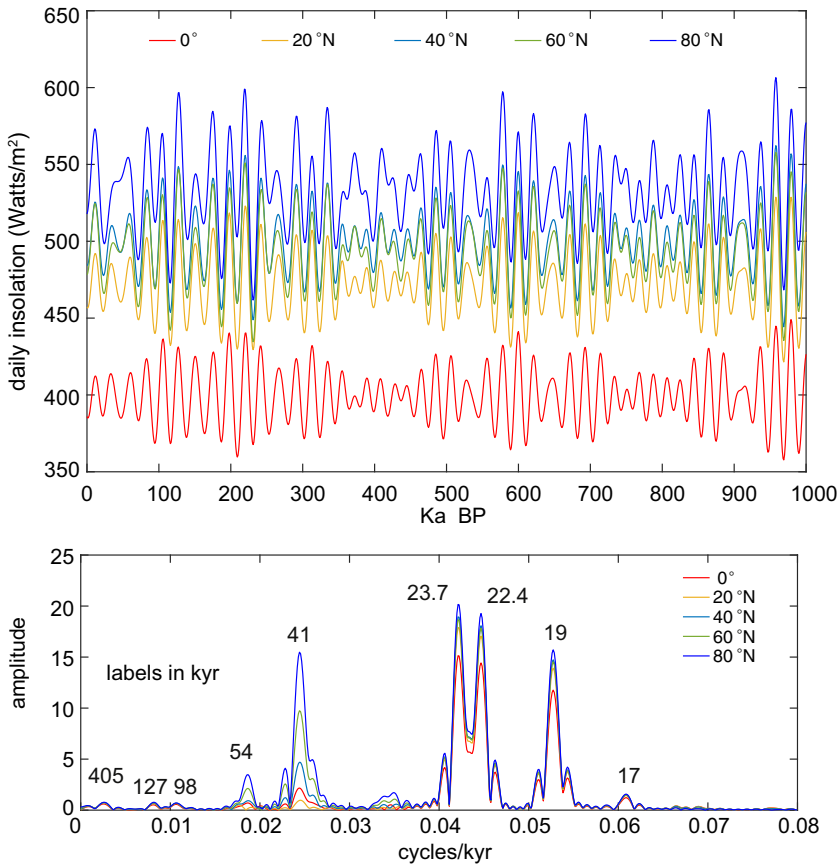


**Figure 8** Mean daily insolation at June 21 (northern Summer Solstice) for latitudes 0°, 20° N, 40° N, 60° N and 80° N. (A) Insolation sampled at  $\Delta t = 1$  kyr for 0 to 1 Ma using the La2004 astronomical solution. (B)  $2\pi$  multitaper amplitude spectra of the insolation time series shown in (A). All calculations were carried out in *Analyseries 2.0.8* (Paillard et al., 1996).

albeit both have significantly less power than the annual frequency, which is still nearly 4 orders of magnitude higher in power.

- (3) A “mixed climate” response might additionally respond non-linearly to the insolation above the threshold level envisioned above (Fig. 9E). For example, there could be disruptions to ocean surface layer processes from ocean-atmospheric dynamics causing delays, or stochastic weather responding rapidly to rising insolation. The annual-band spectrum (Fig. 9F) now shows obliquity and precession index side-bands on both sides of the annual frequency, which maintains dominant power. However, in the power spectrum across all frequencies (Fig. 10C)

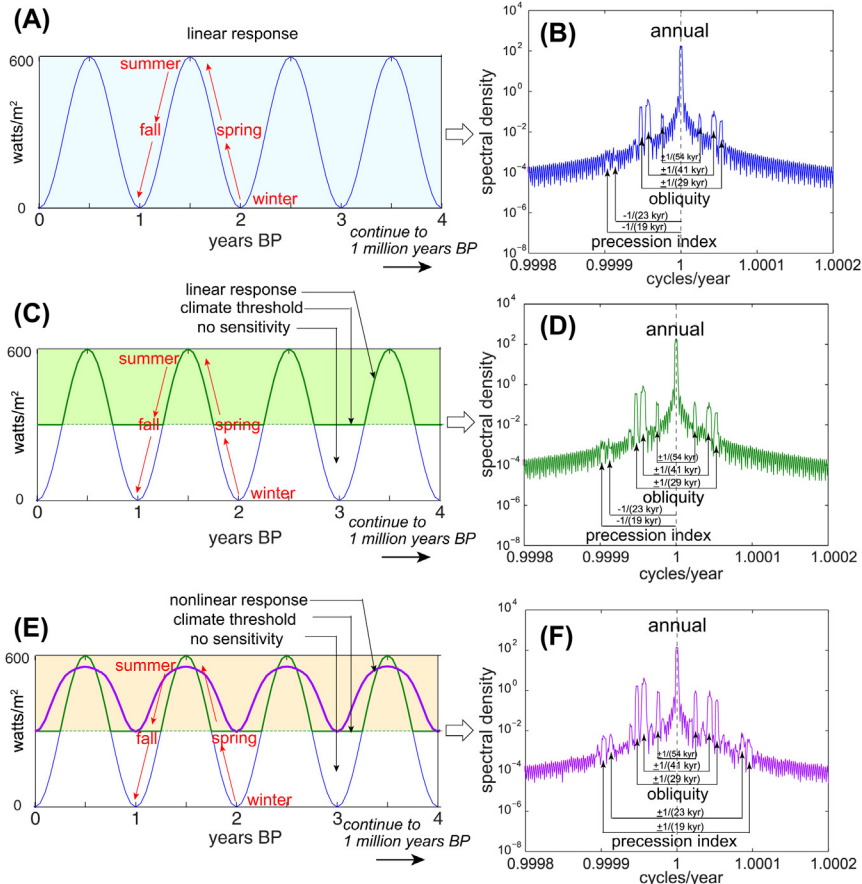


**Figure 9** Conceptual climate responses to insolation forcing at 65° North, past 4 years,  $\Delta t = 30$  days ( $=0.0822$  years). (A) *Linear climate*: Solar irradiance at the top of the atmosphere is the driver of a linearly responding climate system; (B) Power spectrum of a calculated for 0–1 Ma. (C) *Threshold climate*: half-wave rectification (green curve) truncating the seasonal insolation cycles (blue curve) below a threshold (dashed green line) to simulate a threshold insolation required, for example, to trigger marine productivity, or to warm the ocean surface layer. (D) Power spectrum of c calculated for 0–1 Ma. (E) *Mixed climate*: Half-wave rectified seasonal insolation cycles (green curve from B) with amplifications, delays and other nonlinearities (purple curve), for example, to simulate disruptions to ocean surface layer processes from ocean-atmosphere dynamics, weather, etc. (F) Power spectrum of E calculated for 0–1 Ma.

obliquity and precession index power is now only approximately 1 order of magnitude lower than the annual power; also, obliquity power exceeds precession index power, which is normally accomplished with time-integrated insolation (e.g., Huybers, 2006; Berger et al., 2010).

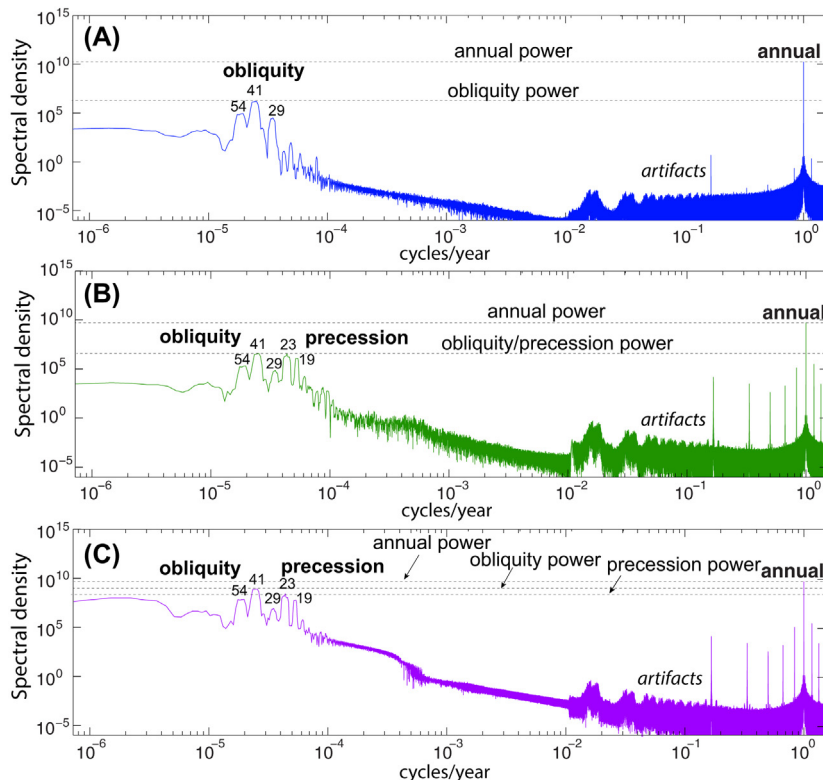


**Figure 10** Power spectra of climate responses to  $65^\circ$  N insolation for 0 to 1 Ma presented in Fig. 8. (A) Linear climate response; (B) threshold climate response; (C) mixed climate response. The horizontal dashed lines indicate power level of the annual, obliquity and precession index frequencies; “artifacts” are likely due to time sampling errors (there are no signal components in the spectrum between the annual and astronomical frequency bands).

## 1.4 Stratigraphic Record of Milankovitch Cycles

While climate is fast-acting and seasonal, its sedimentary record typically involves “filtering” through a much slower system of responses. Some depositional environments have accumulation rates that preserve seasonality in varved sequences, with accumulation rates on the order of a 1–10 mm/year. However, these environments tend not to operate long enough to preserve astronomical timescales, i.e., they fill up quickly. However, there are a few exceptions, e.g., the sequence of 200,000 evaporite varves of the Castile Formation (Ochoan, late Permian) (Anderson, 2011). The vast majority of depositional systems have much lower

accumulation rates, on the order of 1 to 10 cm/kyr, which biases the sedimentary record to preservation of the Milankovitch cycles. Below additional transformations of Milankovitch cycles are described, to explain how orbital eccentricity (405 kyr and  $\sim$ 100 kyr) cycles come to dominate cyclostratigraphy.

#### 1.4.1 Rectification Effects

Consider a threshold climate (see [Section 1.3.2](#)) that registers only the mean of June and July insolation in the seasonal cycle every year; this would result in an interannual climate forcing signal ([Fig. 11A](#), with a power spectrum showing major power at precession index frequencies, and moderate-low power at the obliquity frequencies ([Fig. 11B](#)). Suppose that there is a sedimentation response only when insolation is greater than the mean value ([Fig. 11C](#)); this “clipping” imposes a half-rectification on the climate signal that will be recorded in the sediment. Its power spectrum shows the appearance of difference tones in the orbital eccentricity frequencies and addition tones at high frequencies ([Fig. 11D](#)). Sedimentation of the climate proxy (which assumes the insolation values) now takes place, with a 1 cm/kyr sedimentation rate whenever insolation is above the mean value, and 0 cm/kyr otherwise, squeezing the signal as it takes on its stratigraphic form ([Fig. 11E](#)), which amplifies the difference tones (the orbital eccentricity frequencies) and suppresses the 1/(19 kyr) precession index frequency and the addition tones ([Fig. 11F](#)). Also of some surprise is amplification of the 1/(54 kyr) obliquity frequency. Finally, sediment mixing (e.g., bioturbation) is simulated for a 10-cm depth ([Fig. 11G](#)), which further amplifies the orbital eccentricity frequencies ([Fig. 11H](#)), and for a 20-cm depth ([Fig. 11I](#)), which in this case almost completely eradicates the precession index ([Fig. 11J](#)). This nonlinear sedimentation and mixing model is similar to the one proposed by [Ripepe and Fischer \(1991\)](#) to explain the strong orbital eccentricity frequencies and near absent precession index frequencies in the Lower Cretaceous pelagic Scisti a Fucoidi ([Section 2.2.1](#)).

#### 1.4.2 Variable Accumulation Rates

Stratigraphic time scales are notoriously difficult to determine owing to variable sedimentation rates through time. These rates can have random fluctuations, secular trends, and even cyclic variations, and can defocus and obscure what would otherwise be detected as a clear astronomical signal. The synthetic example shown in [Fig. 12](#) illustrates the strong distorting

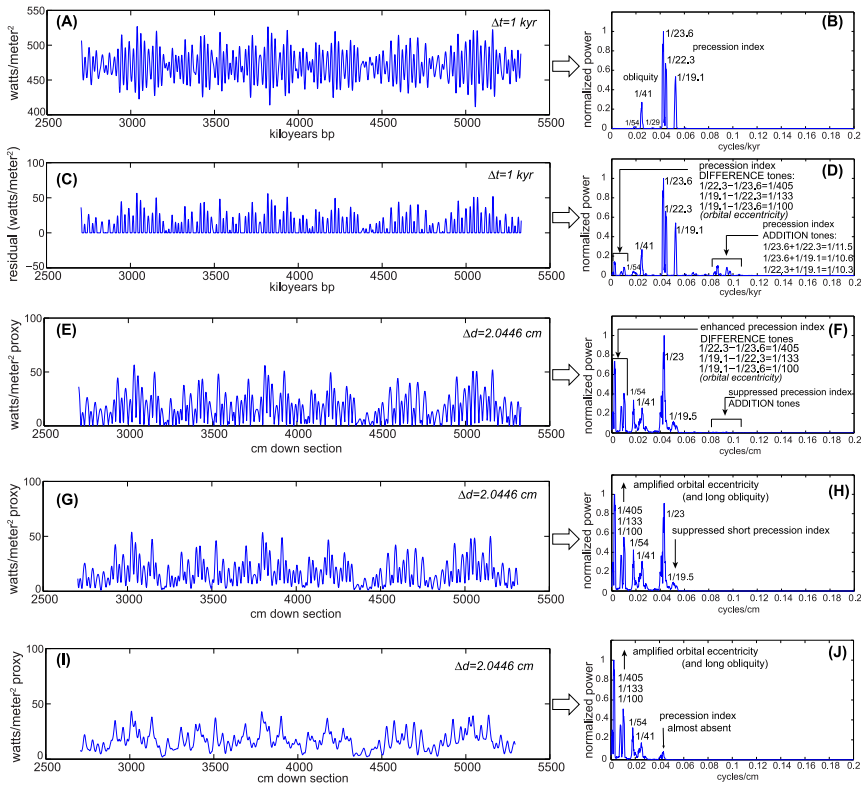


**Figure 11** Stratigraphic enhancement of orbital eccentricity in cyclostratigraphy. (A) Mean June–July insolation at 65° North with La2004 solution from 2.706 Ma to 5.329 Ma, calculated at  $dt = 1$  kyr using Analyseries (Paillard et al., 1996). (B)  $2\pi$  multitaper power spectrum of A. (C) Insolation from A, half-rectified to simulate sedimentation response for insolation greater than the mean value of  $470 \text{ W/m}^2$ , reset to zero in the plot. (D)  $2\pi$  multitaper power spectrum of C showing redistribution of power into the difference tones and addition tones of the precession index frequencies. (E) Conversion of C into stratigraphy assuming a  $1 \text{ cm/kyr}$  sedimentation rate and assuming insolation values as the paleoclimatic proxy. To maintain the actual start and stop times of the stratigraphic series (2.706 Ma to 5.329 Ma) the stratigraphic sample rate was set at  $2.0446 \text{ cm/kyr}$ . (F)  $2\pi$  multitaper power spectrum of E showing amplification of difference tones in the orbital eccentricity band and  $1/(54 \text{ kyr})$  obliquity frequency, and suppression of addition tones and the short  $1/(19 \text{ kyr})$  precession index. (G) Simulation of bioturbation with a simple 10-m smoothing window applied to the stratigraphic series in E. (H)  $2\pi$  multitaper power spectrum of (G) showing further amplification of orbital eccentricity frequencies and  $1/(54 \text{ kyr})$  obliquity frequency, and further reduction of addition tones. (I) Simulation of bioturbation with a simple 20-m smoothing window applied to the stratigraphic series in E. (J)  $2\pi$  multitaper power spectrum of I showing further amplification of orbital eccentricity frequencies and near full suppression of the precession index.

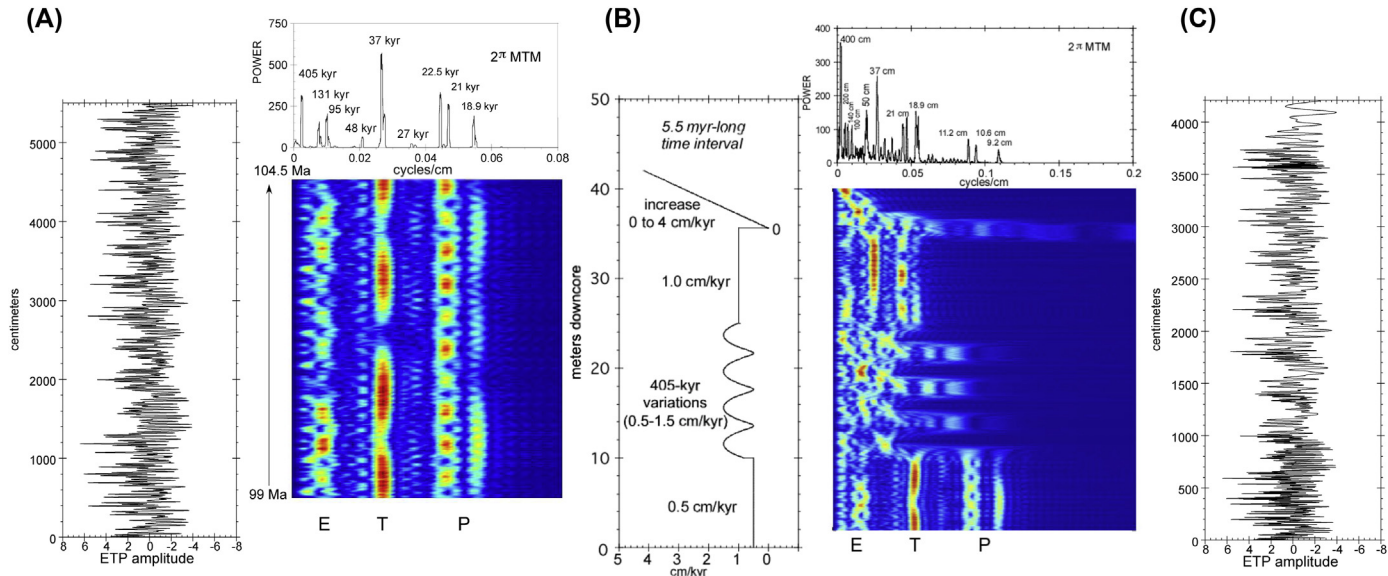
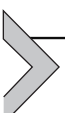


**Figure 12** A demonstration of variable accumulation rates and their effects on an astronomical forcing signal, represented as the synthetic combination ETP (defined in Section 3.1.1). (A) Left: ETP signal from 99 Ma to 104.5 Ma from the La2004 solution at <http://vo.imcce.fr/insola/earth/online/earth/earth.html>, converted to “stratigraphy” assuming a 1 cm/kyr sedimentation rate. Top:  $2\pi$  power spectrum; bottom: FFT spectrogram computed with a 250-cm window. (B) Variable sedimentation rates to be applied to the same ETP signal that is recorded in A. (C) Right: ETP signal converted to stratigraphy according to the sedimentation rates in B. Top:  $2\pi$  power spectrum; bottom: FFT spectrogram computed with a 250-cm window.

effects of a series of sedimentation rate variations on an astronomical signal. The example (Fig. 12B) considers a series of sedimentation rates starting with a constant rate of 0.5 cm/kyr, changing to a cyclic variation with a 405-kyr periodicity, followed by a constant 1 cm/kyr rate, a brief (one sample long) hiatus, and ending with an interval with a linear increase in rates from 0 to 4 cm/kyr. While the two stratigraphic intervals characterized by constant rates have an easily identifiable ETP signal, it is far more difficult to detect the ETP signal in the intervals with variable rates (Fig. 12C). This problem is ubiquitous in cyclostratigraphy — especially in the very long, multi-million year-long sequences that are being collected today — and is the main motivation for the practice of “tuning” discussed at length below (Section 3.3).



## 2. CYCLOSTRATIGRAPHY

Today sedimentologists and stratigraphers are sensitive to an unprecedented degree that astronomical forcing could be recorded in their sections. Researchers with a singular focus on cyclostratigraphy and reconstructing timescales (Section 4) are now collecting multi-million year-long cyclostratigraphic series that are correlated to all available biostratigraphy, magnetostratigraphy, chemostratigraphy and radioisotopic geochronology. Cyclostratigraphy from 0 to 55 Ma can theoretically be matched directly to the astronomical solution (Section 1.1.2), although modeling and testing will continue to be required to determine  $p_{\odot+c}$  for all geologic times (Section 1.1.4). Visual identification (Section 3.3.1) of the 405-kyr metronome (Section 3.2.1) has been especially provident for effective alignment of astronomical signals in Mesozoic and Paleozoic cyclostratigraphy (Section 4). Representative examples of well-known cyclostratigraphic sequences are highlighted below. Also notable is that the best cyclostratigraphic evidence almost exclusively comes from drill core data, which provides the required level of high-precision control on stratigraphic position.

### 2.1 Cenozoic

The cyclostratigraphy that has contributed the most to the Neogene time scale is from the Mediterranean sapropelic sequence, which has been analyzed for biostratigraphy, magnetostratigraphy and oxygen isotopes, and correlated with deep-sea drill core counterparts from the Atlantic and

Pacific oceans (Lourens et al., 2004; Hilgen et al., 2012). The astronomically forced benthic marine  $\delta^{18}\text{O}$  record for 0–5 Ma has also been correlated and “stacked” across 57 sections from the Atlantic, Pacific, Indian and Southern oceans (Lisiecki and Raymo, 2005), testimony to the strong global nature of the record.

Following on the Cenozoic  $\delta^{18}\text{O}$  curve compiled by Zachos et al. (2001, 2008), a benthic marine  $\delta^{18}\text{O}$  “Megaslice” over 0 to 35 Ma was recently stitched together from single ODP core records in series for study of the time evolution of phasing of recorded astronomical parameters (De Vleeschouwer et al., 2017a). This “Megaslice” (Fig. 13A) shows the characteristic Oi1 step at the Eocene-Oligocene boundary, interpreted as the glaciation of Antarctica, followed by strong astronomically forced cycling throughout the Oligocene, ending with a pronounced Mi1 spike at the Oligocene-Miocene boundary (Paleogene-Neogene boundary), a reversal during the mid-Miocene, followed by renewed cooling at Mi3, and in this record, stasis from 13 to 3 Ma, when major glaciations came to dominate the Northern Hemisphere. The astronomical cycles are very pronounced, and reasonably well-aligned by the current tuning, except at precession timescales (detail and power spectrum in Fig. 13A).

Gamma ray (GR) logs from boreholes in the continental Bohai Bay Basin (North China) have been assembled into a complete Paleogene sequence of syn-rift and post-rift sedimentation from 66 Ma to 23 Ma, with a continuous 43-Myr long record of astronomical forcing (Liu et al., 2017a). 405-kyr cycles were identified and used to reconstruct the sedimentation history of the basin, showing a dramatic drop (by a factor of 6) in sedimentation rate at 35.99 Ma just prior to Eocene-Oligocene boundary (and glaciation of Antarctica). Rifting events in the basin, indicated by increases in sedimentation rate, are newly calibrated by the 405-kyr-based timescale, and compared with the subduction of the neighboring Pacific Plate to the east, collision of the Indian and Eurasian plates to the south, and drying episodes in the Late Eocene of eastern Asia.

Elsewhere, Eocene cyclostratigraphy has been correlated to the astronomical solution with core-scanning XRF and carbon isotope data indicating 405-kyr cycles, with researchers chipping away at a longstanding mid-late Eocene cyclostratigraphic gap (Westerhold et al., 2012, 2014, 2015; Boulila et al., 2018). The timing of the Paleocene/Eocene boundary has been astronomically estimated, using interpreted precessional cycles, as 170 kyr (Röhl et al., 2007). In the Paleocene, cyclostratigraphy from ODP cores and outcrops (notably Zumaia, Spain) has also been used to

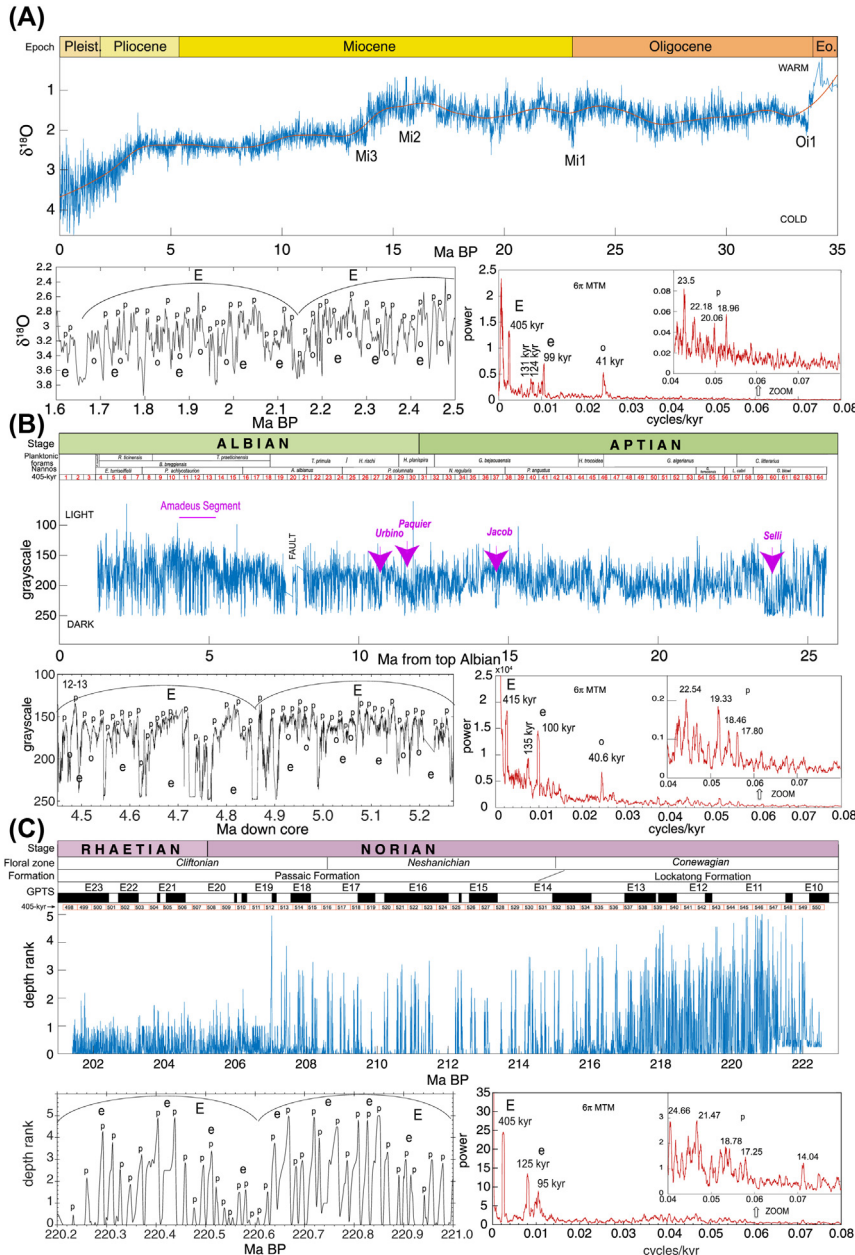


**Figure 13** Exceptional cyclostratigraphic sequences from the Cenozoic and Mesozoic eras. For each case, three panels are displayed: top: the tuned cyclostratigraphic proxy; bottom left: a detail; bottom right:  $6\pi$  multitaper power spectrum, with a vertical zoom of the precession index band. Precession index power is low in part

calibrate the age of the K/Pg boundary, which occurred during an orbital eccentricity minimum (Herbert, 1999), with research progressively adjusting the number of observed 405-kyr cycles through the epoch from 24 to 25 together with new radioisotope geochronology (65.28 Ma or 65.68 Ma, Westerhold et al., 2007, 2008; 65.95 Ma, Kuiper et al., 2008; 66 Ma, Hilgen et al., 2010; 66.043 ± 0.043 Ma, Renne et al., 2013; 66.022 ± 0.040 Ma, Dinarès-Thurell et al., 2014).

## 2.2 Mesozoic

Over the past decade there has been rapid progress in studies of Mesozoic cyclostratigraphy and astrochronology. A complete account of the significant developments is provided in Huang (this volume), with highlights summarized below.

### 2.2.1 Cretaceous

The K/Pb boundary calibrated from cyclostratigraphy from below (i.e., from the Maastrichtian) is consistent with the Paleocene calibration from Zumaia and neighboring outcrops (65.56 Ma or 65.97 Ma; Batenburg et al., 2012, 2014; 66 Ma, Dinarès-Thurell et al., 2013) and from ODP Site 762 (66 ± 0.07 Ma, Husson et al., 2011). The estimate of approximately 300 kyr from the K/Pb boundary to the base of C29r (e.g., Table 1 in

due to uncorrected high frequency sedimentation rate variations. Labels: E = 405 kyr long orbital eccentricity, e = ~100 kyr short orbital eccentricity, o = obliquity, and p = precession index cycles. (A) 35 Myr long composite benthic marine  $\delta^{18}\text{O}$  “Megasplice” from late Eocene-Pleistocene ODP drill core records consisting of 12171 measurements with an average  $\Delta t = 3$  kyr (De Vleeschouwer et al., 2017a). Epochs are shown at the top; Oi1, Mi1, Mi2 and Mi3 indicate glaciation events. Note: the  $\delta^{18}\text{O}$  scale (y-axis) points down. This “Megasplice” is publicly available at <https://doi.pangaea.de/10.1594/PANGAEA.869815>. (B) 23.936 Myr long grayscale scan with a 0.8 mm resolution of the 77-m long Aptian-Albian abyssal Scisti a Fucoidi in the Piobbico Core, central Italy, tuned to the indicated 405-kyr cycles, resolving an average  $\Delta t = 0.24$  kyr (Grippo et al., 2004; Huang et al., 2010a, 2010b, 2010c). The “Amadeus Segment” is the 8-m segment analyzed by Herbert et al. (1986) and Park and Herbert (1987). The numbers in the rectangles represent 405-kyr cycle number from top of Cenomanian. Data are courtesy of A. Grippo. (C) 21.12 Myr long depth rank series of a 3447-m long composite section of drill cores from the Norian-Rhaetian Newark Basin, eastern USA with 4040 points, tuned to the indicated 405-kyr “McLaughlin” cycles, for an average  $\Delta t = 5$  kyr (Kent et al., 2017, 2018). The numbers in the rectangles represent 405-kyr cycle number from the present. This dataset is publicly available at <https://www.ledo.columbia.edu/~polsen/nbcn/data.html>.

**Table 1** Planetary Secular Frequencies from Table 3 in [Laskar et al. \(2004\)](#). The Subscripts 1–6 Represent Each Planet (1 = Mercury; 2 = Venus; ..., 6 = Saturn)

| Secular frequencies | Arcseconds/yr | yr      |
|---------------------|---------------|---------|
| $g_2$               | 7.452         | 173913  |
| $g_3$               | 17.368        | 74620   |
| $g_4$               | 17.916        | 72338   |
| $g_5$               | 4.257452      | 304307  |
| $s_2$               | −7.050        | −183830 |
| $s_3$               | −18.850       | −68753  |
| $s_4$               | −17.755       | −72911  |
| $s_6$               | −26.347855    | −49188  |

[Hennebert, 2014](#)) inspired an upward cyclostratigraphic extrapolation from the base of C29r to identify the K-Pb boundary in the continental Songliao Basin of China ([Wu et al., 2014](#)), which exhibits cyclostratigraphy through much of its depositional history through the entire Cretaceous Period ([Wang et al., 2013](#)). A well-known Tethyan cyclostratigraphic section from Bottaccione Gorge, Italy was evaluated, yielding a Santonian duration of 2.94 Myr, and a Coniacian duration of 3.46 Myr ([Sprovieri et al., 2013](#)). In the Western Interior Seaway, USA cyclostratigraphy integrated into the regional chronostratigraphy to provide an astronomical timescale for the entire Niobrara Formation with a Santonian duration of  $2.3 \pm 0.82$  Myr (shorter than the Tethyan scale) and a Coniacian duration of  $3.26 \pm 0.82$  Myr ([Sageman et al., 2014](#)). This was followed by a transformational analysis of the long-term modulations of the eccentricity ( $g_4 - g_3$ ) and obliquity ( $s_4 - s_3$ ) in the Niobrara Formation, which detected evidence for an orbital resonance transition between Earth and Mars that had been predicted by the La2004 solution from 83 Ma to 90 Ma ([Ma et al., 2017](#)) (see [Section 1.1.3](#)).

In the Tethyan abyssal realm, in central Italy (not far from Bottaccione) a core was drilled through the entire Aptian-Albian section, the “Piobbico Core” ([Fischer et al., 1991](#)). Among the many innovative studies that have been carried out on this core, a high-resolution grayscale scan of digitized core photographs was analyzed ([Fig. 13B; Grippo et al., 2004; Huang et al., 2010a](#)). The recognition of 405-kyr cycles through the entire section provides a 24 Myr long astrochronology, continuous sampling of the major lower Cretaceous black shales (e.g., the Selli event) and recovery of an

explicit record of all three astronomical parameters (detail and power spectrum in Fig. 13B). The grayscale scan (lightness L $\star$ ) of a drill core through the Volgian Stage (the lowermost Cretaceous to upper Jurassic) in the Norwegian Sea records 13.3 Myr of astronomical cycling, with the potential to solve the long-standing problem of correlating the Volgian to the international chronostratigraphic units (Tithonian and Berriasian stages; Huang et al., 2010b).

### 2.2.2 Jurassic

The upper Jurassic source rock, the Kimmeridge Clay (Dorset, England) was drilled in 1996 and 1997, providing excellent drill cores for study of its organic shales and cyclostratigraphy (Morgans-Bell et al., 2001). An initial cyclostratigraphic study (Weedon et al., 2004) was revised into a 405-kyr cycle calibration using total organic carbon (TOC) and Formation Micro Scanner (FMS) data (Huang et al., 2010c), indicating a 6.74 Myr long duration for the formation. Studies of shorter cyclostratigraphic intervals have identified 405-kyr cycles in a number of European Aalenian-Oxfordian sections (see Appendix G). The Toarcian cyclostratigraphic sequence of the Sancerre Core (France) has been tuned to 405-kyr cycles for a total duration of 8.3 Myr (Boulila et al., 2014), including the renowned Toarcian Oceanic Anoxic Event, for which the astrochronological interpretation remains controversial and unsettled (reviewed in Boulila et al., 2017). Hand-held XRF measurements of the Pliensbachian Mochras Core (Wales) have revealed pronounced astronomical cycles, with strong 405-kyr cycles indicating a duration of 8.7 Myr (Ruhl et al., 2016). Currently in the lower Jurassic only the Sinemurian is missing complete cyclostratigraphic coverage; the Hettangian-Lower Sinemurian outcrops from St. Audrie's Bay/Quantoxhead (Somerset, UK) provide a 2.7 Myr long astronomical record at the start of the Jurassic Period (Hüsing et al., 2014).

### 2.2.3 Triassic

The Newark Series is a thick continental sedimentary sequence from a tropical rift system in eastern North America (Olsen, 1997, 2010). Within the Newark Basin a nearly 7 km-thick cyclic lacustrine sequence from 233 Ma to 199 Ma archives the early evolution of the dinosaurs, the rifting of Pangea, and an astronomically forced paleoclimate system (Olsen and Kent, 1996). Depositional cycles are comprised of organic-rich, laminated

shales (deep lake) yielding to subaerial-exposed, desiccated mudstones (lake margin) in repeating sequences, documented by facies analysis of drill cores, and compiled as a “depth rank” series (Fig. 13C). This depth rank series shows the hallmarks of precession-eccentricity cycling, with 20-kyr “Van Houten cycles” (‘p’) bundled into  $\sim$ 100-kyr “short modulating cycles” (‘e’) and 405-kyr “McLaughlin cycles” (‘E’) (Kent et al., 1995; Olsen and Kent, 1996; Kent et al., 2017). The latter recently were shown to be precisely phased with the 405-kyr term of the La2004 solution (Table 6 in Laskar et al., 2004; see Appendix F) (Kent et al., 2018; Hinnov, 2018). Coeval to the Newark Series – but a world away – is a remarkable marine bedded chert sequence (Inuyama, Japan), which spans 70 Myr from Lower Triassic to Lower Jurassic (Ikeda et al., 2010; Ikeda and Tada, 2013, 2014; Ikeda et al., 2017) (see Fig. 5 in Huang, 2018). This sequence, with its extremely slow accumulation rate, has greatly magnified the recorded orbital eccentricity, and modulations with a 1.6 to 1.8 Myr periodicity that may be related to a similar, 1.75 Myr periodicity detected in the Newark depth rank series (Ikeda and Tada, 2013; Olsen and Kent, 1999). Both records differ from the low-frequency orbital eccentricity solutions computed for this time period (i.e., La2004, La2010a–d). The extraordinarily long span of the Inuyama sequence also reveals even longer term,  $\sim$ 8 Myr cycling, which has yet to be assigned an attribution. Finally, Lower Triassic cyclostratigraphy in South China (Li et al., 2016), has recently been correlated with the German Basin (Li et al., 2018a), as well as to the Japanese Inuyama sequence (Huang, 2018).

### 2.3 Paleozoic

As would be expected, cyclostratigraphy of the Paleozoic Era is relatively unexplored. Since there are no astronomical solutions to provide an accurate time framework, Paleozoic cyclostratigraphy is limited to empirical evidence. An active research initiative is underway to improve knowledge of this evidence (International Geological Correlation Programme 652, [http://www.geolsed.ulg.ac.be/IGCP\\_652/](http://www.geolsed.ulg.ac.be/IGCP_652/)). The recent confirmation that the strong 405-kyr orbital eccentricity cycle in the La2004 solution is precisely phased with the radioisotopically calibrated Newark Series at 215 Ma (Section 2.2.3) raises expectation that as with Cenozoic and Mesozoic, 405-kyr cycles also dominated Paleozoic cyclostratigraphy, and this is affirmed below.

### 2.3.1 Permian

Intense interest in the end-Permian biotic extinction and its causes has generated high-precision geochronological data (Burgess et al., 2014; Burgess and Bowring, 2015; Burgess et al., 2017; Ramezani and Bowring, 2018) and analysis of late Permian Chinese cyclostratigraphy exhibiting strong 405-kyr cycles (Wu et al., 2013). In the lower North American Ochoan (Late Permian), the extraordinary evaporitic Castile Formation, USA with more than 200,000 carbonate-anhydrite varves provides a rare and fascinating observational window into paleoclimatic variations from annual to orbital eccentricity scale (Anderson, 1982; Anderson, 2011). The sequence of basinal chert-mudstone alternations of the Guadalupian (Middle Permian) Gufeng Formation (Lower Yangze, South China) was tested with a three-step (obliquity/long-precession/obliquity) tuning process (similar to the procedure of Imbrie et al., 1984) sharpen power in the obliquity and precession index bands (Yao et al., 2015). To the west, the coeval, highly cyclic limestone-rich Maokou Formation (Upper Yangze, South China) was measured for magnetic susceptibility and anhysteretic remanent magnetism, revealing astronomical forcing. Tuning to strong 405-kyr cycles aligns a strong 32 kyr cycle interpreted as obliquity (shortened from present-day, see Section 1.2.4), and evidence for orbital resonance transitions (Section 1.1.3) (Fang et al., 2015, 2017).

### 2.3.2 Carboniferous

The Carboniferous Earth was an icehouse with large and dynamic continental ice sheets enveloping southern Gondwana, and large sea level oscillations repeatedly flooding the continental margins. One of the great legacies of the sea level transgression-regressions are the well-known Carboniferous cyclothsems, recognized worldwide, e.g., the Midcontinent Sea (Algeo and Heckel, 2008) and Russian Platform of Euramerica (Eros et al., 2012), eastern Panthalassic Gondwana margin (Grader et al., 2008), South China Block (Feng et al., 1998), and Australia (Fielding et al., 2008). Despite the high repute of the cyclothsems, until recently, their origins have not been ascribed to Milankovitch forcing. High-precision radioisotope geochronology was the first line of evidence indicating that cyclothsems occurred at 405-kyr intervals (Davydov et al., 2010; Schmitz and Davydov, 2012). The cyclic periplatform slope deposits of the Dian-Qian-Gui-Xiang Platform in South China were recently discovered to contain a 14.6 Myr

long record (36 405-kyr cycles) of astronomical forcing (Fang et al., 2018). Another ongoing investigation at Naqing (South China) has documented a 34 Myr-long record of astronomical cycles that is so long that a shift toward lower-period obliquity cycles can be detected, from 30.5 kyr to 31.5 kyr (Wu et al., 2018a, 2018b). Finally, new analysis of Late Bashkirian cyclostratigraphy in the Copacabana Formation of Bolivia (Carvajal et al., 2018) has enabled an estimate of  $k (= p_{\odot+c})$  and Carboniferous LOD (Section 1.2.4) (Ma et al., 2018).

### 2.3.3 Devonian

The Devonian Period was predominantly a greenhouse, except for the latest Devonian (Famennian), during which climatic instabilities swinging between intervals of glaciation and oceanic anoxia occurred repeatedly in advance of the Carboniferous icehouse (Isaacson et al., 2008; McGhee, 2013). The astronomical forcing of the Famennian was investigated comprehensively by Pas et al. (2018), who analyzed drill core from the deep shelf deposits of the Illinois Basin, USA, finding a 13.5 Myr-long record of strong 405-kyr cycling, accompanied by  $\sim 100$  kyr and 34 kyr cycles, ascribed to forcing from the orbital eccentricity and obliquity, with stratigraphic effects presumably suppressing what had to have included strong precession index forcing (see Section 1.4.1). Following on modeling by Le Hir et al. (2011) demonstrating that combined continental drifting and land plant expansion caused the significant CO<sub>2</sub> drawdown during the Devonian, De Vleeschouwer et al. (2014) used the Hadley Centre GCM to simulate Devonian climate conditions for different combinations of the astronomical parameters. The results indicate that for the Frasnian greenhouse, confluent obliquity and orbital eccentricity maxima produce the highest mean annual temperatures (27 °C) and confluent minima produce the lowest (19.5 °C) temperatures (This is consistent with Mesozoic and Cenozoic responses to these parameter configurations; e.g., Hinnov, 2018.). This pattern was explored further to explain the timing of the Late Devonian extinctions during the Frasnian-Famennian transition (De Vleeschouwer et al., 2017b). Cyclostratigraphy of outer ramp carbonate facies of the Belgian Givetian was analyzed by De Vleeschouwer et al. (2015) using a magnetic susceptibility proxy, documenting 405-kyr and  $\sim 100$  kyr cycles (orbital eccentricity), 33 kyr cycles (obliquity) and 18 kyr cycles (precession index), and an estimated duration (based on the 405-kyr cycles) of  $4.35 \pm 0.45$  Myr for the Givetian Stage. The 33 kyr periodicity assigned to the

obliquity suggests a slower LOD than for the Carboniferous, for which a substantially faster 30.5 kyr to 31.5 kyr obliquity periodicity has been estimated (Section 2.3.2). Moroccan cyclostratigraphy of the Eifelian Stage based on low-resolution magnetic susceptibility measurements suggests a duration of 6.28 Myr for the stage (Ellwood et al., 2015). Astronomical forcing of Early Devonian cyclostratigraphy of the Czech Republic was identified with ASM modeling (Section 3.5.2) assuming the modeled Devonian (400 Ma) astronomical parameter periodicities of Berger et al. (1992) (orbital eccentricity: 400 kyr, 131 kyr, 123 kyr, 100 kyr and 95 kyr; obliquity: 38.7 kyr and 31.6 kyr; precession index: 19.7 kyr and 16.7 kyr) (Da Silva et al., 2016; power spectra showing obliquity and precession index bands appear in their Appendix.)

#### 2.3.4 Silurian

While there is a long-standing interest in Silurian cyclostratigraphy, practically no studies have yet attempted to identify whether astronomical forcing played a role. In their study of the Lochovian GSSP, Crick et al. (2001) measured the magnetic susceptibility across the Silurian-Devonian boundary in the Czech Republic and Morocco, and considered the possibility that the sedimentary cyclicity common to both localities had been forced by obliquity or orbital eccentricity. The evidence for global sea level cycles throughout the Silurian at the Myr-scale (Calner, 2008) should be sampled in greater stratigraphic detail – ideally by coring (e.g., by the Swedish Deep Drilling Program; Lorenz, 2010) – in order to resolve astronomical forcing timescales. Short shallow marine sections of the Estonian Wenlockian have been described as having shallowing-upward cycles (Nestor et al., 2001); recently, examination of Upper Homerian (Sheinwoodian) cyclostratigraphy of Lithuania suggests astronomical forcing, with nested “fourth” and “fifth” order cycles, plus an unnamed higher order of cycling (Radzevičius et al., 2017).

#### 2.3.5 Ordovician

A growing number of Milankovitch-forced successions have been reported from the Late Ordovician, presumed to involve a strong glacioeustatic component during the Katian. These include the Juniata Formation in the eastern Appalachians indicating an obliquity periodicity of 30 kyr (Hinnov and Diecchio, 2015), glacial deposits in northern Africa (Loi et al., 2010), the Mallowa Salt in northwestern Australia with an estimated obliquity periodicity of  $31.3 \pm 3$  kyr (Williams, 1991), and the Kope Formation of

eastern-central North America (Ellwood et al., 2013). The Vauréal, Ellis Bay and Bepscie formations of Anticosti Island, eastern Canada (Desrochers et al., 2010; Elrick et al., 2013) have recently been sampled at high resolution, which has the potential to reveal astronomical variations (Sinnesael et al., 2017a, 2017b). In the Sandbian, the lower slope deposits of the Pingliang Formation (Guanzhuang, China; Fang et al., 2015) and the Arnestad Formation of southern Norway (Svensen et al., 2015) both show strong organized sedimentary cyclicity indicative of orbital eccentricity, obliquity, and precession index forcing, the obliquity with shorter periodicities (Pingliang: 30.6 kyr; Arnestad: 30.3 kyr). The Llanvirn (Middle Ordovician) Krivaya Luka section of Siberia has strong sedimentary cycles with magnetic susceptibility variations suggestive of astronomical forcing (Rodionov et al., 2003). The Darwillian (Middle Ordovician) of France has revealed promising patterns indicative of astronomical forcing, but lacking in sufficient age constraints (Dabard et al., 2015; Sinnesael et al., 2017a, 2017b).

In the Lower Ordovician, periodic sedimentation has been found in the Ibexian–Whiterockian marginal marine shelf deposits of the Wah and Juab formations, Utah, with hierarchical thickness bundling meter-scale cycles suggestive of astronomical forcing (Gong and Droser, 2001). The Tremadocian–Arenigian thick Dumugol Formation (Korea) is comprised of a succession of meter-scale basinal, ramp and subtidal cycles, each thought to represent a 96 kyr periodicity (Kim and Lee, 1998). The 115 shallow-marine carbonate cycles of the (mostly Arenigian) El Paso Group in the Franklin Mountains, Texas have cycle thicknesses bundling patterns with unfamiliar ratios (14:1, 9:1, 6.25:1 and 4.17:1) and supposed not due to astronomical forcing (Goldhammer et al., 1993). This conclusion was based on subjective facies analysis at the outcrop; for objective measurements of magnetic susceptibility or other geophysical/geochemical proxy, there might be a different result (Kodama and Hinnov, 2015).

### **2.3.6 Cambrian**

The Cambrian is well known for its worldwide thick sequences of cyclic shallow marine carbonate platforms (and their continuation into the early Ordovician, see Section 2.3.5) (Derby et al., 2012). Most of the analysis of these cyclic peritidal sequences measured cycle thicknesses as a basis for assessing whether astronomically forced sea level oscillations could explain their stacking patterns, e.g., Olseger and Read (1991). Similarly, Bazykin and Hinnov (2002) analyzed thickness bundling frequencies in the Cambro-Ordovician of Kazakhstan and compared them with those of

astronomical models. An interesting development was the “gamma method” ([Section 3.5.5](#)) to estimate sedimentation rates of cyclic sub-facies of middle Cambrian carbonate platform cycles (e.g., subtidal, intertidal and supratidal) by [Bond et al. \(1991\)](#). The gamma age model of the middle Cambrian Trippe Limestone sequence that they studied realigned power into the frequencies that would be expected for astronomical forcing. The gamma method was later abandoned due to its predisposition to assign more time to thicker sub-facies, when for shallow marine carbonates, subtidal units tend to accumulate faster than intertidal and supratidal units (due to accommodation space).

## 2.4 Precambrian

While representing the lion’s share of Earth history, the Precambrian system remains the least explored of geology, especially in terms of cyclostratigraphy. This state of affairs is rapidly changing, however, with the advent of high-precision geochronology and chemostratigraphy providing the chronostratigraphic framework in the absence of biostratigraphy. Now, it is evident that cyclostratigraphy can also play a role. However, this depends on whether the Solar System operated similarly, e.g., is the Earth’s orbital eccentricity still recognizable? How different was the Earth’s rotation? There is pre-existing data and modeling to help anticipate the answers, which are that the orbital eccentricity variations were similar, with 405-kyr,  $\sim 100$  kyr cycles, and that the obliquity and precession index cycles were shorter, as indicated by evidence for shorter LOD ([Fig. 5](#)). Below is a selection of notable studies.

### 2.4.1 Neoproterozoic

At the start of the Ediacaran Period when the Earth exited its “snowball” phase, in succession it experienced a series of three very pronounced negative marine carbon isotope excursions (CIEs), the emergence of the Ediacaran biota, traces and burrows, and at the end of the period, the occurrence of shelly faunas. The Shuram Excursion (SE), the last and largest of the CIEs immediately preceded the explosion of life ([Grotzinger et al., 2011](#)). The timescale of the SE is unknown, with an onset date sometime between 560 Ma to 580 Ma. In some localities, it occurs within a thick sequence of cyclic deposits, hypothesized as astronomically forced. In the Johnnie Formation (Death Valley, USA) the SE is estimated to have lasted 8.2 Myr, with an 818 kyr long deep phase near the start of the event ([Minguez et al., 2015](#)); in the Doushantuo Formation (Donghahe, South China)

cyclostratigraphy indicates that the SE lasted an estimated 9.1 Myr (Gong et al., 2017).

The Cryogenian Period, with its repeated snowball Earth glaciations, is characterized by extended interglacial deposits separating the glacial deposits associated with the snowball events. Between the Sturtian and Marinoan glaciations, cyclostratigraphy of a 292 m-long ZK1909 drill core of the Datangpo Formation (South China) reveals a remarkable series of astronomical cycles lasting 9.8 Myr from 660 Ma to 650.2 Ma (Bao et al., 2018), with 405-kyr tuned obliquity and precession index periodicities consistent with a model based on  $k = p_{\odot+c} = 64.6$  arcseconds/year (650 Ma; Williams, 2000).

#### 2.4.2 Mesoproterozoic

The cyclostratigraphy of the 1.4 Ga Xiamaling Formation (Xiahuayuan, North China) consists of alternating basinal iron oxide-rich and iron oxide-poor mudstones and black shales with cm to m scale bedding, interpreted as astronomically forced cycles with obliquity periodicities of 21 kyr, 27 kyr and 30 kyr, and precession index periodicities of 12 kyr, 14 kyr and 16 kyr (Zhang et al., 2015). A short segment of Cu/Al data, a productivity/redox proxy, representing approximately 600 kyr, was further analyzed to optimize estimates of  $k (= p_{\odot+c})$ ,  $g_2$ ,  $g_3$ ,  $g_4$  and  $g_5$ , (Table 2 in Meyers and Malinverno, 2018), which supports the Zhang et al. interpretation, with an estimated  $k = 85.79$  arcsec/year and precession index periodicities of 12.5 kyr to 14.4 kyr. Further down in the Chinese Mesoproterozoic section is the 1.6 Ga Wumishan Formation (Tianjin, North China), a 3-km thick carbonate platform with a stack of 626 m-scale peritidal cycles, each consisting of lagoonal to supratidal flat subfacies (Mei et al., 2001). Observations of widespread 4:1 bundling of cycle thicknesses, and local 1:5 to 1:8 bundling, led to speculations of Milankovitch forcing (Mei and Tucker, 2013). Studies are ongoing with magnetic susceptibility measurements to completely document the astronomically forced cyclicity of this extraordinary sequence, which is so long that it spans an aragonite/calcite sea transition with a change from cement-dominated to micrite-dominated stromatolites, and records processes at the Wilson cycle scale (Hinnov et al., 2015).

#### 2.4.3 Paleoproterozoic

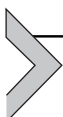
The Lower Proterozoic (1.89 Ga) Rocknest Formation (Northwest Territories, Canada) consists of a stack of up to 160 m-scale peritidal carbonate

platform cycles suggestive of, but not yet assessed for astronomically forced sea levels ([Grotzinger, 1986](#)). The documentation of these cycles at the sub-facies level should make it possible to reconstruct a “depth-rank” facies (analogous to that of the Newark Series) for spectral analysis, and ultimately, perhaps, a new field campaign to reinvestigate the formation with objective technologies (e.g., magnetic susceptibility).

Most intriguing of all are the banded iron formations (BIFs), which count among Earth’s oldest sedimentary deposits, and coming into prominence at the start of the Proterozoic (e.g., Fig. 2 in [Klein, 2005](#)). The most intensely studied of BIFs in terms of cyclic deposition is the 2.5 Ga Dales Gorge Member of the Brockman Iron Formation (Hamersley Basin, Australia), the first from [Trendall \(1965, 1966\)](#). The origins of the pervasive and multiscale cycling of iron oxide and silica remain enigmatic, stymied by lack of adequate geochronology, and by the lack of proxies that can be sampled adequately through sections to resolve the multiple scales. Gray-scale scanning presently suffices as a crude proxy for characterizing iron-rich vs. silica-rich lithologies, and in the upper part of the Dales Gorge Member reveals affinities in the cycling patterns that would be expected for astronomical forcing at that time. Namely, precession index cycles would be expected to have a 11.3 kyr to 12.7 kyr periodicity ([Berger and Loutre, 1994](#)), and assuming that orbital eccentricity cycles maintained a  $\sim$  100 kyr periodicity at the time, a  $\sim$  10:1 bundling of cycles would be expected, as observed in the 16-cm thick “mesobands” in the upper part of the Dales Gorge (Fig. 2 in [Rodrigues et al., 2018](#)).

#### 2.4.4 Archean

The oldest cyclostratigraphic record described thus far is a sequence of shallowing-upward carbonate cycles from the Archean (2.65 Ga) Cheshire Formation (Zimbabwe) ([Hofmann et al., 2004](#)). A 10:1 bundling of the cycle thicknesses is consistent with precession index forcing with an 11.6 kyr mean periodicity, bundled into  $\sim$  100 kyr orbital eccentricity cycles.



### 3. ASTROCHRONOLOGY

In the 19th century, without the knowledge of radioisotopes, geologists turned to cyclic sedimentary deposits for ways to determine geologic time. This included the renowned Charles Lyell who, influenced by the astronomical theory of ice ages by Adhémar and Croll, calibrated glacial deposits from the Last Ice Age (now known to be 20 Ka) to the most recent

maximum orbital eccentricity at 850 Ka, for which the modern solution indicates 972 Ma (Fig. 2A) (Hilgen, 2010). Geologists continued to flirt with the use of an astronomical-forced paleoclimate record as a means for timescale calibration, until radioactivity was discovered in 1895, leading to the radioisotope geochronology revolution. Nonetheless, the later characterization of astronomical forcing as “the insolation canon” by Milankovitch (1941) and the idea that planetary orbital influences on Earth’s surface processes could be highly deterministic was never fully struck from geological doctrine. The seminal report on Pleistocene evidence for astronomical forcing by Hays et al. (1976) was the shot in the arm needed to motivate geologists to initiate a wide-ranging search for astronomical signals in stratigraphy (Fischer, 1986; Fischer et al., 1988), leading to the founding of “cyclostratigraphy” and declarations such as: “Milankovitch cycles are like varves and are proper time units, at least within the accuracy of geological measurements.” (p. 197, Schwarzacher, 1993). The following sections review the profusion of methods that have been devised to link cyclostratigraphic proxy series to the astronomical parameters in the attempt to define timescales.

### 3.1 Astronomical Targets

#### 3.1.1 Time Domain

For explaining the great Pleistocene ice ages, summer insolation at 65° North was marked as the best indicator for ice sheet expansion when insolation was too low to allow ice to melt during the summers (Milankovitch, 1941, and other earlier works). Thus, deepest insolation minima from 0–600 Ka (Fig. 14A) were matched to the Würm I, II, and III, Riss I and II, Mindel I and II and Günz I and II European ice ages (review in Loutre, 2003). This time domain approach has persisted ever since in countless research publications. Among these the Late Neogene astronomical time scale was constructed using the same 65° N summer insolation, matching its maxima to the sedimentary record of Mediterranean sapropels (+3 kyr shift, required by radiocarbon-dated Holocene Sapropel S1 for 0 to 2.7 Ma) (Hilgen et al., 1993; Lourens et al., 2004). Astronomically forced glacial models (Fig. 14B) attempting to replicate the strong sawtooth variations and time delays in Pleistocene paleoclimate records (e.g., Imbrie and Imbrie, 1980) have also been used as tuning targets, e.g., the marine oxygen isotope stack of Lisiecki and Raymo (2005). As more data have been collected, it has become evident that simple insolation models do not fit data very well, especially the amplitudes of the variations (notably the

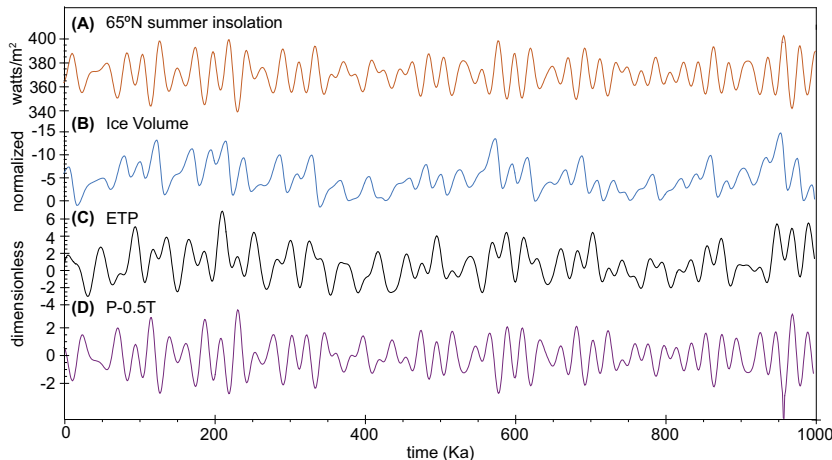


**Figure 14** Time-domain astronomical targets, all sampled with  $\Delta t = 1$  kyr from 0 to 1 Ma, all using the La2004 solution in *Analyseries 2.0.8* (Paillard et al., 1996). (A) Classic summer half-year insolation at  $65^\circ$  North. (B) Glaciation model according to Imbrie and Imbrie (1980), calculated in *Analyseries 2.0.8* (Basic Series menu) with the default settings. (C) Sum of standardized orbital eccentricity, obliquity and precession index, or ETP. (D) Standardized precession index (P) minus 0.5 of the standardized obliquity (T) (similar to mid-latitude summer insolation).

high amplitude orbital eccentricity signals that are not predicted by insolation). This has led to simplified astronomical models, such as the sum of standardized orbital eccentricity, obliquity, and precession index, known as ETP (or EOP) (Fig. 14C), devised by Imbrie et al. (1984). Another useful target is P-0.5T (Fig. 14D), developed for ease in testing different TD and ED models (e.g., Lourens et al., 1996; Lourens et al., 2001, Section 1.2.4).

### 3.1.2 Frequency Domain

Astronomical targets have increasingly moved from the time domain, where incremental manipulation of cyclostratigraphic data alters both frequencies and phasing of the cycling, and heightens the circularity problem in the practice of tuning, to the frequency domain. Since cycle phasing has important information, e.g., the phasing of the precession index can indicate season of forcing (Fig. 8). Therefore, one goal of tuning should be to preserve phasing within the data as much as possible. Minimal tuning (e.g., tuning to 405 kyr cycles only) is one way to achieve this (see Section 3.3.2 below). Another way is by searching for a sedimentation rate that maximizes power in the astronomical frequency bands. This is the approach taken by the

objective techniques offered by the average spectral misfit (ASM) and correlation coefficient (COCO) methods (see [Section 3.3.5](#) below). Finally, evolutionary spectrograms reveal shifting and drifting of frequencies, as shown in the synthetic example of [Fig. 12](#), and can be used to correct sedimentation rates by tracking a single spectral component that changes frequency through the spectrogram (e.g., [Preto et al., 2001; Yao et al., 2015](#)).

## 3.2 Astronomical Metronomes

### 3.2.1 Venus and Jupiter Longitude of Perihelia and Earth's Orbital Eccentricity $g_2 - g_5$

The most prominent of the Earth's orbital eccentricity terms is  $g_2 - g_5 = 3.199279''/\text{year}$  which completes a cycle in 405,091 years, determined by a recurrent alignment of the perihelia of Venus and Jupiter ([Fig. 2A and B](#); [Tables 1, 2](#)). The cycle is very stable due to the large mass of Jupiter; over a 250 Myr long solution,  $g_2$  indicates a variability of 13.4%, but  $g_5$  has a vanishingly small variability of only 0.0007% ([Table 3](#) and [Fig. 9](#) of [Laskar et al., 2004](#)). Thus, it is an excellent candidate for use as a high-precision “metronome”. It is readily observed in a majority of cyclostratigraphy, which is marked by enhanced orbital eccentricity cycles ([Section 1.4.1](#); [Fig. 11](#)). The phase of  $g_2 - g_5$  of the La2004 solution was recently verified by high-precision radioisotopic dating of the 200 Ma to 215 Ma continental Newark Series ([Fig. 13G–I](#); [Kent et al., 2018](#)). The definition of the La2004  $g_2 - g_5$  metronome is given in [Fig. 15](#), for which the first maximum in past time occurs at 192.125 Ka. It should be noted that the recent work on the Newark Series by [Kent et al. \(2017, 2018\)](#) assumed the less accurate maximum of 216 Ka based on the full orbital

**Table 2** Main Terms Used to Determine Earth's Orbital Eccentricity, Obliquity and Climatic Precession (Precession Index) Periodicities According to [Laskar et al. \(2004\)](#). The  $g_i$  and  $s_i$  are the Planetary Secular Frequencies; Subscripts 1–6 Represent Each Planet (1 = Mercury; 2 = Venus; ..., 6 = Saturn) and  $k$  is Earth's Precession Constant. For Present-day Earth,  $k = 50.475838$  Arcseconds/year ([Laskar et al., 2004](#))

|       | Orbital eccentricity | Obliquity |           | Climatic precession |
|-------|----------------------|-----------|-----------|---------------------|
| E     | $g_2 - g_5$          | $o_1$     | $k + s_6$ | $p_1$               |
| $e_1$ | $g_3 - g_2$          | $o_2$     | $k + s_3$ | $p_2$               |
| $e_2$ | $g_4 - g_2$          | $o_3$     | $k + s_4$ | $p_3$               |
| $e_3$ | $g_3 - g_5$          | $o_4$     | $k + s_2$ | $p_4$               |
| $e_4$ | $g_4 - g_5$          |           |           |                     |

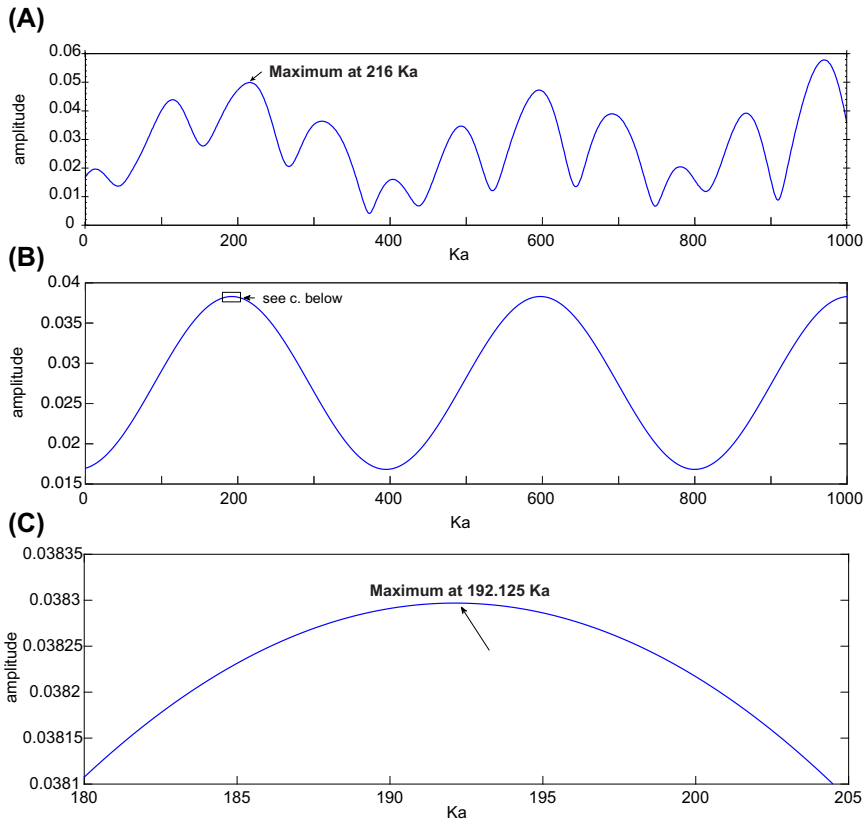


**Figure 15** The  $g_2 - g_5$  405-kyr metronome. (A) La2004 orbital eccentricity variation ([Laskar et al., 2004](#)) with apparent maximum at 216 Ka. (B)  $s_3 - s_6$  over the same interval based on Table 6 in [Laskar et al. \(2004\)](#). (C) The first  $s_3 - s_6$  405 kyr cycle indicates a maximum at 192.125 Ka (see [Appendix F](#) for MATLAB script).

eccentricity solution ([Fig. 15A](#)) for their metronome formula: the age of  $k$ th 405-kyr cycle maximum =  $0.216 + (k-1) \times 0.405$  Ma ([Eq. 1 in Kent et al., 2017](#)), or a difference of 23875 years. For the Arabian Orbital Time Scale, the age of the  $M^{\text{th}}$  405 kyr Stratigraphic base =  $0.371 + (M-1) \times 0.405$  Ma ([Al Husseini, 2015](#)), which also differs slightly from the La2004 definition of  $192.125$  Ka +  $405/2$  kyr =  $394.625$  Ka, or a difference of 23625 years.

### 3.2.2 Earth and Saturn Precession of Nodes and Earth's Orbital Inclination $s_3 - s_6$

The Earth's orbital inclination plays a major role in the modulations of the obliquity variation. One of these modulations involves Saturn's precession of

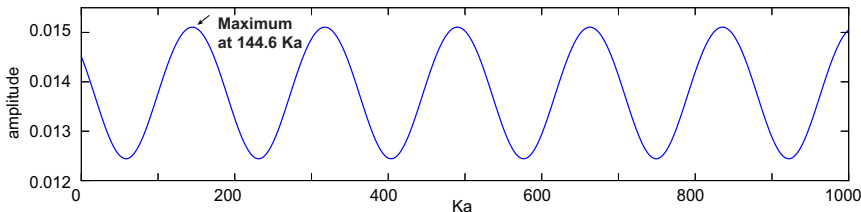


**Figure 16** The  $s_3 - s_6$  173-kyr metronome, computed using values from Table 5 and Eq. (26) in Laskar et al. (2004) (see Appendix F for MATLAB script).

nodes and its interaction with those of the Earth,  $s_3 - s_6$ ; it has a periodicity of 173 kyr (Fig. 2D). As with  $g_2 - g_5$ , the  $s_3 - s_6$  is unusually stable because of the large mass of Saturn. Thus, it can be used as a metronome in sequences characterized by dominant obliquity forcing and low precession index contributions (i.e., low or no  $g_2 - g_5$ ). The definition of the La2004  $s_3 - s_6$  metronome is given in Fig. 16, for which the first maximum in past time occurs at 144.6 Ka. This metronome has only very recently been described and used to tune a 10-Myr long Eocene deep-sea sequences characterized by dominant obliquity forcing, from 38 Ma to 48 Ma (Boulila et al., 2018). The joint recovery of  $g_2 - g_5$  and  $s_3 - s_6$  metronomes from two frequency bands in cyclostratigraphy promises to enhance our confidence in astronomically derived timescales.

### 3.3 Classical Tuning

#### 3.3.1 Visual Tuning

Simply looking at a plot of a cyclostratigraphic proxy series, with assistance from a “proviso” time scale when possible, is a crucial first step to establish its potential for providing an astronomical forcing record. In some (albeit mostly rare) cases, the affinity of data with an astronomical signal (i.e., target) is unambiguous, as in Fig. 4 of Hilgen et al. (2014), where it is irresistible to correlate each of the peaks between the data and astronomical target. This is the essence of visual tuning, and this has been in practice from the very beginning, to develop depth-to-time transformations for cyclostratigraphy. Visual tuning is the basis for the “Linage” and “Splinage” functions in Analyseries (Paillard et al., 1996) which plots the data and target side by side and invites the user to use a mouse to select tie points (An equivalent procedure is now also available in the “linage” function of *astrochron*; Meyers, 2014.) However, as discussed in Section 3.3.5, circular reasoning is an ever-present risk in tuning procedures that “force” data-target matches based on visual

patterns, which may vary according to one's "personal equation." Thus, additional measures should be taken to control this problem; some remedies are discussed below.

### 3.3.2 Minimal Tuning

One way to reduce circular reasoning is to tune data to a single astronomical frequency and assess the success or failure of the tuning in aligning other astronomical terms in a procedure known as "minimal tuning" ([Muller and MacDonald, 2000](#)). 405-kyr cycle tuning is the most common implementation of minimal tuning, and is extremely successful. For example, the Cretaceous and Triassic cyclostratigraphic data depicted in [Fig. 13B and C](#) were visually tuned to 405-kyr cycles (see numbered rectangles). Amazingly, even individual spectral peaks in the precession band are as well defined (although at different frequencies) as those in the Cenozoic spectrum of [Fig. 13A](#), which involved another minimal tuning approach, namely limiting the tuning tie points of all of the contributing records to  $\sim 100$  kyr intervals ([Zeeden et al., 2015](#)). This strategy for the Cenozoic data led to the discovery of a change in precession phasing, interpreted as evidence for astronomical forcing of the global deep ocean temperatures as predominantly in the Northern Hemisphere during the late Oligocene, then in the Southern Hemisphere during the Middle Miocene Climate Optimum, and switching back to the Northern Hemisphere during the Quaternary Period ([De Vleeschouwer et al., 2017a](#)). In another example, [Kodama et al. \(2010\)](#) tuned a 4 Myr long ARM proxy of a late Eocene flysch deposit to the La2004 orbital eccentricity solution (see their [Fig. 9](#)) which preserved an October–November precession band phasing (see their [Fig. 11](#)), interpreted as evidence for a Mediterranean climate responding to astronomical forcing.

### 3.3.3 Tune and Release

Another tuning strategy involves tuning to one astronomical frequency, then "releasing" it and tuning to another astronomical frequency. The approach was pioneered by [Imbrie et al. \(1984\)](#), who iteratively tuned bandpass filtered versions of the SPECMAP stack in the precession and obliquity bands to the BER1978 solution for a total of 120 iterations. The procedure, however, never became popular and has not been used since then. Recently, [Yao et al. \(2015\)](#) tested a similar approach, bandpass filtering their Late Permian chert–mudstone rank series to isolate an obliquity signal, tuning it to 32 kyr (predicted for the Late Permian), then

bandpass filtering the results for the long precession — which is actually a multiple frequency component — and tuning that to 20.2 kyr, and finally bandpass filtering those results for the obliquity band and retuning to the 32 kyr obliquity to restore any multiple components in the long precession (procedure demonstrated in Fig. 3 of [Yao et al., 2015](#)).

### **3.4 Sedimentological Tuning**

While the classical tuning techniques discussed above manipulate data in a variety of ways to “fit” the astronomical target, there are other non-manipulative procedures based completely on sedimentological criteria —and currently severely underutilized, or not utilized at all — that have been shown to focus astronomical frequencies in cyclostratigraphy. These are as follows.

#### **3.4.1 Aluminum Tuning**

In marine sediment (weight percent) aluminum concentrations are typically extremely low, and their fluctuations along a section are mostly the result of variable accumulation of the remaining sediment. Thus, correcting aluminum concentrations to a constant value by adjusting the time scale can be used to estimate sedimentation rates along a section. Application of this approach to the Pleistocene SPECMAP V28–238  $\delta^{18}\text{O}$  record significantly sharpened the power spectrum at the obliquity and precession index frequencies ([Kominz et al., 1979](#)). However, the procedure has not been used since then. “Aluminum tuning” (or a modernized or equivalent version of it) could be reinstated with potential great success given the rise of XRF core scanning ([Croudace and Rothwell, 2015](#)).

#### **3.4.2 Carbonate Tuning**

[Herterich and Sarnthein \(1984\)](#) assumed a constant sedimentation rate for the noncarbonate fraction and a variable sedimentation rate for the carbonate fraction in their carbonate-rich Brunhes section to model an incremental timescale along the section. Application of the model increased obliquity and precession spectral power, and resolved 23 kyr and 19 kyr spectral peaks in the precession band. A similar procedure is described in [Herbert et al. \(1986\)](#) for estimating carbon fluxes according to the Albian Piobbico core.

#### **3.4.3 Depth-Derived Time Scales**

Depth-derived time scale modeling considers cyclostratigraphy from multiple sections for a given time interval, and the availability of independent

time control, e.g., radioisotopic data (Huybers and Wunsch, 2004; Huybers, 2007). Common stratigraphic features, e.g., magnetic reversals, are taken as time-correlative control points among the sections. Independent time control is used to develop a preliminary sedimentation rate model for each section, and to assign ages to the control points. The mean age of each control point across all sections and its uncertainty is then estimated. The goal is to retain variability in the time-calibrated signal that might be due to nonlinear climate change. The variant of the method was applied to a basin-wide set of sections from the Eocene Green River Formation, USA (Aswasereelert et al., 2013), leading to new insights: alluvial sediments alternating with carbonate-rich lacustrine sediments recorded  $\sim 100$  kyr cycles, while shorter cycles were recorded preferentially by lacustrine sediments.

### **3.4.4 Turbidite, Conglomerate Removal**

Cyclostratigraphy depends on the assumption that sedimentation rates are stable (constant), or slowly varying, such as a pelagic rain in a marine basin. A turbidite represents an instantaneous depositional event, in which a thick (cm to m) and sometimes relatively coarse sedimentary layer is deposited in a matter of minutes to hours. Thus, while the normal sedimentation mode at a depositional site might involve very slow sedimentation rates, e.g., 1 cm/kyr, a 1 cm turbidite represents less than a day. Turbidites therefore “contaminate” a basinal section, and if included can severely distort time-scale estimates. The solution is simply to remove the turbidite(s) prior to analyzing a cyclostratigraphic section for astronomical forcing. This was done in a study of the Triassic basinal Buchenstein beds, which dramatically reduced the number of spectral peaks in the turbidite-free version of the cyclostratigraphic proxy series (Maurer et al., 2004). In a related procedure, thick conglomerate intervals were removed from the gamma ray log of an extended, cyclic lacustrine-fluvial-alluvial sequence from the Lower Cretaceous of Songliao Basin (China), which clarified a strong orbital eccentricity signal in the log (Liu et al., 2017b).

## **3.5 Statistical Tuning**

### **3.5.1 Average Spectral Misfit (ASM)**

The average spectral misfit (ASM) method was developed for cyclostratigraphy with uncertain timescales (Meyers and Sageman, 2007). The method relies on preliminary spectral analysis of cyclostratigraphic data to identify statistically significant “line” frequencies with multitaper F-testing (Thomson, 1982, 2009). Detected data lines exceeding a pre-determined

significance level (e.g., 95%) are input to ASM, which computes the difference between the set of data line frequencies converted from stratigraphic (e.g., cycles/cm) to time domain (e.g., cycles/kyr) with a test sedimentation rate, and the set of target line frequencies of an astronomical model. The procedure is repeated over a range of test sedimentation rates to find the minimum ASM.

Additionally, for each sedimentation rate, Monte Carlo simulation is performed by randomizing the data line frequencies (in cycles/kyr) for large number of trials (e.g., 10,000) and computing the ASM value for each trial. The number of trials with ASM values indicating a difference of zero between the sets of data and target lines is used as an estimate of the significance level for rejection of the null hypothesis ( $H_0$ : no astronomical signal) for the original ASM value.  $H_0$  below a critical significance level is taken as evidence for frequencies in the data that are consistent with those of the astronomical model. This has been suggested to be the inverse of the total number of investigated test sedimentation rates (e.g., 0.02 for a run with 500 sedimentation rates). The optimal sedimentation rate is the one with the lowest ASM value and  $H_0$  with the highest significance level and lowest P value. This method is provided in the “asm” function of the *astrochron* package in R (Meyers, 2014). For cases where significant variations in sedimentation rate are suspected along a cyclostratigraphic section, an “evolutionary” version of ASM is available, that calculates the ASM procedure along a running window through the section, provided as “eAsm” in *astrochron*.

### 3.5.2 Bayesian Tuning

Malinverno et al. (2010) developed a “Bayesian Monte Carlo” approach to search for the sedimentation rate in a cyclostratigraphic proxy series that maximizes spectral power at the astronomical frequencies. The Monte Carlo method is used to develop uncertainties for the estimated sedimentation rate. This can be applied with a running window to estimate sedimentation rates through sections. However, since its introduction and application to the Aptian Selli Event interval, it has not been used.

Lin et al. (2014) developed a procedure for the alignment of stratigraphic records that applies Bayesian inference and hidden Markov modeling to develop the probability distribution for the alignment, which is then used for estimating its uncertainty. Their set of MATLAB scripts is available at: [http://ccmbweb.ccv.brown.edu/cgi-bin/download\\_HMM\\_Match.pl](http://ccmbweb.ccv.brown.edu/cgi-bin/download_HMM_Match.pl).

### 3.5.3 TimeOpt and TimeOptMCMC

The time optimization (timeOpt) method was developed with the same goals as ASM. However, in this case cyclostratigraphy is analyzed for the sedimentation rate that optimizes orbital eccentricity frequency characteristics of the precession index amplitude envelope, and power at the precession index and orbital eccentricity frequencies (Meyers, 2015). For each test sedimentation rate, the data are fitted to model precession index and orbital eccentricity time series in two steps: (1) the data are band-pass filtered and Hilbert transformed to isolate the precession index amplitude envelope. This envelope is then linearly regressed on a model time series with orbital eccentricity frequencies, and the result is reported together with the squared model-data Pearson correlation coefficient  $r_{\text{envelope}}^2$ ; and (2) the data are linearly regressed on a model time series with orbital eccentricity and precession index frequencies, and the result is reported together with the squared model-data Pearson correlation coefficient  $r_{\text{power}}^2$ .

The product  $r_{\text{opt}}^2 = r_{\text{envelope}}^2 \cdot r_{\text{power}}^2$  indicates the fraction of power shared by the precession index envelope and the orbital eccentricity plus precession index time series. For a perfect data-model fit, and perfect synchronization, as would be the case between the precession index, its amplitude envelope and the orbital eccentricity,  $r_{\text{opt}}^2 = 1$ . However,  $r_{\text{opt}}^2$  is typically much lower than 1 due to data filtering and noise; Monte Carlo simulation is required to evaluate the statistical significance of the computed  $r_{\text{opt}}^2$  maximum (Meyers, 2015). This method is available in the “timeOpt” and “timeOptSim” functions in the *astrochron* package in R (Meyers, 2014).

An important extension – time optimization with Markov Chain Monte Carlo simulation – was recently introduced in order to search additionally for optimal  $k$  ( $= p_{\odot + C}$ ) (Eq. 4) and  $g_1$  to  $g_5$  for the model. This was applied to two cyclostratigraphic sections, one from the 1.4 Ga Xiamaling Formation (China) and the other from the 55 Ma Walvis Ridge ODP Core 1262, for joint optimization of sedimentation rate,  $k$ , and  $g_1$  to  $g_5$  (Meyers and Malinverno, 2018). The procedure is available in the function “timeOptMCMC” in *astrochron* 0.8.

### 3.5.4 Correlation Coefficient (COCO)

As with ASM (Section 3.5.2), the correlation coefficient (COCO) method of Li et al. (2018b) evaluates two problems simultaneously: (1) a potential astronomical signal in cyclostratigraphy, and (2) stratigraphic distortion

due to variable sedimentation rates. COCO estimates the correlation coefficient between the power spectra of an astronomical target signal and paleoclimate proxy series across a range of test sedimentation rates. As with ASM, a null hypothesis of no astronomical forcing is evaluated using Monte Carlo simulation. When applied using a sliding stratigraphic window, “eCOCO” estimates sedimentation rate variations along cyclostratigraphic sections, and other insights into astronomical forcing.

### **3.5.5 Other Assorted Techniques**

Other techniques that have been developed for establishing statistically based fits between cyclostratigraphy and astronomical targets include: linear inversion (Martinson et al., 1982), varimax norm demodulation (Schiffelbein and Dorman, 1986), a minimal cost function method (Bruggemann, 1992), dynamic optimization (Yu and Ding, 1998), dynamic programming (Lisiecki and Lisiecki, 2002), CORRELATOR (Olea, 1994, 2004), precession-eccentricity optimization (Zeeden et al., 2015), dynamic time warping (Kotov and Pälike, 2017), and automatic correlation optimization (Zeeden et al., 2018).

Finally, for stratigraphic cycles defined by repeating sub-facies, “gamma analysis” was designed to estimate the sedimentation rates of individual subfacies contributing to a cycle (Kominz and Bond, 1990; Kominz et al., 1991). In each cycle, the thickness of the  $i$ th subfacies  $c_i$  has an unknown inverse sedimentation rate  $\gamma_i$ , and so the periodicity of the cycle with  $N$  subfacies is:  $T_{cy} = \sum_{i=1}^N \gamma_i c_i$ . If the cycle period is unknown,  $T_{cy} = 1$  is assumed. There is an equation for each cycle, so for a total of  $N$  cycles each occurring with a period  $T_{cy}$ , the set of  $N$  equations is inverted to solve for  $\gamma_i$ .

## **3.6 Astronomical Time Scale**

The Astronomical Time Scale (ATS) is based on astronomical solutions matched with cyclostratigraphy that is correlated with global chronostratigraphy. There are “anchored” and “floating” versions of the ATS, the former anchored to the present day, and the latter to high-precision geochronologic dates in the GTS. For 0 to 5 Ma, insolation models are typically used for matching; earlier than 5 Ma, the effects of shorter LOD on precession need to be included, astronomical targets such as “P-0.5T La2004<sub>1,1</sub>” (e.g., Zeeden et al., 2014) may become standard targets for early Neogene

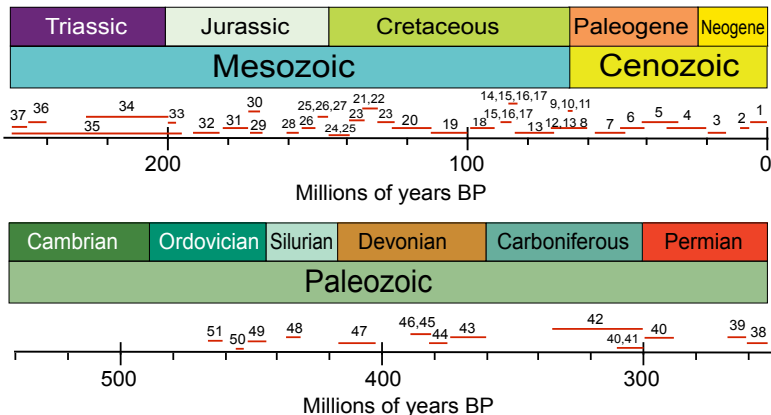
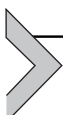


**Figure 17** Major sequences of  $g_2 - g_5$  cycles in the cyclostratigraphic record. A detailed list of the numbered sources (1–50) appears in [Appendix G](#). Additional information for the Mesozoic is provided in [Huang \(2018\)](#).

and Paleogene cyclostratigraphy. At all times, identification of the 405-kyr metronome is a priority. [Fig. 17](#) shows the current 405-kyr metronome coverage in the cyclostratigraphic record (detailed list in [Appendix G](#)). The formal presentation of the ATS should have a format such as presented in the figures of [Huang \(2018\)](#).



#### 4. CONCLUSIONS

In 2018, cyclostratigraphy can be said to have entered a “golden age”, with multi-million year-long sequences now routine in data collecting, many of these exceeding 10 Myr in duration. These new datasets represent major contributions to the geologic time scale with dominantly deterministic astronomical metronomes readily recognized in the cyclic successions. The principal metronome originates from the interactions of the orbital perihelia of Venus and Jupiter,  $g_2 - g_5$  with a periodicity of 405-kyr and is commonly found in cyclostratigraphy dominated by precession and orbital eccentricity forcing (see Huang, this volume). The La2004 405-kyr metronome defined by the +5 Myr to −15 Myr integration (Table 6 in [Laskar et al., 2004](#)) is valid as far back as 215 Ma ([Kent et al., 2018](#)). A second metronome originating from the orbital inclinations of Earth and Saturn,  $s_3 - s_6$  with a periodicity of 173-kyr occurs in cyclostratigraphy dominated by obliquity forcing. In the future, the assessment of

jointly occurring  $g_2 - g_5$  and  $s_3 - s_6$  metronomes will provide greater confidence in astrochronology than either metronome on its own.

The accuracy of astrochronology is sufficient for high quality intercalibration with radioisotope geochronology. The integration of both information sources is expected to lead to improved time scales that are continuous and precise at an unprecedented level (achieving 0.05% age uncertainty).

The application of optimization methods to solve for Earth's precession, and planetary secular frequencies for times prior to 50 Ma represents a major advance in cyclostratigraphy, and will provide detailed constraints for Solar System modeling in the very near future.

The next line of inquiry in cyclostratigraphy will involve investigation of Solar System resonance state and chaotic events through geologic time. This goes hand in hand with the long sequences now being assembled, in light of the million-year period modulations that need to be recovered for this purpose.

Finally, in the high stakes race to discover astronomical forcing signals in cyclostratigraphy, understanding the pathway from insolation to stratigraphy has been severely shortchanged. Thus, the other future major line of inquiry will involve modeling insolation forcing of the paleoclimate system, and the responses of the depositional systems that have inherited the astronomical signal.



## APPENDIX A – CALCULATION OF EARTH'S ORBITAL ECCENTRICITY AND INCLINATION

### A.1 La2010 Solution Files

At: <http://vo.imcce.fr/insola/earth/online/earth/earth.html>, e.g., in the “Data files here” link under “Solutions La2010 for Earth orbital elements from –250 Myr to the present,” the file “La2010d\_alkhqp3L.dat” provides values for La2010d:

t: the time from J2000 (in kyr) (negative back in time)

a: semi-major axis

l: mean longitude (expressed in radians)

k:  $e \cos(\Pi)$

h:  $e \sin(\Pi)$

q:  $\sin(l/2) \cos(\Omega)$

p:  $\sin(l/2) \sin(\Omega)$

(Note: In the main text, the subscript “3” is used to designate the Earth’s orbital elements.)

## A.2 Orbital Eccentricity

For time t, given:  $k = e \cos \Pi$  and  $h = e \sin \Pi$ :

$$k^2 + h^2 = e^2 (\cos^2 \Pi + \sin^2 \Pi) = e^2$$

$$e = \sqrt{(k^2 + h^2)}$$

## A.3 Orbital Inclination

For time t, given:  $q = \sin(I/2) \cos \Omega$  and  $p = \sin(I/2) \sin \Omega$ :

$$q^2 + p^2 = \sin^2(I/2) (\cos^2 \Omega + \sin^2 \Omega) = \sin^2(I/2)$$

$$\sin(I/2) = \sqrt{q^2 + p^2}$$

$$I = 2 \sin^{-1} \left( \sqrt{q^2 + p^2} \right)$$



## APPENDIX B – ASTRONOMICAL SOLUTIONS TRANSFORMATIVE TO CYCLOSTRATIGRAPHY

### B.1 Analytical Solutions

LEVER1855 ([Le Verrier, 1855](#)) orbital eccentricity and obliquity solution.  
STOCK1873 ([Stockwell, 1873](#)) originally completed in 1870.

LEVMS1931 ([Miskovitch, 1931](#)) solution based on LEVER1855.

BROVW1960 ([Brouwer and van Woerkom, 1950](#)) includes terms up to the sixth degree in the eccentricities and inclinations of Jupiter and Saturn, and terms related to the “great inequality”, i.e. the near equality to the 5:2 mean motion resonance between Jupiter and Saturn up to the second order in planetary masses.

SHABU1967 ([Sharaf and Budnikova, 1967, 1969](#)) (corrections to BROVW1960)

VERNE1972 ([Vernekar, 1972](#)) (BROVW1960 corrected by SHABU1967)  
BRETA1974 ([Bretagnon, 1974](#)) includes terms up to the fourth degree in planetary eccentricities and inclinations, and up to second order in planetary masses.

BER78 (Berger, 1978) based on BRETA1974, with FORTRAN code to compute insolation.

## B.2 Numerical Integrations

La1990 (Laskar, 1990) includes terms up to the sixth degree in planetary eccentricities and inclinations, and up to second order in planetary masses.

La1993 (Laskar et al., 1993) includes adjustable parameters for Earth rotation and dynamical ellipticity with the La1990 solution, valid from 0 to 35 Ma.

La2004 (Laskar et al., 2004) is a numerical solution for full Solar System with an Earth precession model based on LLR observations, orbital solution valid from 0 to 40 Ma.

La2010 (Laskar et al., 2011a) incorporates new INPOP planetary ephemeris, no Earth precession model, 4 solutions, valid from 0 to 50 Ma.

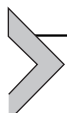
La2011 (Laskar et al., 2011b; Laskar et al., 2012) inclusion of asteroid bodies, no Earth precession model, valid from 0 to 50 Ma.

ZB2017 (Zeebe, 2017) new integrator algorithms, separate Moon, asteroids, no Earth precession model, 17 solutions, valid from 0 to 54 Ma.

La1990–2010a-d models are at: <http://vo.imcce.fr/insola/earth/online/earth/earth.html>.

La2011 model is provided in the ‘getLaskar’ function of the astrochron for R package (Meyers, 2014).

Zeebe models are at: [https://www.soest.hawaii.edu/oceanography/faculty/zeebe\\_files/Astro.html](https://www.soest.hawaii.edu/oceanography/faculty/zeebe_files/Astro.html).



## APPENDIX C – VARIABLES OF EARTH’S PRECESSION

### C.1 – Luni-Solar Precession

The annually averaged net torque due to gravitational forcing from the Sun is (p. 712, Williams, 1994):

$$\tau_{\odot} = \frac{3Gm_{\odot}(C - A)\sin\epsilon \cos\epsilon}{2a^3(1 - e^2)^{3/2}}$$

This results in retrograde precession (see Fig. 3) of the Earth’s rotation axis:

$$\begin{aligned} \frac{d\psi_{\odot}}{dt} &= \frac{\tau_{\odot}}{C\phi \sin\epsilon} = \frac{3Gm_{\odot}(C - A)\cos\epsilon}{2C\phi a^3(1 - e^2)^{3/2}} = 2.450183 \times \frac{10^{-12}}{\text{s}} \\ &= 15.948788 \text{ arcseconds/year} \end{aligned}$$

Similarly, gravitational forcing from the Moon, with an added factor to account for the lunar orbital inclination  $I_{\text{C}}$  with respect to the Earth, results in:

$$\begin{aligned}\frac{d\psi_{\text{C}}}{dt} &= \frac{\tau_{\text{C}}}{C\phi \sin e} = \frac{3Gm_{\text{C}}(C-A)\cos e}{2C\phi a_{\text{C}}^3(1-e_{\text{C}}^2)^{3/2}} \left(1 - \frac{3}{2}\sin^2 I_{\text{C}}\right) \\ &= 5.334529 \times \frac{10^{-12}}{\text{s}} = 34.723638 \text{ arcseconds/year}\end{aligned}$$

The sum gives the luni-solar total of 50.672426 " /year and in general:

$$\begin{aligned}\frac{d\psi_{\odot}}{dt} + \frac{d\psi_{\text{C}}}{dt} &= \frac{3Gm_{\odot}(C-A)\cos e}{2C\phi a^3(1-e^2)^{3/2}} \\ &\quad + \frac{3Gm_{\text{C}}(C-A)\cos e}{2C\phi a_{\text{C}}^3(1-e_{\text{C}}^2)^{3/2}} \left(1 - \frac{3}{2}\sin^2 I_{\text{C}}\right) \\ &= \frac{3Gm_{\odot}(C-A)\cos e}{2C\phi a^3(1-e^2)^{3/2}} + \frac{3Gm_{\text{C}}(C-A)\cos e}{2C\phi a_{\text{C}}^3(1-e_{\text{C}}^2)^{3/2}} \left(1 - \frac{3}{2}\sin^2 I_{\text{C}}\right) \\ \frac{d}{dt}(\psi_{\odot} + \psi_{\text{C}}) &= \frac{3GH}{2\phi} \left[ \frac{m_{\odot}}{a^3(1-e^2)^{3/2}} + \frac{m_{\text{C}}(1-\frac{3}{2}\sin^2 I_{\text{C}})}{a_{\text{C}}^3(1-e_{\text{C}}^2)^{3/2}} \right] \cos e = p_{\odot+\text{C}}\end{aligned}$$

This appears as Eq. (4) in the main text (This derivation benefitted from online notes by [Mclemore and Koonce, 2016](#)).

## C.2 – Orbital Contributions to Precession and Obliquity

Given  $p$  and  $q$  for the Earth ([Appendix A](#) above), the following expressions provide the planetary perturbation contributions to the precession and obliquity equations (Eq. 5 in the main text):

$$\begin{aligned}\mathcal{A}(t) &= \frac{2}{\sqrt{1-p^2-q^2}} [\dot{q} + p(q\dot{p} - p\dot{q})] \\ \mathcal{B}(t) &= \frac{2}{\sqrt{1-p^2-q^2}} [\dot{p} - q(q\dot{p} - p\dot{q})] \\ \mathcal{C}(t) &= q\dot{p} - p\dot{q}\end{aligned}$$

with

$$\dot{p} = \frac{dp}{dt} \text{ and } \dot{q} = \frac{dq}{dt}$$

### C.3 – Variable Definitions

$\phi$  – Earth rotation rate ( $7.2921150 \times 10^{-5}$  rad/s at J2000, IERS)

$G$  = gravitational constant ( $6.67408 \times 10^{-11} \text{ m}^3/(\text{kg s}^2)$ )

$H$  – Earth dynamical ellipticity =  $(C-A)/C$  (present-day: 0.003273787)

$A$  – Earth's equatorial moment of inertia ( $8.008 \times 10^{37} \text{ kg/m}^2$ )

$C$  – Earth's polar moment of inertia ( $8.034 \times 10^{37} \text{ kg/m}^2$ )

$a$  – semi-major axis of Earth's orbit ( $1.4959802 \times 10^{11} \text{ m}$  at J2000, IERS)

$e$  – Earth orbital eccentricity (0.016708634 at J2000, IERS)

$a_C$  – semi-major axis of Moon's orbit ( $3.833978 \times 10^8 \text{ m}$  at J2000, IERS)

$e_C$  – eccentricity of the Moon's orbit (0.05554553 at J2000, IERS)

$I_C$  – inclination of Moon orbit on the ecliptic (5.156690 at J2000, IERS)

$m_C$  – mass of the Moon ( $7.34767309 \times 10^{22} \text{ kg}$ )

$m_\odot$  – mass of the Sun ( $1.98855 \times 10^{30} \text{ kg}$ ) (=27068510  $m_C$ )

$Gm_\odot = 1.3271244 \times 10^{20} \text{ m}^3/\text{s}^2$  (at J2000, IERS)

$Gm_C = 4.902799 \times 10^{12} \text{ m}^3/\text{s}^2$  (at J2000, IERS)

$\epsilon$  – obliquity angle of Earth (23.43928 at J2000, IERS)

$\odot$  – symbol for the Sun

$\subset$  – symbol for the Moon

$\oplus$  – symbol for the Earth



## APPENDIX D – LUNAR RECESSION AND EARTH DECELERATION

In the Earth–Moon system, tidal dissipation results in a transfer of angular momentum from the Earth to Moon. The Earth's rotational angular momentum is  $L_E = C\phi$ , and the Moon's orbital angular momentum is  $L_M = \kappa L_E$ , where present-day  $\kappa = 4.93$ . Assuming that tidal friction caused by Moon and Sun is independent and proportional to the square of the ratio of their tidal amplitudes (0.46) (Eq. 2 in [Deubner, 1990](#)):

$$dL_E = -dL_M \left[ 1 + (0.46)^2 \left( \frac{a_0}{a} \right)^6 \right]$$

Integrating and rearranging Eq. (3) in [Deubner \(1990\)](#) gives:

$$\frac{\phi}{\phi_0} = 6.00967 - 4.93 \left( \frac{a}{a_0} \right)^{\frac{1}{2}} - 0.080245231 \left( \frac{a}{a_0} \right)^{\frac{13}{2}}$$

where  $\phi_0$  is present-day  $\phi$  ( $=7.2921150 \times 10^{-5}$  rad/s) and  $a_0$  is present-day lunar semi-major axis ( $=3.833978 \times 10^8$  m). A detailed treatment of the problem is provided in Chapter 10 of [Lambeck \(1980\)](#).



## APPENDIX E – EARTH-MOON ROCHE LIMIT

The Roche Limit is the distance between two attracting bodies at which the smaller of the two bodies experiences disruptive forces that are sufficient to break it part. The Roche Limit (in km) for the Earth–Moon system, assuming rigid bodies is (p. 53, [Lowrie, 2007](#)):

$$d_R = R_{\oplus} \left[ 2 \left( \frac{\rho_{\oplus}}{\rho_{\odot}} \right) \right]^{\frac{1}{3}} = 1.4887 \times 6371 \text{ km} = 9484 \text{ km}$$

where  $R_{\oplus}$  = Earth radius = 6371 km  $\rho_{\oplus}$  = Earth mean density = 5.51 g/cm<sup>3</sup>  $\rho_{\odot}$  = Moon mean density = 3.34 g/cm<sup>3</sup>



## APPENDIX F – CALCULATING THE $g_2-g_5$ AND $s_3-s_6$ METRONOMES WITH LA2004

The following two MATLAB scripts calculate the  $g_2-g_5$  and  $s_3-s_6$  metronomes for 0–1 Ma:

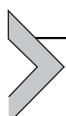
```
% This calculates g2-g5
% using the formula in Table 6 of Laskar et al., 2004;
% negative time t in years BP (into the past)
dt = -1.; % 1 year sample rate (change to -1000 for kyr)
t = 0:dt:-1000000; % 0 to 1 million years BP (negative time)
% e0, mu, b and faz from Laskar et al., 2004, Table 6
e0 = 0.0275579;
mu = 3.199279*pi/(3600*180); % convert to radians
b = 0.010739;
faz = 170.739*pi/180.; % convert to radians
```

```

ecc405 = e0+b*cos(mu*t + faz);
figure; plot(t,ecc405);

% This calculates s3–s6
% using s3 and s6 from Table 5 and Eq. 26 in Laskar et al., 2004;
% negative t in years BP (into the past)
dt = -1.; % 1 year sample rate (change to -1000 for kyr)
t = 0:dt:-1000000; % 0 to 1 million years BP (negative time)
t = t';
s3a = 0.01377449*cos((-18.845116*pi/(3600*180))*t-pi*111.31/180);
s3b = 0.01377449*sin((-18.845116*pi/(3600*180))*t-pi*111.31/180);
s6a = 0.00133215*cos((-26.34788*pi/(3600*180))*t + pi*127.306/180);
s6b = 0.00133215*sin((-26.34788*pi/(3600*180))*t + pi*127.306/180);
s36a = s3a-s6a;
s36b = s3b-s6b;
s36 = sqrt(s36a.^2 + s36b.^2);
figure; plot(t,s36);

```



## APPENDIX G – MAJOR SEQUENCES OF $g_2$ – $g_5$ CYCLES IN THE GEOLOGIC RECORD

The following is a list of publications that describe  $g_2$ – $g_5$  cycles in cyclostratigraphic sections. Coverage in geologic time is summarized in Fig. 17; bold numbers refer to the labels in the figure; approximate time intervals (and durations) are also given. For the Mesozoic, additional detailed information is provided in Huang (2018).

### **Cenozoic**

#### ***Neogene***

Pliocene-Pleistocene: (1) Nie, 2017: 0–5.5 Ma (5.5 Myr)

Miocene: (2) Hilgen et al., 1999: 6.6–9.5 Ma (3.1 Myr); (3) Miller et al. (2017): 14–20 Ma (6 Myr)

Oligocene: (4) Pälike et al., 2006: 23–36 Ma (13 Myr)

#### ***Paleogene***

Eocene: (5) Westerhold et al., 2014: 31–43 Ma (12 Myr); (6) Westerhold et al., 2015: 41–49 Ma (8 Myr)

Paleocene: (7) [Westerhold et al., 2012](#): 48–58 Ma (10 Myr); (8) [Hilgen et al., 2015](#): 61–66 Ma (5 Myr)

K/Pg boundary: (9) [Kuiper et al., 2008](#); (10) [Renne et al., 2013](#); (11) [Hennebert, 2014](#).

## Mesozoic

### Cretaceous

Maastrichtian: (12) [Batenburg et al., 2014](#): 66–72 Ma (6 Myr); (13) [Wu et al., 2014](#): 66–72.1 Ma (6.1 Myr)

Campanian: (13) [Wu et al., 2014](#): 70.5–83.4 Ma (12.9 Myr)

Santonian: (14) [Thibault et al., 2016](#): 84–87 Ma (3 Myr); (15) [Wu et al., 2013](#): 83.6–86.3 Ma (3.3 Myr); (16) [Sageman et al., 2014](#): 84.19–86.49 Ma (2.3 Myr); (17) [Locklair and Sageman, 2008](#):

Coniacian: (15) [Wu et al., 2013](#): 86.3–89.6 Ma (3.6 Myr); (16) [Sageman et al., 2014](#): 86.49–89.75 Ma (3.26 Myr)

Turonian: (18) [Eldrett et al., 2015](#): 89.75–94.1 Ma (4.35 Myr)

Cenomanian: (18) [Eldrett et al., 2015](#): 94.1–98 Ma (4.1 Myr; *upper part*)

Albian: (19) [Grippo et al., 2004](#): 101–113 Ma (12 Myr)

Aptian: (20) [Huang et al., 2010a](#): 113–126 Ma (13 Myr)

Barremian: (21) [Hinnov et al., 2008](#): 126–131.67 Ma (5.67 Myr) (based on (22) [Fiet and Gorin, 2000](#))

Hauterivian: (23) [Martinez et al., 2015](#): 129.5 to 135.25 Ma or 126.1 to 132 Ma (5.265 Myr)

Valanginian: (23) [Martinez et al., 2015](#): 135.25–140.25 Ma or 132 to 137 Ma (5.08 Myr)

Berriasian: (24) [Huang et al., 2010c](#): 137.8 to 144.7 Ma (6.9 Myr; *Upper Volgian*); (25) [Kietzmann et al., 2015](#): 139.9–145 Ma (5.1 Myr)

## Jurassic

Tithonian: (25) [Kietzmann et al., 2015](#): 145–149 Ma (4 Myr; *upper part*) (26) [Huang et al., 2010b](#): 147.2–150.52 Ma (2.5 Myr; *lower part*) (27) [Rameil, 2005](#): 6.8 Myr.

Kimmeridgian: (26) [Huang et al., 2010b](#): 147.2–153.93 Ma (6.73 Myr)

Oxfordian: (28) [Boulila et al., 2010](#): 157.2–161.2 Ma (4 Myr; *lower-middle part*)

Callovian: Incomplete data

Bathonian: Incomplete data

Bajocian: (29) [Sucheras-Marx et al., 2013](#): ~168–172 Ma (4.1 Myr; lower part)

Aalenian: (30) [Huret et al., 2008a, 2008b](#): 170.85–174.7 Ma (3.85 Myr);  
(29) [Sucheras-Marx et al., 2013](#): (0.94 Myr; upper part)

Toarcian: (31) [Boulila et al., 2014](#): 174.7–183 Ma (8.3 Myr)

Pliensbachian: (32) [Ruhl et al., 2016](#): 183.8–192.5 Ma (8.7 Myr); [Ikeda and Tada, 2014](#): xxx–yyy (zzz)

Sinemurian–Hettangian: (33) [Hüsing et al., 2014](#): 197.3–200 Ma (2.7 Ma;  
*lower Sinemurian*)

### ***Triassic***

Rhaetian: (34) [Kent et al., 2017](#): 205.5–201.4 Ma (4.1 Myr); (35) [Ikeda and Tada, 2014](#): 208.5–201.4 Ma (7.1 Myr)

Norian: (34) [Kent et al., 2017](#): 227–205.5 Ma (21.5 Myr); [Ikeda and Tada, 2014](#): 225–208.5 Ma (16.5 Myr)

Carnian: (35) [Ikeda and Tada, 2014](#): 235.2–225 Ma (10.2 Myr)

Ladinian: [Ikeda and Tada, 2014](#): xxx–235.2 Ma (xxx Myr)

Anisian: (36) [Li et al., 2018a](#): 241–247 Ma (6 Myr)

Induan–Olenekian: (37) [Li et al., 2016](#): 252–247 Ma (5 Myr)

### **Paleozoic**

#### ***Permian***

Wuchiapingian–Changhsingian: (38) [Wu et al., 2013](#): 260–251 Ma (9 Myr)

Wordian–Capitanian: (39) [Fang et al., 2017](#): 262–269 Ma (7 Myr)

Asselian–Artinskian: (40) [Schmitz and Davydov, 2012](#): 288–299 Ma  
(11 Myr; lower Artinskian)

#### ***Carboniferous***

Moscovian–Gzhelian: (41) [Davydov et al., 2010](#); (40) [Schmitz and Davydov, 2012](#): 299–309 Ma (10 Myr; upper Moscovian)

Visean–Gzhelian: (42) [Wu et al., 2018a, 2018b](#): 299–333 Ma (34 Myr; upper Visean)

Tourniasian: Incomplete data

#### ***Devonian***

Famennian: (43) [Pas et al., 2018](#): 358.9–372.2 Ma (13.5 Myr)

Frasnian: (44) [De Vleeschouwer et al., 2012](#): 376.7–383.6 Ma (6.9 Myr)

Givetian: (45) [De Vleeschouwer et al., 2015](#): 383.6–387.95 Ma (4.35 Myr)

Eifelian: (46) [Ellwood et al., 2015](#): 387.95–394.16 Ma (6.21 Myr)

Emsian: No data

Lockovian–Pragian: (47) [Da Silva et al., 2016](#): 404–418 Ma (14 Myr)

### ***Silurian***

Pridoli: No data

Ludfordian: No data

Gorstian: No data

Homerian: Incomplete data

Sheinwoodlian: No data

Telychian: (48) [Gambacorta et al., 2018](#): 433.4–438.86 Ma (5.46 Myr)

Aeronian: No data

Rhuddanian: Incomplete data

### ***Ordovician***

Katian–Hirnantian: (49) [Hinnov and Diecchio, 2015](#): 443–450 Ma (7 Myr)

Sandbian: (50) [Fang et al. \(2016\)](#): 453–456 Ma (3 Myr; *upper part*)

Darwillian–Dapingian: (51) [Rasmussen et al., 2018](#): 463–468.5 Ma (5.5 Myr; *upper Dapingian, lower Darwillian*)

Floian: No data

Tremadocian: No data.

*Cambrian*: No data.

## **ACKNOWLEDGMENTS**

My deep gratitude goes to Alfred G. Fischer (★December 12, 1920 – †July 2, 2017), who supported my effort to understand cyclostratigraphy for more than 30 years. Al's scientific leadership and meticulous documentation of the cyclic sedimentary record, and his ability to synthesize complex concepts throughout his life inspired countless geologists in their careers. Al was responsible for the term "cyclostratigraphy" and he quickly adapted new ideas into his research, for example, the recognition of 405-kyr cycles and their use as a metronome. He was responsible for the 405-kyr cycle definitions in the Aptian-Albian Piobbico core record highlighted in this paper. I thank Jim Ogg, who has tirelessly supported and promoted cyclostratigraphic research for decades, carefully integrating cyclostratigraphy into the International Geologic Time Scale 2004, 2008, 2012, 2016, and now the upcoming GTS 2020. I am grateful to my long-time colleague David Florkowski, who through many years has never failed to alert me about new developments in signal processing, Solar System modeling, geodynamics, and much, much more. Finally, I thank all of my long-suffering, wonderful colleagues and co-authors for their graciousness in always sharing their data and including me in their research, and reviewer Christian Zeeden, who provided incisive and valuable comments that greatly improved this presentation.

## REFERENCES

- Al Husseini, M.I., 2015. Arabian orbital stratigraphy revisited – AROS 2015. *GeoArabia* 20 (4), 183–216.
- Algeo, T.J., Heckel, P.H., 2008. The late Pennsylvanian Midcontinent Sea of North America: a review. *Palaeogeogr. Palaeoclimatol. Palaeoecol.* 268, 205–221. <https://doi.org/10.1016/j.palaeo.2008.03.049>.
- Anderson, R.Y., 2011. Enhanced climate variability in the tropics: a 200 000 yr annual record of monsoon variability from Pangea's equator. *Clim. Past* 7, 757–770. <https://doi.org/10.5194/cp-7-757-2011>.
- Anderson, R.Y., 1982. A long geoclimatic record from the Permian. *J. Geophys. Res.* 87 (C9), 7285–7294. <https://doi.org/10.1029/JC087iC09p07285>.
- Aswasereelert, W., Meyers, S.R., Carroll, A.R., Peters, S.E., Smith, M.E., Feigl, K.L., 2013. Basin cyclostratigraphy of the Green River formation. *Geol. Soc. Am. Bull.* 125, 216–228. <https://doi.org/10.1130/B30541.1>.
- Bao, X., Zhang, S., Jiang, G., Wu, H., Li, H., Wang, X., An, Z., Yang, T., 2018. Cyclostratigraphic constraints on the duration of the Datangpo Formation and the onset age of the Nantuo (marinoan) glaciation in South China. *Earth Planet. Sci. Lett.* 483, 52–63. <https://doi.org/10.1016/j.epsl.2017.12.001>.
- Batenburg, S.J., Gale, A.S., Sprovieri, M., Hilgen, F., Thibault, N., Boussaha, M., Orue-Etxebarria, X., 2014. An astronomical time scale for the Maastrichtian based on the Zumaia and Sopelana sections (Basque country, northern Spain). *J. Geol. Soc.* 171, 165–180. <https://doi.org/10.1144/jgs2013-015>.
- Batenburg, S.J., Sprovieri, M., Gale, A.S., Hilgen, F.J., Hüsing, S., Laskar, J., Liebrand, D., Lirer, F., Orue-Etxebarria, X., Pelosi, N., Smit, J., 2012. Cyclostratigraphy and astronomical tuning of the late Maastrichtian at Zumaia (Basque country, Spain). *Earth Planet. Sci. Lett.* 359–360, 264–278. <https://doi.org/10.1016/j.epsl.2012.09.054>.
- Bazykin, D.A., Hinnov, L.A., 2002. Orbitally-driven depositional cyclicity of the Lower Paleozoic Aisha-Bibi seamount (Malyi Karatau, Kazakhstan): integrated sedimentological and time series study. In: Zempolich, W.G., Cook, H.E. (Eds.), Paleozoic Carbonates of the Commonwealth of Independent States (CIS): Subsurface Reservoirs and Outcrop Analogs, pp. 19–41. SEPM Special Publication No. 75.
- Berger, A., 1978. A Simple Algorithm to Compute Long Term Variations of Daily or Monthly Insolation. Contribution No. 18. Institut d'Astronomie et de Géophysique Georges Lemaitre, Université Catholique de Louvain, Louvain-la-Neuve, Belgique, 50 p.
- Berger, A., Loutre, M.-F., 1994. Astronomical forcing through geologic time. In: DeBoer, P.L., Smith, D.G. (Eds.), Orbital Forcing and Cyclic Sequences: International Association of Sedimentologists Special Publication, vol. 19, pp. 15–24.
- Berger, A., Loutre, M.-F., Tricot, C., 1993. Insolation and Earth's orbital periods. *J. Geophys. Res.* 98 (D6), 10341–10362. <https://doi.org/10.1029/93JD00222>.
- Berger, A., Loutre, M.-F., Yin, Q.Z., 2010. Total irradiation during any time interval of the year using elliptic integrals. *Quat. Sci. Rev.* 29, 1968–1982. <https://doi.org/10.1016/j.quascirev.2010.05.007>.
- Berger, A., Loutre, M.-F., Laskar, J., 1992. Stability of the astronomical frequencies over the Earth's history for paleoclimatic studies. *Science* 255, 560–566. <https://doi.org/10.1126/science.255.5044.560>.
- Berger, A., Loutre, M.-F., Dehant, V., 1989. Influence of the changing lunar orbit on the astronomical frequencies of pre-Quaternary insolation patterns. *Paleoceanography* 4, 555–564. <https://doi.org/10.1029/PA004i005p00555>.

- Berry, W.B., Barker, R.M., 1968. Fossil bivalve shells indicate longer month and year in Cretaceous than present. *Nature* 217, 938–939.
- Bond, G.C., Kominz, M.A., Beavan, J., 1991. Evidence for orbital forcing of Middle Cambrian peritidal cycles: Wah Wah range, south-central Utah. *Kansas Geol. Survey Bull.* 233, 294–317.
- Boulila, S., Vahlenkamp, M., De Vleeschouwer, D., Laskar, J., Yamamoto, Y., Pälike, H., Kirkland Turner, S., Sexton, P.E., Westerhold, T., Röhl, U., 2018. Towards a robust and consistent middle Eocene astronomical timescale. *Earth Planet. Sci. Lett.* 486, 94–107. <https://doi.org/10.1016/j.epsl.2018.01.003>.
- Boulila, S., Hinnoy, L.A., Galbrun, B., 2017. A review of tempo and scale of the early Jurassic Toarcian OAE: implications for carbon cycle and sea level variations. *Newslett. Stratigr.* 50, 363–389. <https://doi.org/10.1127/nos/2017/0374>.
- Boulila, S., Galbrun, B., Huret, E., Hinnoy, L.A., Rouget, I., Gardin, S., Huang, C., Bartolini, A., 2014. Astronomical calibration of the Toarcian Stage: implications for sequence stratigraphy and duration of the early Toarcian OAE. *Earth Planet. Sci. Lett.* 386, 98–111.
- Boulila, S., Galbrun, B., Hinnoy, L.A., Collin, P.-Y., Ogg, J.G., Fortwengler, D., Marchand, D., 2010. Milankovitch and sub-milankovitch forcing of the oxfordian (late jurassic) terres Noires formation (SE France) and global implications. *Basin Res.* 22, 712–732. <https://doi.org/10.1111/j.1365-2117.2009.00429.x>.
- Bretagnon, P., 1974. Termes à longues périodes dans le système solaire. *Astronomy Astrophys.* 30, 141–154.
- Brouwer, D., van Woerkom, A.J.J., 1950. The secular variations of the orbital elements of the principal planets. *Astronomical Pap. Prep. Use Am. Ephemer. Naut. Alm.* 13 (2), 81–107.
- Brüggenmann, W., 1992. A minimal cost function method for optimizing the age-depth relation of deep-sea sediment cores. *Paleoceanography* 7, 467–487. <https://doi.org/10.1029/92PA01235>.
- Burgess, S.D., Muirhead, J.D., Bowring, S.A., 2017. Initial pulse of Siberian Traps sills as the trigger of the end-Permian mass extinction. *Nat. Commun.* 8, 164. <https://doi.org/10.1038/s41467-017-00083-9>.
- Burgess, S.D., Bowring, S.A., 2015. High-precision geochronology confirms voluminous magmatism before, during, and after Earth's most severe extinction. *Sci. Adv.* 1 (7) <https://doi.org/10.1126/sciadv.1500470> e1500470 1–14.
- Burgess, S.D., Bowring, S.A., Shen, S.Z., 2014. A new high-precision timeline for Earth's most severe extinction. *Proc. Natl. Acad. Sci.* 111, 3316–3321. <https://doi.org/10.1073/pnas.1317692111>.
- Calner, M., 2008. Silurian global events—at the tipping point of climate change. In: Elewa, A.M.T. (Ed.), *Mass Extinctions*. Springer-Verlag, Berlin, pp. 21–58.
- Carvajal, C.P., Soreghan, G.S., Isaacson, P.E., Ma, C., Hamilton, M.A., Hinnoy, L.A., Dulin, S.A., 2018. Atmospheric dust from the Pennsylvanian Copacabana Formation (Bolivia): a high-resolution record of paleoclimate and volcanism from northwestern Gondwana. *Gondwana Res.* 58, 105–121. <https://doi.org/10.1016/j.gr.2018.02.007>.
- Crick, R.E., Ellwood, B.B., Hladil, J., El Hassani, A., Hroudá, F., Chlubac, I., 2001. Magnetostratigraphy susceptibility of the pridolian-lochkovian (Silurian-Devonian) GSSP (Klonk, Czech Republic) and a coeval sequence in anti-atlas Morocco. *Palaeogeogr. Palaeoclimatol. Palaeoecol.* 167, 73–100. [https://doi.org/10.1016/S0031-0182\(00\)00233-9](https://doi.org/10.1016/S0031-0182(00)00233-9).

- Crucifix, M., 2016. Palinsol: Insolation for Palaeoclimate Studies, R Package. <https://CRAN.R-project.org/package=palinsol>.
- Croudace, I.W., Rothwell, R.G., 2015. Micro-XRF Studies of Sediment Cores, Developments in Paleoenvironmental Research, vol. 17. Springer, Dordrecht. <https://doi.org/10.1007/978-94-017-9849-5>, 656 p.
- Da Silva, A.C., Hladil, J., Chadimova, L., Slavik, L., Hilgen, F.J., Babek, O., Dekkers, M.J., 2016. Refining the early devonian time scale using Milankovitch cyclicity in lochkovian–pragian sediments (prague Synform, Czech Republic). *Earth Planet. Sci. Lett.* 455, 125–139. <https://doi.org/10.1016/j.epsl.2016.09.009>.
- Dabard, M.P., Loi, A., Paris, F., Ghienne, J.F., Pistis, M., Vidal, M., 2015. Sea-level curve for the middle to early late ordovician in the armorican massif (western France): icehouse third-order glacio-eustatic cycles. *Palaeogeogr. Palaeoclimatol. Palaeoecol.* 436, 96–111. <https://doi.org/10.1016/j.palaeo.2015.06.038>.
- Davydov, V.I., Crowley, J.L., Schmitz, M.D., Poletaev, V.I., 2010. High-precision U-Pb zircon age calibration of the global Carboniferous time scale and Milankovitch band cyclicity in the Donets Basin, eastern Ukraine. *G-cubed* 11, Q0AA04. <https://doi.org/10.1029/2009GC002736>.
- Dehant, V., Mathews, P.M., 2015. *Precession, Nutation and Wobble of the Earth*. Cambridge University Press, Cambridge, 536 p.
- Dehant, V., Capitaine, N., 1997. On the precession constant: values and constraints on the dynamical ellipticity; link with Oppolzer terms and tilt-over-mode. *Celest. Mech. Dyn. Astronomy* 65, 439–458. <https://doi.org/10.1007/BF00049506>.
- Desrochers, A., Farley, C., Achab, A., Asselin, E., Riva, J.F., 2010. A far-field record of the end ordovician glaciation: the Ellis Bay formation, Anticosti Island, eastern Canada. *Palaeogeogr. Palaeoclimatol. Palaeoecol.* 296, 248–263. <https://doi.org/10.1016/j.palaeo.2010.02.017>.
- Deubner, F.-L., 1990. Discussion on Late Precambrian tidal rhythmites in South Australia and the history of the Earth's rotation. *J. Geol. Soc. London* 147, 1083–1084.
- De Vleeschouwer, D., Da Silva, A.C., Sinnesael, M., Chen, D., Day, J.E., Whalen, M.T., Guo, Z., Claeys, P., 2017b. Timing and pacing of the Late Devonian mass extinction event regulated by eccentricity and obliquity. *Nat. Commun.* 8, 2268. <https://doi.org/10.1038/s41467-017-02407-1>.
- De Vleeschouwer, D., Vahlencamp, M., Crucifix, M., Paëlike, H., 2017a. Alternating Southern and Northern Hemisphere climate response to astronomical forcing during the past 35 m.y. *Geology* 45 (4), 375–378. <https://doi.org/10.1130/G38663.1>.
- De Vleeschouwer, D., Boulvain, F., Da Silva, A.-C., Pas, D., Labaye, C., Claeys, P., 2015. The astronomical calibration of the givetian (middle devonian) timescale (dinant Synclinorium, Belgium). In: Da Silva, A.C., Whalen, M.T., Hladil, J., Chadimova, L., Chen, D., Spassov, S., Boulvain, F., Devleeschouwer, X. (Eds.), *Magnetic Susceptibility Application: A Window onto Ancient Environments and Climatic Variations*, vol. 414. Geological Society, London, pp. 245–256. <https://doi.org/10.1144/SP414.3>. Special Publications.
- De Vleeschouwer, D., Crucifix, M., Bounceur, N., Claeys, P., 2014. The impact of astronomical forcing on the Late Devonian greenhouse climate. *Glob. Planet. Change* 120, 65–80. <https://doi.org/10.1016/j.gloplacha.2014.06.002>.
- De Vleeschouwer, D., Whalen, M.T., Day, J.E.J., Claeys, P., 2012. Cyclostratigraphic calibration of the Frasnian (Late Devonian) time scale (western Alberta, Canada). *Geological Society of America Bulletin* 124 (5/6), 928–942. <https://doi.org/10.1130/B30547.1>.

- Denis, C., Schreider, A.A., Varga, P., Zavoti, J., 2002. Despinning of the earth rotation in the geological past and geomagnetic paleointensities. *J. Geodyn.* 34, 667–685. [https://doi.org/10.1016/S0264-3707\(02\)00049-2](https://doi.org/10.1016/S0264-3707(02)00049-2).
- De Surgy, N.O., Laskar, J., 1997. On the long term evolution of the spin of the Earth. *Astronomy Astrophys.* 318, 975–989.
- Derby, J., Fritz, R., Longacre, S., Morgan, W., Sternbach, W., 2012. The great american carbonate bank: the geology and economic Resources of the cambrian-ordovician Sauk megasequence of laurentia. *AAPG Memo.* 98, 528 p.
- Dickey, J.O., Bender, P.L., Faller, J.E., Newhall, X.X., Ricklefs, R.L., Ries, J.G., Shelus, P.J., Veillet, C., Whipple, A.L., Wiant, J.R., Williams, J.G., Yoder, C.F., 1994. Lunar laser ranging: a continuing legacy of the Apollo Program. *Science* 265, 482–490. <https://doi.org/10.1126/science.265.5171.482>.
- Dinarès-Thurell, J., Westerhold, T., Pujalte, V., Röhl, U., Kroon, D., 2014. Astronomical calibration of the danian stage (early Paleocene) revisited: Settling chronologies of sedimentary records across the atlantic and Pacific oceans. *Earth Planet. Sci. Lett.* 405, 119–131. <https://doi.org/10.1016/j.epsl.2014.08.027>.
- Dinarès-Turell, J., Pujalte, V., Stoykova, K., Elorza, J., 2013. Detailed correlation and astronomical forcing within the Upper Maastrichtian succession in the Basque Basin. *Bol. Geol. y Min.* 124 (2), 253–282.
- Eldrett, J.S., Ma, C., Bergman, S.C., Lutz, B., Gregory, F.J., Dodsworth, P., Phipps, M., Hardas, P., Minisini, D., Ozkan, A., Ramezani, J., Bowring, S., Kamo, S.L., Ferguson, K., Macalulay, C., Kelly, A.E., 2015. An astronomically calibrated stratigraphy of the cenomanian, turonian and earliest coniacian from the cretaceous western interior Seaway, USA: implications for global chronostratigraphy. *Cretac. Res.* 56, 316–344. <https://doi.org/10.1016/j.cretres.2015.04.010>.
- Ellwood, B.B., El Hassani, A., Tomkin, J.H., Bultynck, P., 2015. A climate-driven model using time-series analysis of magnetic susceptibility ( $\chi$ ) datasets to represent a floating-point high-resolution geological timescale for the Middle Devonian Eifelian stage. In: Da Silva, A.C., Whalen, M.T., Chadimova, J., Chen, D., Spassov, S., Boulvain, F., Devleeschouwer, X. (Eds.), *Magnetic Susceptibility Application: A Window onto Ancient Environments and Climatic Variations*, vol. 414. Geological Society, London, pp. 209–223. <https://doi.org/10.1144/SP414.4>. Special Publications.
- Ellwood, B.B., Brett, C.E., Tomkin, J.H., Macdonald, W.D., 2013. Visual identification and quantification of Milankovitch climate cycles in outcrop: an example from the upper ordovician Kope Formation, northern Kentucky. In: Jovane, L., Herreiro-Bervara, E., Hinnov, L.A., Housen, B.A. (Eds.), *Magnetic Methods and the Timing of Geological Processes*, vol. 373. Geological Society, London, pp. 341–353. <https://doi.org/10.1144/SP373.2>. Special Publications.
- Elrick, M., Reardon, D., Labor, W., Martin, J., Desrochers, A., Pope, M., 2013. Orbital-scale climate change and glacioeustasy during the early Late Ordovician (pre-Hirnantian) determined from  $\delta^{18}\text{O}$  values in marine apatite. *Geology* 41, 775–788. <https://doi.org/10.1130/G34363.1>.
- Edvardsson, S., Karlsson, K.G., Englholm, M., 2002. Accurate spin axes and solar system dynamics: climatic variations for the Earth and Mars. *Astronomy Astrophys.* 384, 689–701. <https://doi.org/10.1051/0004-6361:20020029>.
- Eros, J.M., Montanez, I.P., Osleger, D.A., Davydov, V.I., Nemyrovska, T.I., Poletaev, V.I., Zhykalyak, M.V., 2012. Sequence stratigraphy and onlap history of the Donets Basin, Ukraine: insight into Carboniferous icehouse dynamics. *Palaeogeogr. Palaeoclimatol. Palaeoecol.* 313–314, 1–25. <https://doi.org/10.1016/j.palaeo.2011.08.019>.

- Fang, Q., Wu, H., Wang, X., Yang, T., Li, H., Zhang, S., 2018. Astronomical cycles in the Serpukhovian-Moscovian (Carboniferous) marine sequence, South China and their implications for geochronology and icehouse dynamics. *J. Asian Earth Sci.* 156, 302–315. <https://doi.org/10.1016/j.jseas.2018.02.001>.
- Fang, Q., Wu, H.C., Hinnov, L.A., Jing, X.C., Wang, X.L., Yang, T.S., Li, H.Y., Zhang, S.H., 2017. Astronomical cycles of Middle Permian Maokou Formation in South China and their implications for sequence stratigraphy and paleoclimate. *Palaeogeogr. Palaeoclimatol. Palaeoecol.* 474, 130–139. <https://doi.org/10.1016/j.palaeo.2016.07.037>.
- Fang, Q., Wu, H., Hinnov, L.A., Wang, X., Yang, T., Li, H., Zhang, S., 2016. A record of astronomically forced climate change in a late Ordovician (Sandbian) deep marine sequence, Ordos Basin, North China. *Sediment. Geol.* 341, 163–174. <https://doi.org/10.1016/j.sedgeo.2016.06.002>.
- Fang, Q., Wu, H., Hinnov, L.A., Jing, X., Wang, X., Jiang, Q., 2015. Geological evidence for the chaotic behavior of the planets and its constraints on the third order eustatic sequences at the end of the Late Paleozoic Ice Age. *Palaeogeogr. Palaeoclimatol. Palaeoecol.* 440, 848–859. <https://doi.org/10.1016/j.palaeo.2015.10.014>.
- Feng, Z.Z., Yang, Y.Q., Bao, Y.Q., Yu, Z.D., Jing, Z.K., 1998. Carboniferous Lithofacies Paleogeography in South China. Geological Press, Beijing, pp. 1–119 (in Chinese with English abstract).
- Fiet, N., Gorin, G., 2000. Lithologic expression of Milankovitch cyclicity in carbonate-dominated, pelagic, Barremian deposits in central Italy. *Cretac. Res.* 21, 457–467. <https://doi.org/10.1006/cres.2000.0220>.
- Fielding, C.R., Frank, T.D., Birgenheier, L.P., Rygel, M.C., Jones, A.T., Roberts, J., 2008. Stratigraphic imprint of the Late Palaeozoic Ice Age in eastern Australia: a record of alternating glacial and nonglacial climate regime. *J. Geol. Soc.* 165, 129–140.
- Fischer, A.G., Herbert, T.D., Napoleone, G., Premoli Silva, I., Ripepe, M., 1991. Albian pelagic rhythms (Piobbico core). *J. Sediment. Petrol.* 61 (7), 1164–1172. <https://doi.org/10.1306/D426785C-2B26-11D7-8648000102C1865D>.
- Fischer, A.G., 1986. Climatic rhythms recorded in strata. *Annu. Rev. Earth Planet. Sci.* 14, 351–376. <https://doi.org/10.1146/annurev.ea.14.050186.002031>.
- Fischer, A.G., De Boer, P.L., Premoli Silva, I., 1988. Cyclostratigraphy. In: Beaudoin, B., Ginsburg, R.N. (Eds.), *Global Sedimentary Geology Program: Cretaceous Resources, Events, and Rhythms*. — NATO ASI Series. Kluwer, Dordrecht, pp. 139–172.
- Gambacorta, G., Menichetti, E., Trincianti, E., Torricelli, S., 2018. Orbital control on cyclical primary productivity and benthic anoxia: astronomical tuning of the Telychian Stage (Early Silurian). *Palaeogeogr. Palaeoclimatol. Palaeoecol.* 495, 152–162. <https://doi.org/10.1016/j.palaeo.2018.01.003>.
- Goldhammer, R.K., Lehmann, P.J., Dunn, P.A., 1993. The origin of high-frequency platform carbonate cycles and third order sequences (Lower Ordovician El Paso Group, west Texas): constraints from outcrop data and stratigraphic modeling. *J. Sediment. Petrol.* 63, 318–359. <https://doi.org/10.1306/D4267AFA-2B26-11D7-8648000102C1865D>.
- Gong, Y., Droser, M.L., 2001. Periodic anoxic shelf in the Early-Middle Ordovician transition: ichnosedimentologic evidence from west-central Utah, USA. *Sci. China, Ser. D* 44, 979–989. <https://doi.org/10.1007/BF02875391>.
- Gong, Z., Kodama, K.P., Li, Y.-X., 2017. Rock magnetic cyclostratigraphy of the Doušantuo Formation, South China and its implications for the duration of the Shuram carbon isotope excursion. *Precambrian Res.* 289, 62–74. <https://doi.org/10.1016/j.precamres.2016.12.002>.

- Grader, G.W., Issacson, P.E., Díaz-Martínez, E., Pope, M.C., 2008. Pennsylvanian and permian sequences in Bolivia: direct responses to Gondwana glaciation. In: Fielding, C.R., Frank, T.D., Isbell, J.L. (Eds.), Resolving the Late Paleozoic Ice Age in Time and Space, vol. 441, pp. 143–159. [https://doi.org/10.1130/2008.2441\(10\).GeologicalSocietyofAmericaSpecialPaper](https://doi.org/10.1130/2008.2441(10).GeologicalSocietyofAmericaSpecialPaper).
- Green, J.A.M., Huber, M., Waltham, D., Buzan, J., Wells, M., 2017. Explicitly modelled deep-time tidal dissipation and its implication for Lunar history. *Earth Planet. Sci. Lett.* 461, 46–53. <https://doi.org/10.1016/j.epsl.2016.12.038>.
- Green, J.A.M., Huber, M., 2013. Tidal dissipation in the early Eocene and implications for ocean mixing. *Geophys. Res. Lett.* 40, 2707–2713. <https://doi.org/10.1002/grl.50510>.
- Grippo, A., Fischer, A.G., Hinnov, L.A., Herbert, T.D., Premoli Silva, I., 2004. Cyclostratigraphy and chronology of the Albian stage (Piobbico core, Italy). In: D'Argenio, B., Fischer, A.G., Premoli Silva, I., Weissert, H., Ferreri, V. (Eds.), Cyclostratigraphy: Approaches and Case Histories, pp. 57–81. <https://doi.org/10.2110/pec.04.81.0057>. SEPM Special Publication No. 81.
- Grotzinger, J.P., 1986. Cyclicity and paleoenvironmental dynamics, Rocknest platform, northwest Canada. *Geol. Soc. Am. Bull.* 97, 1208–1231. [https://doi.org/10.1130/0016-7606\(1986\)97<1208:CAPDRP>2.0.CO;2](https://doi.org/10.1130/0016-7606(1986)97<1208:CAPDRP>2.0.CO;2).
- Grotzinger, J.P., Fike, D.A., Fischer, W.W., 2011. Enigmatic origin of the largest-known carbon isotope excursion in Earth's history. *Nat. Geosci.* 4, 285–292. <https://doi.org/10.1038/ngeo1138>.
- Hays, J.D., Imbrie, J., Shackleton, N.J., 1976. Variations in the Earth's orbit: pacemaker of the ice ages. *Science* 194 (4270), 1121–1132. <https://doi.org/10.1126/science.194.4270.1121>.
- Hennebert, M., 2014. The Cretaceous-Paleogene boundary and its 405-kyr eccentricity cycle phase: a new constraint on radiometric dating and astrochronology. *Carnets Géologique* 14 (9), 173–189. <https://doi.org/10.1029/2012GC004096>.
- Herbert, T.D., 1999. Toward a composite orbital chronology for the late Cretaceous and early Paleocene GPTS. *Phil. Trans. R. Soc. Lond.* 357, 1891–1905. <https://doi.org/10.1098/rsta.1999.0406>.
- Herbert, T.D., Stallard, R.F., Fischer, A.G., 1986. Anoxic events, productivity rhythms and the orbital signature in a mid-Cretaceous deep-sea sequence from Central Italy. *Paleceanography* 1, 495–506. <https://doi.org/10.1029/PA001i004p00495>.
- Herterich, K., Sarnthein, M., 1984. Brunhes time scale: tuning by rates of calcium-carbonate dissolution and cross spectral analyses with solar insolation. In: Berger, A., Imbrie, J., Hays, J., Kukla, G., Salzman, B. (Eds.), *Milankovitch and Climate, Part I*, D. Reidel Publishing Company, Dordrecht, pp. 447–466.
- Hilgen, F.J., 2010. Astronomical tuning in the 19th century. *Earth Sci. Rev.* 98, 65–80. <https://doi.org/10.1016/j.earscirev.2009.10.004>.
- Hilgen, F.J., Abels, H.A., Kuiper, K.F., Lourens, L.J., Wolthers, M., 2015. Towards a stable astronomical time scale for the Paleocene: aligning Shatsky rise with the Zumaia – Walvis Ridge ODP site 1262 composite. *Newslett. Stratigr.* 48 (1), 91–110. <https://doi.org/10.1127/nos/2014/0054>.
- Hilgen, F.J., Hinnov, L.A., Abdul Aziz, H., Abels, H.A., de Boer, B., Bosmans, J.H.C., Hüsing, S.K., Kuiper, K., Lourens, L.J., Tuenter, E., Van de Val, R.S.W., Zeeden, C., 2014. Stratigraphic continuity and fragmentary sedimentation: the success of cyclostratigraphy as part of integrated stratigraphy. Special Publication. In: *Strata and Time: Probing the Gaps in Our Understanding*, vol. 404. Geological Society of London. <https://doi.org/10.1144/SP404.12>.
- Hilgen, F.J., Lourens, L.J., Van Dam, J.A., 2012. The Neogene period. In: Gradstein, F.M., Ogg, J.G., Schmitz, M., Ogg, G. (Eds.), *The Geologic Time Scale 2012*. Elsevier, pp. 923–978. <https://doi.org/10.1016/B978-0-444-59425-9.00029-9> (Chapter 29).

- Hilgen, F.J., Kuiper, K.F., Lourens, L.J., 2010. Evaluation of the astronomical time scale for the Paleocene and earliest Eocene. *Earth Planet. Sci. Lett.* 300, 139–151. <https://doi.org/10.1016/j.epsl.2010.09.044>.
- Hilgen, F.J., Abdul Aziz, H., Krijgsman, W., Langereis, C.G., Lourens, L.J., Meulenkamp, J.E., Riffi, I., Steenbrink, J., Turco, E., van Vugt, N., Wijbrans, J.R., Zachariasse, W.J., 1999. Present status of the astronomical (polarity) time-scale for the Mediterranean Late Neogene. *Phil. Trans. R. Soc. Lond. Ser. A* 357, 1931–1947. <https://doi.org/10.1098/rsta.1999.0408>.
- Hilgen, F.J., Lourens, L.J., Berger, A., Loutre, M.F., 1993. Evaluation of the astronomical lay liberated time scale for the late Pliocene and earliest Pleistocene. *Paleoceanography* 8, 549–565. <https://doi.org/10.1029/93PA01248>.
- Hinnov, L.A., 2018. Astronomical metronome of geological consequence. *Proc. Natl. Acad. Sci.* 115 (24), 6104–6106. <https://doi.org/10.1073/pnas.1807020115>.
- Hinnov, L.A., 2013. Cyclostratigraphy and its revolutionizing applications in the earth and planetary Sciences. *Geol. Soc. Am. Bull.* 125, 1703–1734. <https://doi.org/10.1130/B30934.1>.
- Hinnov, L.A., Diecchio, R.J., 2015. Milankovitch cycles in the Juniata Formation, late ordovician central appalachian basin, USA. *Stratigraphy* 12, 287–296.
- Hinnov, L.A., Mei, M., Wu, H., Zhang, S., 2015. The Precambrian Wumishan cyclothem of China: 60+ million year long shallow marine carbonate record of multiple-scale, hierarchical sea level oscillations, an aragonite-calcite sea transition and cyanobacteria calcification. *Geol. Soc. Am. Annual Meet. Abstr. Programs* 47 (7), 649. Baltimore, Maryland, USA 1–4 November.
- Hinnov, L.A., Locklair, R., Ogg, J., 2008. Recent developments in the geologic timescale, construction of the astronomical time scale—Part 1. In: Early Cretaceous, Abstract, 33nd International Geological Congress, Oslo, Norway, 6–14 August.
- Hofmann, A., Dirks, P.H.G.M., Jelsma, H.A., 2004. Shallowing upward carbonate cycles in the Belingwe Greenstone Belt, Zimbabwe: a record of Archean sealevel oscillations. *J. Sediment. Res.* 4, 64–81. <https://doi.org/10.1306/052903740064>.
- Hüsing, S., Benist, A., van der Boon, A., Abels, H.A., Deenen, M.H.L., Ruhl, M., Krijgsman, W., 2014. Astronomically-calibrated magnetostratigraphy of the lower jurassic marine successions at St. Audrie's Bay and East Quantoxhead (Hettangian–Sinemurian; Somerset, UK). *Palaeogeogr. Palaeoclimatol. Palaeoecol.* 403, 43–56. <https://doi.org/10.1016/j.palaeo.2014.03.022>.
- Huang, C., 2018. Astronomical time scale for the Mesozoic (this volume). *Stratigr. Time-scales 3 (Chapter 4)*.
- Huang, C., Hinnov, L.A., Fischer, A.G., Grippo, A., Herbert, T., 2010a. Astronomical tuning of the Aptian stage from Italian reference sections. *Geology* 38, 899–903. <https://doi.org/10.1130/G31177.1>.
- Huang, C., Hinnov, L.A., Swientek, O., Smelnor, M., 2010b. Astronomical tuning of late jurassic–early cretaceous sediments (Volgian–Ryazanian stages), Greenland-Norwegian Seaway, abstract. In: AAPG Annual Convention, New Orleans, LA, 11–14 April.
- Huang, C., Hesselbo, S.P., Hinnov, L.A., 2010c. Astrochronology of the late jurassic Kimmeridge Clay (Dorset, England) and implications for earth system processes. *Earth Planet. Sci. Lett.* 289, 242–255. <https://doi.org/10.1016/j.epsl.2009.11.013>.
- Huret, E., Hinnov, L.A., Galbrun, B., Boulila, S., Collin, P.-Y., 2008a. High-resolution cyclostratigraphy of Upper Jurassic (Callovian to Oxfordian) marly formations (Paris Basin): astronomical calibration and implications for regional correlation, Abstract. In: 33rd International Geological Congress, Oslo, Norway, 6–14 August.
- Huret, E., Hinnov, L.A., Galbrun, B., Collin, P.-Y., Gardin, S., Rouget, I., 2008b. Astronomical calibration and correlation of the lower jurassic, paris and lombard basins (tethys), abstract. In: 33rd International Geological Congress, Oslo, Norway, 6–14 August.

- Husson, D., Galbrun, B., Laskar, J., Hinnov, L.A., Thibault, N., Gardin, S., Locklair, R.E., 2011a. Astronomical calibration of the maastrichtian (late cretaceous). *Earth Planet. Sci. Lett.* 305, 328–340. <https://doi.org/10.1016/j.epsl.2011.03.008>.
- Huybers, P., 2007. Glacial variability over the last two million years: an extended depth-derived age model, continuous obliquity pacing, and the Pleistocene progression. *Quat. Sci. Rev.* 26, 37–55. <https://doi.org/10.1016/j.quascirev.2006.07.013>.
- Huybers, P., 2006. Early Pleistocene glacial cycles and the integrated summer insolation forcing. *Science* 313, 508–511. <https://doi.org/10.1126/science.1125249>.
- Huybers, P., Wunsch, C., 2004. A depth-derived Pleistocene age model: uncertainty estimates, sedimentation variability, and nonlinear climate change. *Paleoceanography* 19, PA1028. <https://doi.org/10.1029/2002PA000857>.
- Ikeda, M., Tada, R., Ozaki, K., 2017. Astronomical pacing of the global silica cycle recorded in Mesozoic bedded cherts. *Nat. Commun.* 8, 15532. <https://doi.org/10.1038/ncomms15532>.
- Ikeda, M., Tada, R., 2014. A 70 million year astronomical time scale for the deep-sea bedded chert sequence (Inuyama, Japan): implications for Triassic-Jurassic geochronology. *Earth Planet. Sci. Lett.* 399, 30–43. <https://doi.org/10.1016/j.epsl.2014.04.031>.
- Ikeda, M., Tada, R., 2013. Long period astronomical cycles from the Triassic to Jurassic bedded chert sequence (Inuyama, Japan); Geologic evidences for the chaotic behavior of solar planets. *Earth Planets Space* 65, 351–360. <https://doi.org/10.5047/eps.2012.09.004>.
- Ikeda, M., Tada, R., Sakuma, H., 2010. Astronomical cycle origin of bedded chert; middle Triassic bedded chert sequence, Inuyama, Japan. *Earth Planet. Sci. Lett.* 297, 369–378. <https://doi.org/10.1016/j.epsl.2010.06.027>.
- Imbrie, J., Hays, J.D., Martinson, D.G., McIntyre, A., Mix, A.C., Morley, J.C., Pisias, N.G., Prell, W.L., Shackleton, N.J., 1984. The orbital theory of Pleistocene climate: support from a revised chronology of the marine  $\delta^{18}\text{O}$  record. In: Berger, A., Imbrie, J., Hays, J., Kukla, G., Salzman, B. (Eds.), *Milankovitch and Climate, Part I*. D. Reidel Publishing Company, Dordrecht, pp. 269–305.
- Imbrie, J., Imbrie, J.Z., 1980. Modeling the climatic response to orbital variations. *Science* 207, 943–953. <https://doi.org/10.1126/science.207.4434.943>.
- Isaacson, P.E., Diaz-Martinez, E., Grader, G.W., Kalvoda, J., Babek, O., Devuyst, F.X., 2008. Late Devonian–earliest Mississippian glaciation in Gondwanaland and its biogeographic consequences. *Palaeogeogr. Palaeoclimatol. Palaeoecol.* 268 (3–4), 126–142. <https://doi.org/10.1016/j.palaeo.2008.03.047>.
- Ito, T., Tanikawa, K., 2007. Trends in 20th Century Celestial Mechanics, vol. 9. *Publications of the National Astronomy Observatory of Japan*, pp. 55–112.
- Kietzmann, D.A., Palma, R.M., Iglesia Llanos, M.P., 2015. Cyclostratigraphy of an orbitally-driven tithonian–valanginian carbonate ramp succession, southern mendoza, Argentina: implications for the jurassic–cretaceous boundary in the Neuquén basin. *Sediment. Geol.* 315, 29–46. <https://doi.org/10.1016/j.sedgeo.2014.10.002>.
- Kent, D.V., Olsen, P.E., Rasmussen, C., Lepre, C., Mundil, R., Irmis, R., Gehrels, G., Giesler, D., Geissman, J., Parker, W., 2018. Empirical evidence for stability of the 405 kyr Jupiter-Venus eccentricity cycle over hundreds of millions of years. *Proc. Natl. Acad. Sci. USA*. <https://doi.org/10.1073/pnas.1800891115>.
- Kent, D.V., Olsen, P.E., Muttoni, G., 2017. Astrochronostigraphic polarity time scale (APTS) for the Late Triassic and Early Jurassic from continental sediments and correlation with standard marine stages. *Earth Sci. Rev.* 166, 153–180. <https://doi.org/10.1016/j.earscirev.2016.12.014>.
- Kent, D.V., Olsen, P.E., Witte, W.K., 1995. Late Triassic–earliest Jurassic geomagnetic polarity sequence and paleolatitudes from drill cores in the Newark rift basin, eastern North America. *J. Geophys. Res.* 100, 14965–14998. <https://doi.org/10.1029/95JB01054>.

- Kim, J.C., Lee, Y.I., 1998. Cyclostratigraphy of the lower ordovician Dumugol Formation, Korea: meter-scale cyclicity and sequence stratigraphic interpretation. *Geosci. J.* 2, 134–147. <https://doi.org/10.1007/BF02910257>.
- Klein, C., 2005. Some Precambrian banded iron-formations (BIFs) from around the world: their age, geologic setting, mineralogy, metamorphism, geochemistry, and origin. *Am. Mineral.* 90, 1473–1499. <https://doi.org/10.2138/am.2005.1871>.
- Kodama, K.P., Hinnov, L.A., 2015. Rock Magnetic Cyclostratigraphy. John Wiley and Sons, Chichester, UK. <https://doi.org/10.1002/9781118561294>, 164 p.
- Kodama, K.P., Anastasio, D.J., Pares, J., Hinnov, L.A., 2010. High-resolution rock magnetic cyclostratigraphy in an Eocene flysch, Spanish Pyrenees. *G-cubed* 11, Q0AA07. <https://doi.org/10.1029/2010GC003069>.
- Kominz, M.A., Beavan, J., Bond, G.C., McManus, J., 1991. Are cyclic sediments periodic? Gamma analysis and spectral analysis of Newark Supergroup lacustrine strata. *Kansas Geological Survey Bulletin* 233, 320–334.
- Kominz, M.A., Bond, G.C., 1990. A new method of testing periodicity in cyclic sediment: application to the Newark Supergroup. *Earth Planet. Sci. Lett.* 98, 233–244.
- Kominz, M.A., Heath, G.R., Ku, T.-L., Pisias, N.G., 1979. Brunhes time scales and the interpretation of climatic change. *Earth Planet. Sci. Lett.* 45, 394–410.
- Kostadinov, T.S., Gilb, R., 2014. Earth Orbit v2.1: a 3-D visualization and analysis model of Earth's orbit, Milankovitch cycles and insolation. *Geosci. Model Dev.* 7, 1051–2014. <https://doi.org/10.5194/gmd-7-1051-2014>.
- Kotov, S., Pálike, H., 2017. MyDTW – dynamic Time Warping program for stratigraphical time series. In: 19th EGU General Assembly, EGU2017, 23–28 April, 2017, Vienna, Austria., 2157.
- Kuiper, K.F., Deino, A., Hilgen, F.J., Krijgsman, W., Renne, P.R., Wijbrans, J.R., 2008. Synchronizing rock clocks of Earth history. *Science* 320, 500–504. <https://doi.org/10.1126/science.1154339>.
- Lambeck, K., 1980. *The Earth's Variable Rotation: Geophysical Causes and Consequences*. Cambridge University Press, New York, 449 p.
- Laskar, J., 2015. Stability of the Solar System. [http://www.scholarpedia.org/article/Stability\\_of\\_the\\_solar\\_system](http://www.scholarpedia.org/article/Stability_of_the_solar_system).
- Laskar, J., 2013. Is the solar system stable? *Progr. Math. Phys.* 66, 239–270.
- Laskar, J., 1993. The stability of the solar system. In: Pfenniger, D. (Ed.), *Ergodic Concepts and Stellar Dynamics*, Lecture Notes in Physics.
- Laskar, J., 1990. The chaotic motion of the Solar System: a numerical estimate of the size of the chaotic zones. *Icarus* 88, 266–291. [https://doi.org/10.1016/0019-1035\(90\)90084-M](https://doi.org/10.1016/0019-1035(90)90084-M).
- Laskar, J., 1989. A numerical experiment on the chaotic behavior of the Solar System. *Nature* 338, 237–238. <https://doi.org/10.1038/338237a0>.
- Laskar, J., Farrés, A., Gastineau, M., 2012. Stability of the long period terms in the La2011 astronomical solution. *Geophys. Res. Abstr.* 14. EGU2012-E2481.
- Laskar, J., Gastineau, M., Delisle, J.-B., Farrés, A., Fienga, A., 2011b. Strong chaos induced by close encounters with Ceres and Vesta. *Astronomy Astrophys.* 532, L4.
- Laskar, J., Fienga, A., Gastineau, M., Manche, H., 2011a. La2010: a new orbital solution for the long term motion of the Earth. *Astronomy Astrophys.* 532, A89. <https://doi.org/10.1051/0004-6361/201116836>.
- Laskar, J., Robutel, P., Joutel, J., Gastineau, M., Correia, A.C.M., Levrard, B., 2004. A numerical solution for the insolation quantities of the Earth. *Astronomy Astrophys.* 428, 261–285. <https://doi.org/10.1051/0004-6361:20041335>.
- Laskar, J., Joutel, J., Boudin, F., 1993. Orbital, precessional and insolation quantities for the Earth from -20 Myr to +10 Myr. *Astronomy Astrophys.* 270, 522–533.

- Le Hir, G., Donnadieu, Y., Goddérès, Y., Meyer-Berthaud, B., Ramstein, G., Blakey, R.C., 2011. The climate change caused by the land plant invasion in the Devonian. *Earth Planet. Sci. Lett.* 310 (3–4), 203–212. <https://doi.org/10.1016/j.epsl.2011.08.042>.
- Le Verrier, U.J., 1855. *Recherches astronomiques. Annales Observatoire Impérial de Paris* 1, 73–383.
- Li, M., Kump, L.R., Hinnov, L.A., Mann, M.E., 2018b. Tracking variable sedimentation rates and astronomical forcing in Phanerozoic paleoclimate proxy series with evolutionary correlation coefficients and hypothesis testing. *Earth Planet. Sci. Lett.* (in press).
- Li, M., Huang, C., Hinnov, L.A., Chen, W., Ogg, J.G., Tian, W., 2018a. Astrochronology of the anisian stage (middle triassic) at the Guandao reference section, south China. *Earth Planet. Sci. Lett.* 482, 591–606. <https://doi.org/10.1016/j.epsl.2017.11.042>.
- Li, M., Huang, C., Hinnov, L.A., Ogg, J., Chen, Z.-Q., Zhang, Y., 2016. Obliquity-forced climate during the early triassic hothouse in China. *Geology* 44, 623–626. <https://doi.org/10.1130/G37970.1>.
- Lin, L., Khider, D., Lisiecki, L.E., Lawrence, C.E., 2014. Probabilistic sequence alignment of stratigraphic records. *Paleoceanography* 29, 976–989. <https://doi.org/10.1002/2014PA002713>.
- Lisiecki, L.E., Raymo, M.E., 2005. A Pliocene–Pleistocene stack of 57 globally distributed benthic  $\delta^{18}\text{O}$  records. *Paleoceanography* 20, PA1003. <https://doi.org/10.1029/2004PA001071>.
- Lisiecki, L.E., Lisiecki, P.A., 2002. Application of dynamic programming to the correlation of paleoclimate records. *Paleoceanography* 17 (4), 1049. <https://doi.org/10.1029/2001PA000733>.
- Liu, J.-C., Capitaine, N., 2017. Evaluation of a possible upgrade of the IAU2006 precession. *Astronomy Astrophys.* 597, A83. <https://doi.org/10.1051/0004-6361/201628717>.
- Liu, W., Wu, H., Hinnov, L.A., Ma, C., Li, M., Pas, D., 2017b. Paleoclimate evolution driven by astronomical forcing in the early cretaceous Songliao Basin, northeast China. In: *10th International Symposium on the Cretaceous, 21–26 August, Vienna, AT*.
- Liu, Z., Huang, C., Algeo, T.J., Liu, J., Hao, Y., Du, X., Lu, Y., Chen, P., Guo, L., Peng, L., 2017a. High-resolution astrochronological record for the paleocene-oligocene (66–23 Ma) from the rapidly subsiding Bohai Bay Basin, northeastern China. *Palaeogeogr. Palaeoclimatol. Palaeoecol.* <https://doi.org/10.1016/j.palaeo.2017.10.030>.
- Locklair, R.E., Sageman, B.B., 2008. Cyclostratigraphy of the Upper Cretaceous Niobara Formation, Western Interior, U.S.A.: A Coniacian-Santonian orbital timescale. *Earth Planet. Sci. Lett.* 269, 540–553. <https://doi.org/10.1016/j.epsl.2008.03.021>.
- Loi, A., Ghienne, J.-F., Dabard, M.P., Paris, F., Botquelen, A., Christ, N., Elouad-Debbaj, Z., Gorini, A., Vidal, M., Videt, B., Destombes, J., 2010. The Late Ordovician glacio-eustatic record from a high-latitude storm-dominated shelf succession: The Bou Ingarf section (Anti-Atlas, Southern Morocco). *Palaeogeogr. Palaeoclimatol. Palaeoecol.* 296, 332–358. <https://doi.org/10.1016/j.palaeo.2010.01.018>.
- Lorenz, H., 2010. The Swedish Deep Drilling Program: For Science and Society. *GFF-Uppsala* 132 (1), 25–27. <https://doi.org/10.1080/11035891003763354>.
- Lourens, L.J., Hilgen, F., Shackleton, N.J., Laskar, J., Wilson, D., 2004. The Neogene Period. In: Gradstein, F., Ogg, J., Smith, A. (Eds.), *A Geologic Time Scale 2004*. Cambridge University Press, Cambridge, UK, pp. 400–440.
- Lourens, L.J., Wehausen, R., Brumsack, H.J., 2001. Geological constraints on tidal dissipation and dynamical ellipticity of the Earth over the past three million years. *Nature* 409, 1029–1033. <https://doi.org/10.1038/35059062>.
- Lourens, L.J., Antonarakou, A., Hilgen, F.J., Van Hoof, A.A.M., Vergnaud-Grazzini, C., Zachariasse, W.J., 1996. Evaluation of the Plio-Pleistocene astronomical timescale. *Paleoceanography* 11 (4), 391–413. <https://doi.org/10.1029/96PA01125>.

- Loutre, M.-F., 2003. Ice Ages (Milankovitch Theory). In: Curry, J.A., Pyle, J.A. (Eds.), *Encyclopedia of Atmospheric Sciences*. Elsevier, pp. 995–1003.
- Loutre, M.-F., Dehant, V., Berger, A., 1990. Astronomical frequencies in paleoclimatic data and the dynamical ellipticity of the Earth. In: Brosche, P., Sündermann, J. (Eds.), *Earth's Rotation from Eons to Days*. Springer-Verlag, Berlin, pp. 188–200. [https://doi.org/10.1007/978-3-642-75587-3\\_20](https://doi.org/10.1007/978-3-642-75587-3_20).
- Lowrie, W., 2007. *Fundamentals of Geophysics*, second ed. Cambridge University Press, Cambridge. 381 p.
- Ma, C., Hinnov, L.A., Carvajal, C.P., Soreghan, G.L., 2018. Earth's Late Bashkirian Precessional Frequency from the Copacabana Formation, Bolivia, South America. *Nat. Geosci.* (in review).
- Ma, C., Meyers, S.R., Sageman, B.B., 2017. Theory of chaotic orbital variations confirmed by Cretaceous geological evidence. *Nature* 542, 468–470. <https://doi.org/10.1038/nature21402>.
- Malinverno, A., Erba, E., Herbert, T.D., 2010. Orbital tuning as an inverse problem: Chronology of the early Aptian oceanic anoxic event 1a (Sellia Level) in the Cismon APTICORE. *Paleoceanography* 25, PA2203. <https://doi.org/10.1029/2009PA001769>.
- Martinez, M., Deconinck, J.-F., Pellenard, P., Riquier, L., Company, M., Reboulet, S., Moiroud, M., 2015. Astrochronology of the Valanginian–Hauterivian stages (Early Cretaceous): Chronological relationships between the Paraná–Etendeka large igneous province and the Weissert and the Faraoni events. *Glob. Planet. Change* 131, 158–173. <https://doi.org/10.1016/j.gloplacha.2015.06.001>.
- Martinson, D.G., Menke, W., Stoffa, P., 1982. An inverse approach to signal correlation. *J. Geophys. Res.* 87, 4807–4818. <https://doi.org/10.1029/JB087iB06p04807>.
- Maurer, F., Hinnov, L.A., Schlager, W., 2004. Statistical time series analysis and sedimentological tuning of bedding rhythms in a Triassic basinal succession (S. Alps, Italy). In: D'Argenio, B., Fischer, A.G., Premoli Silva, I., Weissert, H., Ferreri, V. (Eds.), *Cyclostratigraphy: Approaches and Case Histories*, vol. 81. Society for Sedimentary Geology Special Publication, pp. 83–99. <https://doi.org/10.2110/pec.04.81.0083>.
- Mazzullo, S.J., 1971. Length of the year during the Silurian and Devonian Periods. *Geol. Soc. Am. Bull.* 82, 1085–1086.
- McGhee Jr., G.R., 2013. When the Invasion of Land Failed: The Legacy of the Devonian Extinctions. Columbia University Press, New York. <https://doi.org/10.7312/mcgh16056>, 317 p.
- Mclemore, Y. and Koonce, L., 2016. Precession, Rigid Body and Basic Concepts of Classical Mechanics, Academic Studio, New York: <http://ebooks.wtbooks.com/static/wtbooks/ebooks/9781280131134/9781280131134.pdf>. [http://www.thefullwiki.org/Axial\\_precession\\_\(astronomy\)](http://www.thefullwiki.org/Axial_precession_(astronomy)). [https://wikivisually.com/wiki/Axial\\_precession](https://wikivisually.com/wiki/Axial_precession).
- Meech, L.W., 1856. On the relative intensity of the heat and light of the Sun. *Smithson. Contribut. Knowl.* 9, 1–58.
- Mei, M., Tucker, M.E., 2013. Milankovitch-driven cycles in the Precambrian of China: The Wumishan Formation. *J. Palaeogeogr.* 2 (4), 369–389. <https://doi.org/10.3724/SP.J.1261.2013.00037>.
- Mei, M., Ma, Y., Zhou, H., Du, M., Luo, Z., Guo, Q., 2001. Fischer plots of Wumishan cyclothsems, Precambrian records of third-order sea-level changes. *J. China Univ. Geosci.* 12, 1–10.
- Meyers, S.R., 2015. The evaluation of eccentricity-related amplitude modulation and bundling in paleoclimate data: An inverse approach for astrochronologic testing and time scale optimization. *Paleoceanography* 30, 1625–1640. <https://doi.org/10.1002/2015PA002850>.
- Meyers, S.R., 2014. Astrochron: An R Package for Astrochronology. <https://cran.r-project.org/web/packages/astrochron/index.html>.

- Meyers, S.R., Malinverno, A., 2018. Proterozoic Milankovitch cycles and the history of the solar system. Proc. Natl. Acad. Sci. <https://doi.org/10.1073/pnas.1717689115>.
- Meyers, S.R., Sageman, B.B., 2007. Quantification of deep-time orbital forcing by average spectral misfit. Am. J. Sci. 307, 773–792. <https://doi.org/10.2475/05.2007.01>.
- Milankovitch, M., 1941. Kanon der Erdbestrahlung und seine Anwendung auf das Eiszeitenproblem. Royal Serbian Academy, Section of Mathematical and Natural Sciences, Belgrade, 633 p. (and 1998 reissue in English: Canon of Insolation and the Ice-Age Problem: Belgrade, Serbian Academy of Sciences and Arts, Section of Mathematical and Natural Sciences, 634 p.).
- Milankovitch, M., 1920. Théorie Mathématique des Phénomènes Thermiques Produits par la Radiation Solaire. Académie Yougoslave des Sciences et des Arts de Zagreb. Gauthier Villars, Paris, pp. 27–52.
- Miller, K.G., Baluyot, R., Wright, J.D., Kopp, R.E., Browning, J.V., 2017. Closing an early Miocene astronomical gap with Southern Ocean  $\delta^{18}\text{O}$  and  $\delta^{13}\text{C}$  records: Implications for sea level change. Paleoceanography 32, 600–621. <https://doi.org/10.1002/2016PA003074>.
- Minguez, D., Kodama, K.P., Hillhouse, J.W., 2015. Paleomagnetic and cyclostratigraphic constraints on the synchronicity and duration of the Shuram carbon isotope excursion, Johnnie Formation, Death Valley Region, CA. Precambrian Res. 266, 395–408. <https://doi.org/10.1016/j.precamres.2015.05.033>.
- Miskovitch, V.V., 1931. Variations séculaires des éléments astronomiques de l'orbite terrestre. Glas Srpske Kraljevske Akademije 143 (70). Première Classe, Belgrade.
- Morgans-Bell, H.S., Coe, A.L., Hesselbo, S.P., Jenkyns, H.C., Weedon, G.P., Marshall, J.E.A., Tyson, R.V., Williams, C.J., 2001. Integrated stratigraphy of the Kimmeridge Clay Formation (Upper Jurassic) based on exposures and boreholes in south Dorset, UK. Geol. Mag. 138 (5), 511–539. <https://doi.org/10.1017/S0016756801005738>.
- Muller, R.A., MacDonald, G.J., 2000. Ice Ages and Astronomical Causes: Data, Spectral Analysis, and Mechanisms. Springer-Praxis, London, 318 p.
- Nestor, H., Einasto, R., Nestor, V., Marss, T., Viira, V., 2001. Description of the type section, cyclicity and correlation of the Riksu Formation (Wenlock, Estonia). Proc. Est. Acad. Sci. Geol. 50, 149–173.
- Nie, J., 2017. The Plio-Pleistocene 405-kyr climate cycles. Palaeogeogr. Palaeoclimatol. Palaeoecol. <https://doi.org/10.1016/j.palaeo.2017.07.022>.
- Olea, R.A., 2004. CORRELATOR 5.2 – a program for interactive lithostratigraphic correlation of wireline logs. Comput. Geosci. 30, 561–567. <https://doi.org/10.1016/j.cageo.2004.01.006>.
- Olea, R.A., 1994. Expert systems for automated correlation and interpretation of wireline logs. Math. Geol. 26, 879–897. <https://doi.org/10.1007/BF02083420> 2.
- Olsen, P.E., 2010. Fossil Great Lakes of the Newark Supergroup – 30 Years Later. In: Benimoff, A.I. (Ed.), *Field Trip Guidebook*, New York State Geological Association, 83rd Annual Meeting, College of Staten Island, pp. 101–162.
- Olsen, P.E., 1997. Stratigraphic record of the early Mesozoic breakup of Pangea in the Laurasia-Gondwana rift system. Annu. Rev. Earth Planet Sci. 25, 337–401. <https://doi.org/10.1146/annurev.earth.25.1.337>.
- Olsen, P.E., Kent, D.V., 1999. Long period Milankovitch cycles from the Late Triassic and Early Jurassic of eastern North America and their implications for the calibration of the early Mesozoic timescale and the long-term behavior of the planets. Phil. Trans. R. Soc. Lond. Ser. A 357, 1761–1786. <https://doi.org/10.1098/rsta.1999.0400>.
- Olsen, P.E., Kent, D.V., 1996. Milankovitch climate forcing in the tropics of Pangaea during the Late Triassic. Palaeogeogr. Palaeoclimatol. Palaeoecol. 122, 1–26. [https://doi.org/10.1016/0031-0182\(95\)00171-9](https://doi.org/10.1016/0031-0182(95)00171-9).

- Olseger, D.A., Read, J.F., 1991. Relation of eustasy to stacking patterns of meter-scale carbonate cycles, Late Cambrian, USA. *J. Sediment. Petrol.* 61 (7), 1225–1252. <https://doi.org/10.1306/D426786B-2B26-11D7-8648000102C1865D>.
- Pálike, H., Shackleton, N.J., 2000. Constraints on astronomical parameters from the geological record for the last 25 Myr. *Earth Planet. Sci. Lett.* 182, 1–14. [https://doi.org/10.1016/S0012-821X\(00\)00229-6](https://doi.org/10.1016/S0012-821X(00)00229-6).
- Pálike, H., Norris, R.D., Herrelle, J.O., Wilson, P.A., Coxall, H.K., Lear, C.H., Shackleton, N.J., Tripati, A.K., Wade, B., 2006. The heartbeat of the Oligocene climate system. *Science* 314, 1894–1898. <https://doi.org/10.1126/science.1133822>.
- Pálike, H., Laskar, J., Shackleton, N.J., 2004. Geological constraints on the chaotic diffusion of the solar system. *Geology* 32, 929–932. <https://doi.org/10.1130/G20750.1>.
- Paillard, D., Labeyrie, L., Yiou, P., 1996. MacIntosh program performs time series analysis: *Eos Transactions. Am. Geophys. Union* 77, 379. <https://doi.org/10.1029/96EO00259>.
- Pannella, G., 1972. Paleontological evidence on the Earth's rotational history since early Precambrian. *Astrophys. Space Sci.* 16, 212–237. <https://doi.org/10.1007/BF00642735>.
- Park, J., Herbert, T.D., 1987. Hunting for paleoclimatic periodicities in a geological time series with an uncertain time scale. *J. Geophys. Res.* 92, 14027–14040. <https://doi.org/10.1029/JB092iB13p14027>.
- Pas, D., Hinnov, L.A., Day, J., Kodama, K., Sinnesael, M., Liu, W., 2018. Cyclostratigraphic calibration of the Famennian Stage (Late Devonian, Illinois Basin, USA). *Earth Planet. Sci. Lett.* 488, 102–114. <https://doi.org/10.1016/j.epsl.2018.02.010>.
- Pilgrim, L., 1904. Versuch einer rechnerischen Behandlung des Eiszeitproblems. *Jahresshefte des Vereins für Vaterländische Naturkunde Württemberg*, Stuttgart 60, 26–117.
- Poliakov, E., 2005. Numerical modelling of the paleotidal evolution of the Earth-Moon System. In: Knezević, Z., Milani, A. (Eds.), *Dynamics of Populations of Planetary Systems*, Proceedings IAU Colloquium No. 197, pp. 445–452. <https://doi.org/10.1017/S174392130400897X>.
- Preto, N., Hinnov, L.A., Hardie, L.A., De Zanche, V., 2001. A Middle Triassic orbital signal recorded in the shallow marine Latemar carbonate buildup (Dolomites, Italy). *Geology* 29, 1123–1128. [https://doi.org/10.1130/0091-7613\(2001\)029<1123:MTOS-RI>2.0.CO;2](https://doi.org/10.1130/0091-7613(2001)029<1123:MTOS-RI>2.0.CO;2).
- Radzevičius, S., Tumakovaitė, B., Spiridonov, A., 2017. Upper Homerian (Silurian) high-resolution correlation using cyclostratigraphy: an example from western Lithuania. *Acta Geol. Pol.* 67 (2), 307–322. <https://doi.org/10.1515/agp-2017-0011>. Warszawa.
- Rameil, N., 2005. *Carbonate Sedimentology, Sequence Stratigraphy, and Cyclostratigraphy of the Tithonian in the Swiss and French Jura Mountains*. PhD Thesis. University of Fribourg, Switzerland, 244 p.
- Ramezani, J., Bowring, S.A., 2018. Advances in Numerical Calibration of the Permian Timescale Based on Radioisotopic Geochronology, vol. 450. Geological Society, London, pp. 51–60. <https://doi.org/10.1144/SP450.17>. Special Publications.
- Rasmussen, J., Hinnov, L.A., Thibault, N., 2018. *Astronomical Time Calibration of the Great Ordovician Biodiversification Event (in preparation)*.
- Renne, P.R., Deino, A.L., Hilgen, F.J., Kuiper, K.F., Mark, D.F., Michell III, W.S., Morgan, L.E., Mundil, R., Smit, J., 2013. Time Scales of Critical Events Around the Cretaceous-Paleogene Boundary. *Science* 339, 684–687. <https://doi.org/10.1126/science.1230492>.
- Ripepe, M., Fischer, A.G., 1991. Stratigraphic rhythms synthesized from orbital variations. In: Franseen, E.K., Watney, W.L., Kendall, C.G.S., Ross, W. (Eds.), *Sedimentary Modeling: Computer Simulations and Methods for Improved Parameter Definition*, Kansas Geological Survey Bulletin, 233, pp. 335–344. <http://www.kgs.ku.edu/Publications/Bulletins/233/index.html>.

- Rodrigues, P.O.C., Hinnov, L.A., Franco, D., 2018. A new appraisal of depositional cyclicity in the Neoarchean–Paleoproterozoic Dales Gorge Member (Brockman Iron Formation, Hamersley Basin, Australia). *Precambrian Res.* (in review).
- Rodionov, V.P., Dekkers, M.J., Khramov, A.N., Gurevich, E.L., Krijgsman, W., Duermeijer, C.E., Heslop, D., 2003. Paleomagnetism and cyclostratigraphy of the Middle Ordovician Kriolutsky Suite, Krivaya Luka section, southern Siberian Platform: Record of nonsynchronous NRM-components or a non-axial geomagnetic field? *Stud. Geophys. Geodessy.* 47, 255–274.
- Röhl, U., Westerhold, T., Bralower, T.J., Zachos, J.C., 2007. On the duration of the Paleocene–Eocene thermal maximum (PETM). *G-cubed* 8. <https://doi.org/10.1029/2007GC001784>.
- Ruhl, M., Hesselbo, S.P., Hinnov, L.A., Jenkyns, H.C., Xu, W., Storm, M., Riding, J., Minisini, D., Ullmann, C.U., Leng, M.J., 2016. Astronomical constraints on the duration of the Early Jurassic Pliensbachian stage and global climate fluctuations. *Earth Planet. Sci. Lett.* 455, 149–165. <https://doi.org/10.1016/j.epsl.2016.08.038>.
- Sageman, B.B., Singer, B.S., Meyers, S.R., Siewert, S.E., Walaszczyk, I., Condond, D.J., Jicha, B.R., Obradovich, J.D., Sawyer, D.A., 2014. Integrating  $^{40}\text{Ar}/^{39}\text{Ar}$ , U-Pb, and astronomical clocks in the Cretaceous Niobrara Formation, Western Interior Basin, USA. *GSA Bull.* 126 (7–8), 956–973. <https://doi.org/10.1130/B30929.1>.
- Schiffelbein, P., Dorman, L., 1986. Spectral effects of time-depth nonlinearities in deep sea sediment cores: a demodulation technique for realigning time and depth scales. *J. Geophys. Res.* 91, 3821–3835.
- Schwarzacher, W., 1993. Cyclostratigraphy and the Milankovitch Theory. In: *Developments in Sedimentology*, vol. 52. Elsevier, Amsterdam, 224 p.
- Scrutton, C.T., 1978. Periodic growth features in fossil organisms and the length of the day and month. In: Brosche, P., Sündermann, J. (Eds.), *Tidal Friction and the Earth's Rotation*. Springer-Verlag, Berlin, pp. 154–196. [https://doi.org/10.1007/978-3-642-67097-8\\_12](https://doi.org/10.1007/978-3-642-67097-8_12).
- Schmitz, M.D., Davydov, V.I., 2012. Quantitative radiometric and biostratigraphic calibration of the Pennsylvanian-Early Permian (Cisuralian) time scale and pan-Euramerican chronostratigraphic correlation. *Geol. Soc. Am. Bull.* 124, 549–577. <https://doi.org/10.1130/B30385.1>.
- Shackleton, N.J., Crowhurst, S.J., Weedon, G.P., Laskar, J., 1999. Astronomical calibration of Oligocene–Miocene time. *Phil. Trans. R. Soc. Lond. Ser. A* 357, 1907–1929. <https://doi.org/10.1098/rsta.1999.0407>.
- Sharaf, S.G., Budnikova, N.A., 1969. Secular changes in the Earth's orbital elements and the astronomical theory of climate variations. *Trudy Instituta Teoreticheskoy Astronomii, Leningrad* 14, 48–84.
- Sharaf, S.G., Budnikova, N.A., 1967. Secular variations of elements of the Earth's orbit which influence the climate of the geological past. *Trudy Instituta Teoreticheskoy Astronomii, Leningrad* 11, 231–261.
- Sinnesael, M., Mauviel, A., Desrochers, A., McLaughlin, P.I., De Weirdt, J., Vandenbroucke, T.R.A., Claeys, P., 2017b. Cyclostratigraphy of the Upper Ordovician Vaureal Formation, Anticosti Island, eastern Canada. *Geol. Soc. Am. Annual Meet. Seattle, WA, Abstracts with Programs* 49 (6). <https://doi.org/10.1130/abs/2017AM-302947>.
- Sinnesael, M., Loi, A., Dabard, M.-P., Vandenbroucke, T., Claeys, P., 2017a. Cyclostratigraphic analysis of the Middle to lower Upper Ordovician Postolonnec Formation in the Armorican Massif (France): integrating XRF, gamma-ray and lithological data. *Geophys. Res. Abstr.* 19. EGU2017-9565, General Assembly, Vienna, Austria.

- Sprovieri, M., Sabatino, N., Pelosi, N., Batenburg, S.J., Coccioni, C., Iavarone, M., Mazzola, S., 2013. Late Cretaceous orbitally-paced carbon isotope stratigraphy from the Bottaccione Gorge (Italy). *Palaeogeogr. Palaeoclimatol. Palaeoecol.* 379–380, 81–94. <https://doi.org/10.1016/j.palaeo.2013.04.006>.
- Stockwell, J.N., 1873. Memoir on the secular variations of the elements of the eight principal planets. *Smithsonian Contributions to Knowledge, Washington* 18 (3), 199 p.
- Sucheras-Marx, B., Giraud, F., Fernandez, V., Pittet, B., Lecuyer, C., Olivero, D., Mattioli, E., 2013. Duration of the Early Bajocian and the associated  $\delta^{13}\text{C}$  positive excursion based on cyclostratigraphy. *J. Geol. Soc. Lond.* 170, 107–118. <https://doi.org/10.1144/jgs2011-133>.
- Svensen, H.H., Hammer, Ø., Corfu, F., 2015. Astronomically forced cyclicity in the Upper Ordovician and U–Pb ages of interlayered tephra, Oslo Region, Norway. *Palaeogeogr. Palaeoclimatol. Palaeoecol.* 418, 150–159. <https://doi.org/10.1016/j.palaeo.2014.11.001>.
- Thibault, N., Jarvis, I., Voight, S., Gale, A.S., Attree, K., Jenkyns, H.C., 2016. Astronomical calibration and global correlation of the Santonian (Cretaceous) based on the marine carbon isotope record. *Paleoceanography* 31, 847–865. <https://doi.org/10.1002/2016PA002941>.
- Thomson, D.J., 1990. Quadratic-Inverse Spectrum Estimates: Applications to Palaeoclimatology. *Phil. Trans. Phys. Sci. Eng.* 332 (1627), 539–597. <https://doi.org/10.1098/rsta.1990.0130>.
- Thomson, D.J., 2009. Time-series analysis of paleoclimate data. In: Gornitz, V. (Ed.), Encyclopedia of Paleoclimatology and Ancient Environments, pp. 949–959. [https://doi.org/10.1007/978-1-4020-4411-3\\_222](https://doi.org/10.1007/978-1-4020-4411-3_222).
- Thomson, D.J., 1982. Spectrum estimation and harmonic analysis. *Proc. IEEE* 70, 1055–1096. <https://doi.org/10.1109/PROC.1982.12433>.
- Trendall, A.F., 1973. Varve cycles in the Weeli Wollie Formation of the Precambrian Hamersley Group, Western Australia. *Econ. Geol.* 68, 1089–1097. <https://doi.org/10.2113/gsecongeo.68.7.1089>.
- Trendall, A.F., 1966. Second progress report on the Brockman Iron Formation in the Wittenoom-Yampire area. In: *Annual Report for the Year 1965, Geological Survey of Western Australia*, pp. 75–87.
- Trendall, A.F., 1965. Progress report on the Brockman Iron Formation in the Wittenoom-Yampire area. In: *Annual Report for the Year 1964, Geological Survey of Western Australia*, pp. 55–64.
- Vanyo, J.P., Awramik, S.M., 1985. Stromatolites and Earth-Sun-Moon dynamics. *Precambrian Res.* 29, 121–142. [https://doi.org/10.1016/0301-9268\(85\)90064-6](https://doi.org/10.1016/0301-9268(85)90064-6).
- Vernekar, A.D., 1972. Long-period global variations of incoming solar radiation. *Meteorol. Monogr.* 12 (34), 130 p.
- Wahr, J.M., 1988. The Earth's rotation. *Annu. Rev. Earth Planet Sci.* 16, 231–249. <https://doi.org/10.1146/annurev.ea.16.050188.001311>.
- Wang, C., Feng, Z., Zhang, L., Huang, Y., Cao, K., Wang, P., Zhao, B., 2013. Cretaceous paleogeography and paleoclimate and the setting of SKI borehole sites in Songliao Basin, northeast China. *Palaeogeogr. Palaeoclimatol. Palaeoecol.* 385, 17–30. <https://doi.org/10.1016/j.palaeo.2012.01.030>.
- Walker, J.C.G., Zahnle, K.J., 1986. Lunar nodal tide and distance to the Moon during the Precambrian. *Nature* 320, 600–602. <https://doi.org/10.1038/320600a0>.
- Waltham, D., 2015. Milankovitch period uncertainties and their impact on cyclostratigraphy. *J. Sediment. Res.* 85, 990–998. <https://doi.org/10.2110/jsr.2015.66>.
- Weedon, G.P., Coe, A.L., Gallois, R.W., 2004. Cyclostratigraphy, orbital tuning and inferred productivity for the type Kimmeridge Clay (Late Jurassic), Southern England. *J. Geol. Soc.* 161, 655–666. <https://doi.org/10.1144/0016-764903-073>.

- Wells, J.W., 1970. Problems of annual and daily growth-rings in corals. In: Runcorn, S.K. (Ed.), *Palaeogeophysics*. Academic, San Diego, CA, pp. 3–9.
- Westerhold, T., Röhl, U., Frederichs, T., Bohaty, S.M., Zachos, J.C., 2015. Astronomical calibration of the geological timescale: closing the middle Eocene gap. *Clim. Past* 11, 1181–1195. <https://doi.org/10.5194/cp-11-1181-2015>.
- Westerhold, T., Röhl, U., Pälike, H., Wilkens, R., Wilson, P.A., Acton, G., 2014. Orbitally tuned timescale and astronomical forcing in the middle Eocene to early Oligocene. *Clim. Past* 10, 955–973. <https://doi.org/10.5194/cp-10-955-2014>.
- Westerhold, T., Röhl, U., Laskar, J., 2012. Time scale controversy: accurate orbital calibration of the early Paleogene. *G-cubed* 13, Q06015. <https://doi.org/10.1029/2012gc004096>.
- Westerhold, T., Röhl, U., Raffi, I., Fornaciari, E., Monechi, S., Reale, V., Bowles, J., Evans, H.F., 2008. Astronomical calibration of the Paleocene time. *Palaeogeogr. Palaeoclimatol. Palaeoecol.* 257, 377–403. <https://doi.org/10.1016/j.palaeo.2007.09.016>.
- Westerhold, T., Röhl, U., Laskar, J., Bowles, J., Raffi, I., Lourens, L.J., Zachos, J.C., 2007. On the duration of magnetochrons C24r and C25n and the timing of early Eocene global warming events: implications from the Ocean Drilling Program Leg 208 Walvis Ridge depth transect. *Paleoceanography* 22, PA2201. <https://doi.org/10.1029/2006PA001322>.
- Williams, G.E., 2000. Geological constraints on the Precambrian history of Earth's rotation. *Rev. Geophys.* 38 (1), 37–59. <https://doi.org/10.1029/1999RG900016>.
- Williams, G.E., 1991. Milankovitch-band cyclicity in bedded halite deposits contemporaneous with Late Ordovician–Early Silurian glaciation, Canning Basin, western Australia. *Earth Planet. Sci. Lett.* 103, 143–155. [https://doi.org/10.1016/0012-821X\(91\)90156-C](https://doi.org/10.1016/0012-821X(91)90156-C).
- Williams, G.E., 1989. Tidal rhythmites: Geochronometers for the ancient Earth-Moon system.  *Episodes* 12, 162–171.
- Williams, J.G., 1994. Contributions to the Earth's obliquity rate, precession and nutation. *Astronomical J.* 108 (2), 711–724. <https://doi.org/10.1086/117108>.
- Wu, H., Hinnov, L.A., Chu, R., Zhang, S., Jiang, G., Yang, R., Li, H., Xi, D., Wang, C., 2018b. Terrestrial evidence for two Solar System chaotic events in the Late Cretaceous geological record. *Earth Planet. Sci. Lett.* (in review).
- Wu, H., Fang, Q., Wang, X., Hinnov, L.A., Qi, Y., Shen, S., Yang, T., Li, H., Chen, J., Zhang, S., 2018a. A  $\sim$ 34 m.y. astronomical time scale for the uppermost Mississippian through Pennsylvanian of the Carboniferous System. *Geology* (in review).
- Wu, H., Zhang, S., Hinnov, L.A., Jiang, G., Yang, T., Li, H., Wan, X., Wang, C., 2014. Cyclostratigraphy and orbital tuning of the terrestrial upper Santonian–Lower Danian in Songliao Basin, northeastern China. *Earth Planet. Sci. Lett.* 407, 82–95. <https://doi.org/10.1016/j.epsl.2014.09.038>.
- Wu, H., Zhang, S., Hinnov, L.A., Feng, Q., Jiang, G., Li, H., Yang, T., 2013. Late Permian Milankovitch cycles. *Nat. Commun.* <https://doi.org/10.1038/ncomms3452>.
- Yao, X., Zhou, Y., Hinnov, L.A., 2015. Astronomical forcing of Middle Permian chert in the Lower Yangtze area, South China. *Earth Planet. Sci. Lett.* 422, 206–221. <https://doi.org/10.1016/j.epsl.2015.04.017>.
- Yu, Z.W., Ding, Z.L., 1998. An automatic orbital tuning method for paleoclimate records. *Geophys. Res. Lett.* 25, 4525–4528. <https://doi.org/10.1029/1998GL900197>.
- Zachos, J.C., Pagani, M., Sloan, L., Thomas, E., Billups, K., 2001. Trends, rhythms, and aberrations in global climate 65 Ma to present. *Science* 292, 686–693. <https://doi.org/10.1126/science.1059412>.
- Zachos, J.C., Dickens, G.R., Zeebe, R.E., 2008. An early Cenozoic perspective on greenhouse warming and carbon-cycle dynamics. *Nature* 451, 279–283. <https://doi.org/10.1038/nature06588>.

- Zeebe, R.E., 2017. Numerical solutions for the orbital motion of the Solar System over the past 100 Myr: limits and new results. *Astronomical J.* 154, 193. <https://doi.org/10.3847/1538-3881/aa8cce>.
- Zeeden, C., Kaboth, S., Hilgen, F.J., Laskar, J., 2018. Taner filter settings and automatic correlation optimisation for cyclostratigraphic studies. *Comput. Geosci.* 119, 18–28. <https://doi.org/10.1016/j.cageo.2018.06.005>.
- Zeeden, C., Meyers, S.R., Louren, L.J., Hilgen, F.J., 2015. Testing astronomically tuned age models. *Paleoceanography* 30. <https://doi.org/10.1002/2014PA002762>.
- Zeeden, C., Hilgen, F., Hüsing, S., Lourens, L., 2014. The Miocene astronomical time scale 9–12 Ma: new constraints on tidal dissipation and their implications for paleoclimatic investigations. *Paleoceanography* 29 (4), 296–307. <https://doi.org/10.1002/2014PA002615>.
- Zhang, S., Wang, X., Hammarlund, E.U., Wang, H., Mafalda Costa, M., Bjerrum, C.J., Connelly, J.N., Zhang, B., Bian, L., Canfield, D.E., 2015. Orbital forcing of climate 1.4 billion years ago. *Proc. Natl. Acad. Sci.* 112 (12), E1406–E1413. <https://doi.org/10.1073/pnas.1502239112>.